CHAPTER 2

Theoretical Investigation of Optical Properties of Single-Walled Carbon Nanotubes

Yang Zhao, XiuJun Wang, Chi-Chiu Ma, GuanHua Chen
Department of Chemistry, The University of Hong Kong, Hong Kong, People's Republic of China

CONTENTS

1. INTRODUCTION

Ever since their inception [1], carbon nanotubes (CNTs) have attracted a tremendous amount of intense experimental and theoretical interest. Synthesis of large quantities of CNTs [2] has been achieved through carbon-arc vaporization in a gas atmosphere or

ISBN: 1-58883-049-7

Handbook of Theoretical and Computational Nanotechnology
Edited by Michael Rieth and Wolfram Schommers
Volume 7: Pages (79–126)

transition-metal catalytic reaction; the latter method has been used to synthesize single-walled nanotubes (SWNTs) [3, 4]. Both open-ended and capped CNTs have been observed by high-resolution transmission electron microscope (TEM) [1, 5] and scanning tunneling microscopy [6] techniques. Because of their superb electronic and mechanical properties, many potential applications have been proposed for CNTs, such as single-electron transistors [7], tunneling-magnetoresistance devices [8], CNT diodes [9], intramolecular junctions [10], molecular bearings [11, 12], springs [13], hooks [14], and gigahertz oscillators [15–19]. Several theoretical studies revealed that CNTs would be either metallic or semiconducting, depending on their underlying structures [20–23].

The simplest among all CNTs, an SWNT, is an individual graphene sheet wrapped in the shape of a seamless cylinder, which can be characterized by its chiral vector (m, n) [22, 24]. As a simple, elongated constituent of the fullerene family, SWNTs are especially attractive to many applications thanks to their remarkable physical, chemical, and mechanical properties. In particular, their dimensions and electronic behaviors make them the ideal building blocks for molecular electronics, and recently, a self-assembled carbon nanotube field-effect transistor (FET) has been built at room temperature, using a scheme based on recognition between molecular building blocks [25]. Photoconductivity on infrared laser illumination has also been measured for individual CNTs that act as channels for an ambipolar FET [26].

It is difficult to exaggerate the importance of optical properties of SWNTs, which are vital to the development of SWNT photonic applications such as nanoscale integrated electroluminescent devices [27], to a variety of interdisciplinary applications. Optical absorption and fluorescence spectroscopy measurements provide evidence for individually dispersed carbon nanotubes, and therefore, optical properties of SWNTs have become an important tool for structure-based nanotube characterization in the exciting, emerging field of DNA-assisted manipulation of the carbon nanotubes [28]. Identification of spectroscopic features and correlations with nanotube structures also aids attempts to purify, separate, and sort SWNTs, and understanding their electronic structure helps their development as optical devices, sensors, and molecular electronics components.

Carbon nanotubes are quasi-one-dimensional crystals whose optical properties are dependent on chiralities and diameters, as well as orientations. Early measurements were often performed on multiwalled nanotubes or bundles of them and SWNTs [29, 30]. For instance, the bulk electronic properties of SWNT bundles have been studied by the high-resolution electron energy loss spectroscopy (EELS) in transmission [29]. Low-energy nondispersive features were attributed to the energy separations of DOS singularities in the nanotubes. The peak appearing in the optical conductivity at 1.8 eV was argued to originate from metallic nanotubes in the bundles. Optical absorption spectroscopy on SWNT-containing soot shows peaks between 0.6 and 3 eV that are interpreted as interband transitions between the van Hove singularities [31]. The absorption spectra of bundles of SWNTs of similar sizes have been measured, for example, on 4 Å SWNTs made by pyrolysis of tripropylamine molecules in the channels of porous zeolite $AlPO_4$-5 (AFI) single crystals [32, 33]. It is possible for only three chiralities to achieve diameters near 4 Å. When the light electric field is polarized parallel to the AFI crystal channel orientation, three low-frequency bands have been observed in the measured absorption spectra of bundles of carbon nanotubes, among which the two lowest bands were assigned to the semiconducting tubes and the third to the conducting nanotubes. When the electric field is perpendicular to the AFI crystal channel orientation, the nanotube is nearly transparent in the measured energy region 0.5–4.1 eV.

Suspension of individual SWNTs and removal of remaining bundles from solution have recently been achieved by encasing individual nanotubes in cylindrical micelles [34]. Spectrofluorimetric measurements on semiconducting SWNTs isolated in aqueous surfactant suspensions [35] delivered, for the first time, spectral information on nanotube chiralities in addition to that on diameters. Exploiting the band-gap fluorescence of these SWNTs as well as advances in solution-phase dispersion and processing of nanotubes led to a definitive (n, m) assignment to semiconducting features. Because metallic nanotubes do not fluoresce, assignment of the metallic species in a similar manner required the help of Raman spectroscopy, which was performed for laser excitations between 565 and 627 nm and also between 458 and 514.5 nm [36]. An (n, m) index has been provided to features in both optical

absorption and Raman spectra for these metallic SWNTs. In the absence of a perturbative environment of tubes and surfaces, SWNTs in aqueous micellar suspensions show much better resolved optical absorption spectra, and the one-dimensional semiconducting band gap was also found to fluoresce strongly in the 800–1600 nm range that is important to fiberoptic communications and bioimaging. Aggregation of nanotubes into bundles quenches fluorescence through interactions with metallic tubes and broadens the absorption spectra. In addition, polydispersity and poor solubility of SWNT bundles in both aqueous and nonaqueous solutions impose considerable challenges to various application-mandated separation and assembly attempts to use SWNTs as an individual macromolcular species. DNA-assisted dispersion and separation of carbon nanotubes have recently been reported [37] as an alternative to aqueous micellar suspension of SWNTs. Bundled SWNTs are effectively dispersed in water by their sonication in the presence of single-stranded DNA (ssDNA). Molecular modeling suggests that ssDNA can bind to carbon nanotubes through π-stacking, resulting in helical wrapping to the surface with a binding free energy of ssDNA to carbon nanotubes that rivals that between two nanotubes. Furthermore, wrapping of CNTs by ssDNA was found to be sequence dependent [28]. That DNA-coated SWNTs can be separated into fractions with different electronic structures by ion-exchange chromatography links one of the central molecules in biology to a technologically very important nanomaterial and opens the door to CNT-based applications in biotechnology. In this process, optical spectroscopy of SWNTs is indispensable to the characterization of nanotube geometrical, electronic, and various other properties.

Previously, it was known that ionic doping creates new metallic bands in semiconducting SWNTs. Only recently, it was shown that covalent chemistry can covert the metallic SWNTs to semiconductors, which may lead to efficient nanotube separation [38, 39]. Diazonium agents were shown to functionalize SWNTs suspended in aqueous solution with high selectivity and to display an autocatalytic effect that functionalizes the entire tube. In particular, metallic species are selected to react to the near exclusion of semiconducting SWNTs under controlled conditions [39]. Discovery of the selective functionalization of metallic nanotubes was made via the ultraviolet-visible-near-infrared absorption spectra and Raman spectroscopy. Absorption features allow for the monitoring of valence electrons in each distinct nantotube in transitions to conduction bands. A first theoretical study on the effect of functionalization on the SWNT optical spectra will be presented here. In addition, absorption spectra for double-walled carbon nanotubes (DWNTs) and CNT junctions are also discussed.

Part of the attractiveness of the CNTs has been their rich electronic properties, which may be altered via physical or chemical modifications to the CNTs. Significant progress has been made in filling the nanotubes with a range of materials. A large enhancement in conductivity is reported after doping with potassium and bromine separately [40]. Recently, potassium iodide has been successfully inserted into single-walled carbon nanotubes [41, 42]. We present here a first-principles DFT calculation of the electronic and optical properties of a potassium iodide intercalated (10, 10) nanotube.

This review is organized as follows. In Section 2, we introduce band structures of the SWNTs via the zone-folding approach from those of a graphene sheet. We discuss in detail the transition dipole moment of the SWNTs in the entire Brillouin zone when the external light field is aligned with the nanotube axis, which is followed by discussions on the absorption spectra as dictated intuitively by the transition dipole field lines and band structure contours in the framework of the simplified tight-binding model. In Section 3, optical properties of a series of finite size SWNTs including those with the smallest diameter (4 Å) are studied systematically. Their absorption spectra are calculated with the semiempirical localized-density-matrix (LDM) method based the time-dependent Hartree-Fock (TDHF) approximation. The finite optical gaps are predicted for the infinite long SWNTs. Strong anisotropy of the dynamic polarizabilities is found for 4-Å SWNTs. The compositions of the dipole-induced excitations are examined by projecting the corresponding density matrices onto the Hartree–Fock molecular orbital representation. Natures of optical excitations are investigated by examining the corresponding reduced single-electron density matrices. In Section 4, the application of the first-principles density-function theory (DFT) calculations to

SWNTs is discussed, and the focus is on the electronic and optical properties of a potassium iodide intercalated (10, 10) SWNT. In Section 5, low-energy absorption features calculated from the tight-binding model and the LDM method are compared with those from the DFT approach. Good agreements are obtained. A brief summary is given in Section 6.

2. TIGHT-BINDING MODEL

2.1. SWNTs As Quantum Confinements of Graphite

Conceptually, SWNTs are simply rolled-up graphene sheets. The diversity in the electronic structure of SWNTs arises from the quantization of the electronic wave vector of the one-dimensional systems classified by their chiralities. As shown in Fig. 1, the chiral vector $\mathbf{C}_h$ in units of hexagonal elements connecting two points on the plane defines a SWNT chirality, (n, m) [22, 24]

$$\mathbf{C}_h = n\mathbf{a}_1 + m\mathbf{a}_2 \tag{1}$$

with $\mathbf{a}_1$ and $\mathbf{a}_2$ being the real space unit vectors of the hexagonal graphite lattice. The integers n and m are such that $0 \leq |m| \leq n$. An armchair nanotube (3, 3) and a zigzag nanotube (6, 0) are shown in Fig. 1 as two examples. Because SWNTs are folded from graphene sheets, it is not surprising that their physical properties are closely related to those of the graphite, as shall be demonstrated in this review of their optical properties [22]. The chiral vector $\mathbf{C}_h$ is along the circumferential direction of the nanotube and, therefore, is orthogonal to the nanotube axis. The reciprocal lattice vectors $\mathbf{k}_2$ and $\mathbf{k}_2$ are defined as follows

$$\mathbf{k}_1 = N^{-1}(-t_2\mathbf{b}_1 + t_1\mathbf{b}_2), \qquad \mathbf{k}_2 = N^{-1}(m\mathbf{b}_1 - n\mathbf{b}_2) \tag{2}$$

where $\mathbf{b}_1$ and $\mathbf{b}_2$ are the unit vectors of the reciprocal lattice, $t_1 = d_R^{-1}(2m + n)$ and $t_2 = d_R^{-1}(2n + m)$, with d_R the greatest common divisor of $2n + m$ and $2m + n$. Spatially, $\mathbf{k}_2$ is along the tubule axis, and $\mathbf{k}_1$ is in the circumferential direction. The translational vector $\mathbf{T}$ is a unit vector for the one-dimensional carbon nanotube. It is parallel to the nanotube axis and can be expressed as

$$\mathbf{T} = t_1\mathbf{a}_1 + t_2\mathbf{a}_2 \tag{3}$$

In the tight-binding model in which only π electrons are considered, the electronic structure of a carbon nanotube can be derived directly from that of a graphene sheet via the so-called zone folding of the two-dimensional energy dispersion relation of the graphite. Intuitively, the band spectra of a carbon nanotube are the intersects of the graphene sheet's conduction and valence energy surfaces and a set of parallel planes perpendicular to the Brillouin zone. The hexagon in Fig. 2a is the first Brillouin zone of the graphene sheet, and the parallel dashed lines, which are along the tubule axis $\mathbf{T}$, are the intersects between the

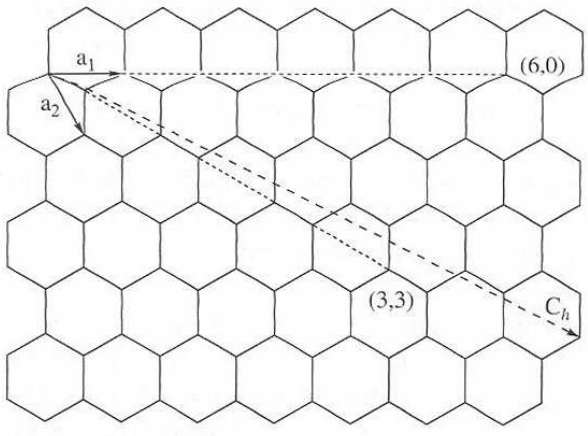

Figure 1. Schematic plot of a two-dimensional graphene sheet showing the lattice vectors $\mathbf{a}_1$ and $\mathbf{a}_2$, and the chiral vector $\mathbf{C}_h = n\mathbf{a}_1 + m\mathbf{a}_2$. An armchair nanotube (3, 3) and a zigzag nanotube (6, 0) are indicated as two examples.

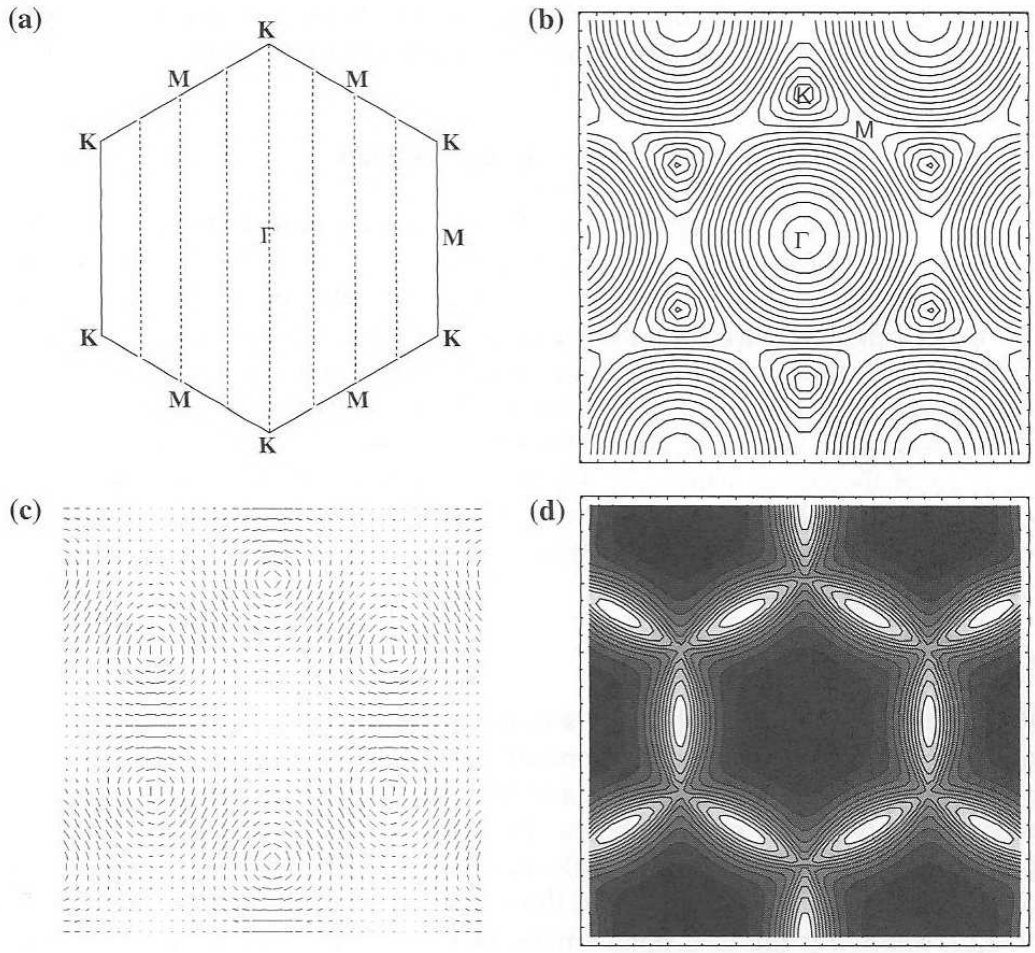

Figure 2. (a) The first Brillouin zone of graphene. The parallel lines (along the tubule axis **T**) are the intersects between the Brillouin zone and the parallel planes that are perpendicular to the Brillouin zone. They represent the allowed states for a (5, 5) SWNT. (b) The contour plot of the conduction band of the graphene sheet. The circle at the center of the first Brillouin zone is the Γ point, and the six surrounding circles are the K points at which the conduction and valence bands join. (c) The transition-dipole field lines of graphene in the first Brillouin zone. The orientations of the lines represent the directions of the transition dipoles at that particular **k**, and the lengths of the lines represent the sizes of the transition dipoles. The transition dipole vanishes asymptotically on approaching the Brillouin zone center. The size of transition dipole reaches its maxima on lines connecting neighboring K points. A circular pattern is found around K points. (d) The contour plot of the oscillator strength $|\mathbf{d}|^2$. The $|\mathbf{d}|^2$ maxima are located at M points (light area), and its minima at the Γ point (dark area). Reprinted with permission from [43], Y. Zhao et al., *Chem. Phys. Lett.* 387, 149 (2004). © 2004, Elsevier B. V.

Brillouin zone and the set of parallel planes. The parallel lines shown in Fig. 2a are the allowed states for a (5, 5) SWNT. At K points, the conduction (E_c) and valence (E_v) bands join, and the energy difference $E_c - E_v$ vanishes; at Γ point $E_c - E_v$ reaches its maxima, and M points are the saddle points at which the energy difference is rather flat nearby. If one of the intersects or parallel lines such as those in Fig. 2a goes through a K point in the Brillouin zone, the tube is metallic ($n - m = 3k$). Otherwise, it is a semiconductor ($n - m = 3k \pm 1$). The absorption spectra of SWNTs can be similarly obtained from the optical properties of a graphene sheet via a set of graphic tools, which will be demonstrated in this review.

Neglecting the overlap integral between the adjacent carbon atoms, the conduction band for a graphene sheet is commonly approximated by

$$E_c(\mathbf{k}) = V_{pp\pi}\sqrt{3 + 4\cos\frac{\sqrt{3}k_x}{2}\cos\frac{k_y}{2} + 2\cos k_y} \tag{4}$$

where $V_{pp\pi}$ is the transfer integral between adjacent lattice points, also called the nearest-neighbor $pp\pi$ interaction. A plot of $E_c(\mathbf{k})$ is given in Fig. 2a. The Hamiltonian field of $E_c(\mathbf{k})$ is shown in Fig. 2b. The conduction band describes the π^*-energy antibonding band and the covalence band, which is the mirror image of the conduction with respect to the

Fermi energy, the π-energy bonding band. The two bands are degenerate at K points the Fermi energy crosses. The conduction bands of the SWNTs folded from the planar graphite sheet can be obtained from

$$E^{\text{tube}}_{\text{c},k_2} = E_{\text{c}}(k\mathbf{k}_2|\mathbf{k}_2|^{-1} + \mu\mathbf{k}_1) \tag{5}$$

where $\mu = 1, \ldots, N$, and $-\pi/|\mathbf{T}| < k < \pi/|\mathbf{T}|$. The vertical parallel lines in Fig. 2a, or the intersects, are along the $\mathbf{k}_2$ directions. Therefore, the intersects are also called $\mathbf{k}_2$ cuts.

Kataura et al. plotted energy differences between the ith van Hove singularities in the conduction and valence bands (both numbered from the Fermi energy) $E_{ii}(d_t)$ as a function of the nanotube diameter d_t for all chiralities, and showed that the energy differences $E_{ii}(d_t)$ have a finite width for a given d_t [31]. This width in $E_{ii}(d_t)$ increases with the increasing energy deviation of $E_{ii}(d_t)$ from the Fermi energy. It was later attributed to the trigonal warping effect of the energy bands [44, 45], which is referred to the deviation of the equal-energy contours near the K points in the Brillouin zone away from K-centered circular patterns and toward a triangular shape, with the three neighboring M points as its corners (cf. Fig. 2b).

2.2. Transition Dipole Moment

In 1998 White and Mintmire [46] solved a puzzle posed by Dresselhaus [21] on the density of states (DOS) being independent of translational unit cell sizes and chiral angles of semiconducting carbon nanotubes [47]. White and Mintmire's discovery has since been employed to interpret various optical measurements. Two lowest peaks in the absorption spectra of SWNT bundles were assigned to the semiconducting SWNTs, and the third was attributed to the metallic tubes. The energies of the three peaks are approximately $\frac{2a}{d_t}|V_{pp\pi}|$, $\frac{4a}{d_t}|V_{pp\pi}|$, and $\frac{6a}{d_t}|V_{pp\pi}|$, where a is the C–C bond length. However, such interpretations of absorption spectra of SWNTs in bundles or aqueous micellar suspensions, although likely correct, have not been adequately scrutinized. In addition to the DOS, the absorption lineshape also has a nontrivial dependence on the transition dipole moments between pairs of valence and conduction bands. A finite transition dipole projection along the direction of an external field ensures the appearance of an absorption peak, which links two van Hove singularities in the DOS, whereas a zero or negligible transition dipole moment gives no absorption peaks even if the corresponding DOS diverges. Calculated transition dipole moments in the entire Brillouin zone, however, have remained elusive in the literature. Here we start with the tight-binding model and determine the transition dipole field lines of a graphene sheet. The general absorption spectral features of SWNTs shall become obvious from those field lines and plots of the conduction (valence) band contours shown in the previous section.

Aside from the van Hove singularities of optically connected valence/conduction bands, the transition dipole moment is the single most important quantity for the prediction of the optical absorption lineshapes. Depending on the orientation of the external laser field, the transition dipole moment of the SWNTs can assume quite different characteristics thanks to the selection rules. Optical responses of carbon nanotubes are highly anisotropic [48, 49], and the anisotropy of carbon nanotubes has been investigated experimentally by Walt de Heer and his colleagues [50]. The dielectric function ϵ was found being much larger when the electric field is aligned along the tube axis than when it is aligned perpendicular to the tube axis. This can be attributed to the fact that transition dipole along the tubule axis $\mathbf{T}$ is larger than its component perpendicular to the tubes. We consider here first the scenario in which the external field is parallel to the tubule axis ($\mathbf{E} \parallel \mathbf{T}$), and thus the transition occurs exclusively between the orbitals of the same momenta $\mathbf{k}$ [51, 52]. The scenario in which external field is perpendicular to the tubule axis ($\mathbf{E} \perp \mathbf{T}$) involves transitions between orbitals with momenta differing by $\pm\mathbf{k}_1$. This case will be briefly visited at the closing of the section.

If the external field points along the tubule axis, the transition occurs only vertically between states of the same momenta $\mathbf{k}$. Following, we derive and plot the size and orientation of the vertical transition dipole moment in the entire Brillouin zone. Implications about the absorption spectra will be then discussed. For $\mathbf{E} \parallel \mathbf{T}$, the tubule-axis projection of the

transition dipole can be calculated from

$$\mathbf{d}\cdot\mathbf{E} = \langle\phi_c(\mathbf{k})|e\mathbf{E}\cdot\mathbf{r}|\phi_v(\mathbf{k})\rangle \tag{6}$$

where the transition happens between the valence-band wave function $|\phi_v(\mathbf{k})\rangle$ and the conduction-band wave function $|\phi_c(\mathbf{k})\rangle$. Therefore, it is of interest to us to visualize the vector field of the dipole

$$\mathbf{d} = \langle\phi_c(\mathbf{k})|e\mathbf{r}|\phi_v(\mathbf{k})\rangle \tag{7}$$

A brief derivation of the transition dipole $\mathbf{d}$ is as follows. The tight-binding wave function for the conduction (valence) band $|\phi_c(\mathbf{k})\rangle$ ($|\phi_v(\mathbf{k})\rangle$) can be written as

$$|\phi_c(\mathbf{k})\rangle = -\mathbf{c}|\mathbf{A}\rangle + |\mathbf{B}\rangle \tag{8}$$

$$|\phi_v(\mathbf{k})\rangle = \mathbf{c}|\mathbf{A}\rangle + |\mathbf{B}\rangle \tag{9}$$

where $|A\rangle$ ($|B\rangle$) is the Bloch function for the A (B) sublattice so that

$$\langle\mathbf{r}|A\rangle = \sum_{\mathbf{R}_A} e^{i\mathbf{k}\cdot\mathbf{R}_A}\psi_A(\mathbf{r}-\mathbf{R}_A) \tag{10}$$

$$\langle\mathbf{r}|B\rangle = \sum_{\mathbf{R}_B} e^{i\mathbf{k}\cdot\mathbf{R}_B}\psi_B(\mathbf{r}-\mathbf{R}_B) \tag{11}$$

and the coefficient c has the form

$$c = \frac{e^{ik_x/4\sqrt{3}}\sqrt{e^{i\sqrt{3}k_x/2} + 2\cos\left(\frac{k_y}{2}\right) + 2e^{i\sqrt{3}k_x}\cos\left(\frac{k_y}{2}\right) + 4e^{i\sqrt{3}k_x/2}\cos^2\left(\frac{k_y}{2}\right)}}{1 + 2e^{i\sqrt{3}k_x/2}\cos\left(\frac{k_y}{2}\right)} \tag{12}$$

The fact that $|c|^2 = 1$ ensures the orthogonality of the two wave functions, $|\phi_c(\mathbf{k})\rangle$ and $|\phi_v(\mathbf{k})\rangle$. The transition dipole between the two wave fucntions, $\langle\phi_c|e\mathbf{r}|\phi_c\rangle$, is composed of four terms:

$$\langle\phi_c|e\mathbf{r}|\phi_v\rangle = -\langle A|e\mathbf{r}|A\rangle + \langle B|e\mathbf{r}|B\rangle - c^*\langle A|e\mathbf{r}|B\rangle + c\langle B|e\mathbf{r}|A\rangle \tag{13}$$

Among the four terms on the right-hand side of Eq. (13), only the cross terms survive, and after substituting in the Bloch functions, one obtains

$$\langle\phi_c|e\mathbf{r}|\phi_v\rangle = -\frac{c^*}{iV_{pp\pi}}\vec{\nabla}_{\mathbf{k}}H_{12}\langle a|r|b\rangle + \frac{c}{iV_{pp\pi}}\vec{\nabla}_{\mathbf{k}}H_{21}\langle b|r|a\rangle \tag{14}$$

where $r = |\mathbf{r}|$, the off-diagonal Hamiltonian matrix element

$$H_{12} = V_{pp\pi}\sum_{i=1}^{3} e^{i\mathbf{k}\cdot\mathbf{R}_i} \tag{15}$$

with $\mathbf{R}_i$ ($i = 1, 2, 3$) connecting three nearest-neighbor B-lattice points to an A-lattice point, and $|a\rangle$ and $|b\rangle$ being two neighboring wave functions of the A and B sublattices, respectively

$$\langle\mathbf{r}|a\rangle = \psi_A(\mathbf{r}-\mathbf{R}_A) \tag{16}$$

$$\langle\mathbf{r}|b\rangle = \psi_B(\mathbf{r}-\mathbf{R}_A-\mathbf{R}_i), \qquad i = 1, 2, 3 \tag{17}$$

To arrive at Eq. (14), one has taken advantage of the symmetry of the π orbitals

$$\langle b|\mathbf{r}|a\rangle = |\mathbf{R}_{ab}|^{-1}\mathbf{R}_{ab}\langle b|r|a\rangle \tag{18}$$

where the A sublattice point a is taken as the origin without loss of generality, and $\mathbf{R}_{ab}$ labels the vector pointing from point a to point b.

The sizes and orientations of **d** as a function of the wave vector **k** are shown in Fig. 2c. The transition dipoles form circular patterns around K points and are prominent along lines connecting neighboring K points. The oscillator strength, therefore, is mainly concentrated in the vicinities of the Brillouin zone boundaries; that is, in areas between neighboring K points. One main feature of the **d** orientations is that the transition dipole points tangentially around the K points, forming pseudo-vortices centered at the K points (cf. Fig. 2c). This is significant because the transition dipole consequently has sizable projections along the tubule axis direction around the K points regardless of any nanotube chirality.

Close to the Brillouin zone centers, the size of the transition dipole vanishes asymptotically. This can be understood as follows: At the Brillouin zone center ($\mathbf{k} = 0$), the transition dipole size has to vanish because of symmetry considerations (i.e., to avoid choosing an orientation at the Γ point). Around the zone center, the transition dipole size has the following property

$$|\mathbf{d}|(k_x = 0, k_y \approx 0) = \frac{k_y^2}{9\sqrt{3}} + O[k_y]^4, \qquad |\mathbf{d}|(k_x \approx 0, k_y = 0) = \frac{k_x^2}{9\sqrt{3}} + O[k_x]^4 \tag{19}$$

Therefore, the oscillator strength roughly scales with $|\mathbf{k}|^4$ around the zone center. Along M–Γ–M lines, the transition dipoles are found parallel to the M–Γ–M lines, whereas along K–Γ–K lines, transition dipoles are perpendicular to the K–Γ–K lines.

In the literature, the optical absorption spectra are often calculated from a matrix element containing the momentum operator **P** [52–54]

$$\langle \phi_c(\mathbf{k}) | \mathbf{P} \cdot \mathbf{E} | \phi_v(\mathbf{k}) \rangle \tag{20}$$

This matrix element is proportional to the transition dipole moment we have calculated, as shown by

$$i\hbar\dot{\mathbf{r}} = [\mathbf{r}, \mathbf{H}] \tag{21}$$

where **H** is the nanotube Hamiltonian.

If the external electric field points perpendicular to the tubule axis, the selection rule dictates that the transition dipole take the form [52, 53, 55]

$$\mathbf{d}' \cdot \mathbf{E} = \langle \phi_c(\mathbf{k}) | e\mathbf{E} \cdot \mathbf{r} | \phi_v(\mathbf{k} \pm \mathbf{k}_1) \rangle \tag{22}$$

Similarly, the vector field of the transverse transition dipole $\mathbf{d}'$

$$\mathbf{d}' = \langle \phi_c(\mathbf{k}) | e\mathbf{r} | \phi_v(\mathbf{k} \pm \mathbf{k}_1) \rangle \tag{23}$$

now assumes the importance of the vertical transition dipole **d** field in the previous discussions.

2.3. The Absorption Intensities

The quasi-one-dimensionality of SWNTs gives rise to sharp van Hove peaks in the density of electronic states. Optical properties of SWNTs are thus dominated by transitions between corresponding van Hove singularities on opposite sides of the Fermi level. Contributions to the absorption lineshape from excitations polarized along the tubule axis at the momentum **k** are determined by two factors; namely, the transition dipole **d** projected along the tubule axis $\mathbf{T} \cdot \mathbf{d}$, and the nanotube DOS for the corresponding conduction (valence) band at **k**, which is precisely $(\mathbf{T} \cdot \nabla_{\mathbf{k}} E_c)^{-1}$ $[(\mathbf{T} \cdot \nabla_{\mathbf{k}} E_v)^{-1}]$. In other words, the absorption intensity is proportional to $(\mathbf{T} \cdot \mathbf{d})^2 (\mathbf{T} \cdot \nabla_{\mathbf{k}} E_c)^{-1} (\mathbf{T} \cdot \nabla_{\mathbf{k}} E_v)^{-1}$. Therefore, except where the $\mathbf{k}_2$ cuts are perpendicular to the transition dipole **d** field lines, or where the transition dipole **d** vanishes, the shape of the absorption spectra is determined mostly by the density of states of the nanotube bands [53]. For external excitation fields along the tubule axis, as is the case under discussion here, vertical transitions in the **k** space are expected, and one needs to find out how the DOS contours lines of the graphite conduction (or covalence) band relate to the tubule axis. The contour lines of the conduction band E_c is depicted in Fig. 2b. When the

tubule axis is tangential to a contour line of E_c at a given $\mathbf{k}$, $(\mathbf{T}\cdot\nabla_{\mathbf{k}}E_c)^{-1}$ diverges, and a van Hove singularity appears in the DOS. Because E_c and E_v are mirror images of each other under the approximation that neglects the overlap integral between adjacent carbon atoms, $(\mathbf{T}\cdot\nabla_{\mathbf{k}}E_v)^{-1}$ also diverges at that particular $\mathbf{k}$. If the transition dipole between the valence and conduction orbitals has a nonzero projection along $\mathbf{T}$ at that $\mathbf{k}$, a corresponding peak arises in the absorption spectrum. Of particular interest are those K and M points in the Brillouin zone. An intersect through the K points does not cause a van Hove singularity, but adjacent intersects do, as noted by White and Mintmire. For metallic SWNTs, two intersects with a spacing $\frac{2}{d_t}$ from the K point have van Hove singularities. Because the energy contours are nearly circular around the K point (cf. Fig. 2b), $E_c - E_v$ at both van Hove singularities can be approximated by $\frac{6a}{d_t}|V_{pp\pi}|$. For semiconducting tubes, no intersect goes through K points. The closest intersect to a K point is $\frac{2}{3d_t}$ from the K point, and the next closest is $\frac{4}{3d_t}$ from the K point; $E_c - E_v$ at the two van Hove singularities are $\frac{2a}{d_t}|V_{pp\pi}|$ and $\frac{4a}{d_t}|V_{pp\pi}|$, respectively. Similarly, any intersects at the M points or their vicinities may lead to van Hove singularities. Because the M points are saddle points at which $E_c - E_v$ are relatively flat, transition energies linking these van Hove singularities are approximately $2|V_{pp\pi}|$.

Neither the oscillator strength nor the DOS alone determines the optical absorption lineshapes of the SWNTs. One is therefore led to study the combined effect of the two competing factors. Figure 3 plots the product of the $E_c(\mathbf{k})$ DOS and the oscillator strength, which combines the effects of the transition dipole and DOS on the absorption spectra

$$|\mathbf{d}|^2|\vec{\nabla}_{\mathbf{k}}E_c(\mathbf{k})|^2 = |\langle\phi_c(\mathbf{k})|e\mathbf{r}|\phi_v(\mathbf{k})\rangle|^2|\vec{\nabla}_{\mathbf{k}}E_c(\mathbf{k})|^2 \tag{24}$$

The vanishing oscillator strength annihilates the DOS singularity at the Brillouin zone center. The contour plot that corresponds to the accompanying three-dimensional plot of $|\mathbf{d}|^2|\vec{\nabla}_{\mathbf{k}}E_c(\mathbf{k})|^2$ in Fig. 3 therefore resembles Fig. 2d.

For (5, 5) nanotubes, for example, the external laser field along the nanotube axis is parallel to the energy intersects or the parallel lines in Fig. 2a. Except when an intersect (see Fig. 2a) is orthogonal to the $\mathbf{d}$ field line at momentum $\mathbf{k}$, the transition dipole will have a nonzero component along the external field. Because the $\mathbf{d}$ field lines near the K points are, to the lowest order, circular in pattern, any intersects in its vicinity are guaranteed not to be perpendicular to the $\mathbf{d}$ field lines. It follows that any transitions linking the van Hove singularities near the K points are allowed. Therefore, armed with plots of the conduction (valence) band contours and the transition dipole field lines of the graphene (i.e., Fig. 2b and 2c), we have proven that the lowest-energy peaks in both metallic and semiconducting tubes depend only on the diameter; for tubes of approximately the same diameters, the two lowest-energy peaks from the semiconducting tubes are about 1/3 and 2/3 in energy, respectively, when compared with the lowest-energy peaks from the metallic tubes. The $\mathbf{d}$ field lines near an M point are approximately parallel to each other. If an intersect is perpendicular to the $\mathbf{d}$ field lines near one M point, as a result of the existence of six equivalent M points in

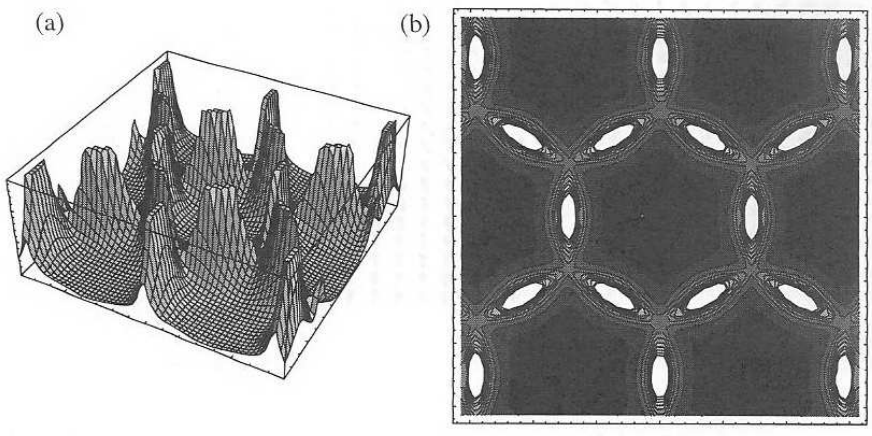

Figure 3. Combined effect of the transition dipole and the SWNT DOS: (a) three-dimensional plot of $|\mathbf{d}|^2|\vec{\nabla}_{\mathbf{k}}E_c(\mathbf{k})|^2$ in the Brillouin zone, and (b) its corresponding contour.

the first Brillouin zone, the same set of intersects parallel to the tubule axis will not be perpendicular to the field lines near the other five M points. We thus expect to observe the absorption peaks attributed to transitions at the M points or in their vicinities, with transition energies at about $2\,|V_{pp\pi}|$. This is helped by the fact that the graphene's oscillator strength, which is proportional to $|\mathbf{d}|^2$, is mainly concentrated near the Brillouin zone boundaries, and especially around the M points, as mentioned earlier from Fig. 2d. Close to the Brillouin zone center, contributions to the absorption lineshapes are weak at best, as the size of the transition dipole vanishes asymptotically at $\mathbf{k} = 0$.

Similar to the orientation plot of transition dipoles in Fig. 2c, the Hamiltonian field of the conduction band also forms vortices around the K points. The area near the M and K points is amplified in Fig. 4a. The Hamiltonian fields along the K–M–K line points almost perpendicular to the K–M–K lines. Therefore, the areas close to the M–K lines are potential candidates for generating absorption peaks as the intersects, or the $\mathbf{k}_2$ cuts, are quite likely tangential to the contour lines along M–K lines. This shall become clearer later. Another stunning feature of the conduction-band Hamiltonian field is that along the M–M lines, the Hamiltonian field points straight toward, or away from, the M points. As a consequence for zigzag $(n, 0)$ tubes, for which all $\mathbf{k}_2$ cuts are parallel to the M–M lines, the $\mathbf{k}_2$ cuts that are close to the M–M lines will contain a finite momentum bracket within which the contour lines are parallel to the tubule axis, and the SWNT DOS diverges. This has implications for the absorption lineshapes calculated by the tight-binding model. For zizag SWNTs, the tight-binding spectra will therefore have large intensities at the energies corresponding to the vicinities of the M–M lines. The spectral contributions from various $\mathbf{k}_2$ cuts for the (9,0) are tabled in Fig. 4b, labeled by μ. The $\mu = 4$ and $\mu = 5$ cuts are close to the M–M lines and are responsible for high-intensity contributions to the absorption spectra over a wide energy range.

For armchair SWNTs, the allowed states, or the $\mathbf{k}_2$ energy cuts, are analogous to the vertical lines in Fig. 2a, which are specifically the $\mathbf{k}_2$ cuts for the $(5, 5)$ tube. To obtain a precise line along which DOS of any armchair SWNT diverges in the vicinities of the K–M–K line, one needs only to solve

$$\mathbf{e}_x \cdot \vec{\nabla}_{\mathbf{k}} E_c(\mathbf{k}) = 0 \tag{25}$$

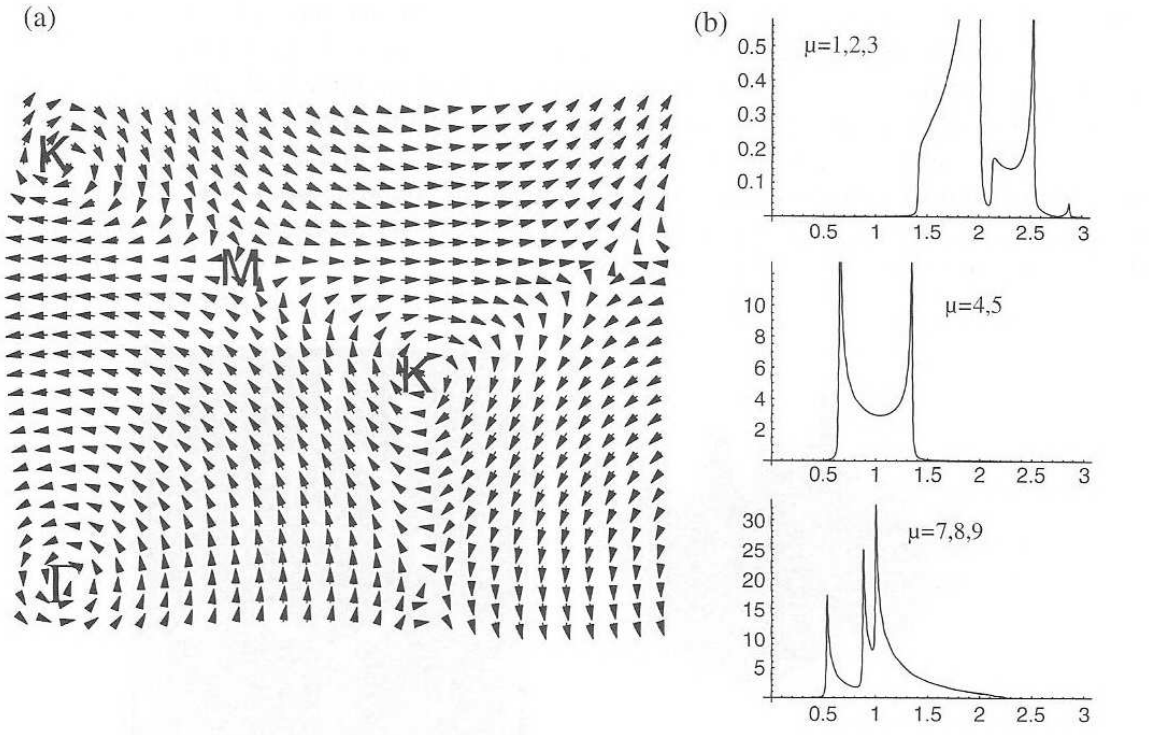

Figure 4. (a) The area near the M and K points is amplified for the Hamiltonian field of the SWNT conduction band; (b) the spectral contributions from various $\mathbf{k}_2$ cuts for the $(9, 0)$ are tabled. Cuts are labelled by μ. The $\mu = 6$ cut goes through the K point, and therefore, it is not listed.

which leads to

$$\cos\frac{\sqrt{3}k_x}{2} + 2\cos\frac{k_y}{2} = 0 \tag{26}$$

The trajectory determined by Eq. (26), as shown by the curvy line in Fig. 5, is very close to the straight line connecting M and K points. For zigzag SWNTs, in contrast, the $\mathbf{k}_2$ cuts are perpendicular to the K–M–K line, which implies that the SWNT DOS diverges on the K–M–K line, and all tight-binding absorption peaks for zigzag SWNTs can be attributed to the points on the K–M–K line. For nanotubes of any other chiralities, the corresponding tight-binding low energy absorption peaks can be attributed to the tiny area in the Brillouin zone that is bordered by the M–K line and the curvy line given by Eq. (26), as shown by the shaded area in Fig. 5.

Recently, Grüneis et al. pointed out an intensity node in optical absorption spectra of a graphene sheet as a function of the electron wave vector $\mathbf{k}$ and the light polarization around the K points in the two-dimensional Brillouin zone [53]. This is in full agreement with the transition-dipole plot, Fig. 2c. For example, in the vicinities of the K points, for a vertical light polarization in Fig. 2c, that is, $\mathbf{E} \parallel \mathbf{k}_y$, there will be zero absorption intensity at wave vectors $\mathbf{k}$, which are on the vertical lines going through the K points. Similarly, for $\mathbf{E} \parallel \mathbf{k}_x$ in Fig. 2c, zero absorption intensity at wave vectors $\mathbf{k}$, which are on the horizontal lines going through the K points. The two nodes on the two sides of the K points, however, are not equivalent, which is also clearly demonstrated in Fig. 2c (cf. Fig. 2 of Ref. [53]).

Optical spectroscopy has been used to reveal detailed composition of bulk SWNT samples providing distributions in both tube diameter and chiral angle. For semiconducting SWNTs, those measurements used small deviations of absorption peaks' dependence on diameter from a linear relation, which can be accounted for qualitatively by the tight-binding model here. For instance, Bachilo et al. observed that the energy ratios between the second and first van Hove singularities, often referred to as E_{22}/E_{11} (E_{22} and E_{11} label the second and first van Hove singularities, respectively), deviate from a central value in the opposite directions for semiconducting nanotubes with $(n - m) \bmod 3 = 1$ and those with $(n - m) \bmod 3 = 2$ [35]. This can be explained by the fact that for wave vectors sufficiently apart from the K points, the energy slope along the K–Γ lines is much steeper than that along the K–M lines (cf. Fig. 2b and Fig. 6).

More features in Fig. 2 of Ref. [35] can be explained intuitively by the graphical tools developed here. In Fig. 6, allowed states for a zigzag semiconducting SWNT can be represented by solid horizontal lines that are perpendicular to the dotted vertical K–Γ line. As the energy slope difference on the two sides of the K point is the largest along the vertical K–Γ line among all lines going through the K point (cf. Fig. 6), zigzag SWNTs exhibit highest deviations of the energy ratios E_{22}/E_{11} from the value two. Furthermore, for zigzag SWNTs, the energy ratio E_{22}/E_{11} for the case of $(n - m) \bmod 3 = 2$ [$(n - m) \bmod 3 = 1$] is below (above) the value two, as clearly demonstrated in Fig. 6a (Fig. 6b). On the other hand, for metallic armchair nanotubes, for which the trigonal warping effect is absent due to

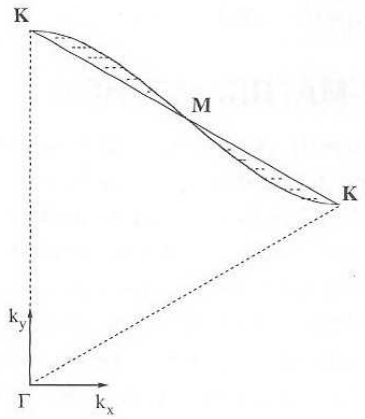

Figure 5. The vicinities of the M–K–M line in the Brillouin zone.

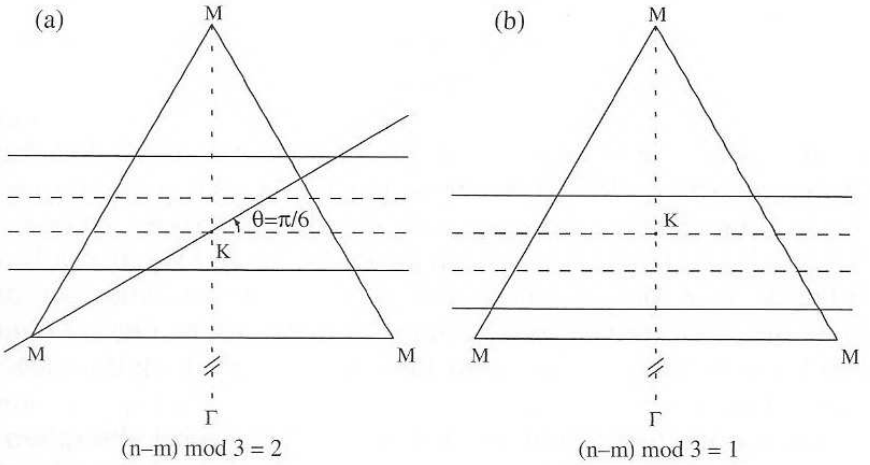

Figure 6. Horizontal solid parallel lines are the allowed states in the Brillouin zone for (a) a zigzag nanotube with $(n - m)$ mod 3 = 2, and (b) a zigzag nanotube with $(n - m)$ mod 3 = 1. Dashed parallel lines divide the distance between the solid lines into three equal parts. One of the two dashed lines goes through the K point. The tilted solid line in (a) connecting the M and K points represents a part of allowed states for armchair nanotubes. Dotted lines connect the K and Γ points. Reprinted with permission from [43], Y. Zhao et al., *Chem. Phys. Lett.* 387, 149 (2004). © 2004, Elsevier B. V.

symmetry, the allowed states are represented by lines that are parallel to the tilted solid line connecting M and K points in Fig. 6a (equivalent to the dashed parallel lines in Fig. 2a). For non-armchair metallic SWNTs, the trigonal warping effect brings about a splitting in the first absorption peak in the tight-binding model, as was elaborated by Saito et al. [44] Phonon spectra have recently been used to verify the existence of singularity splitting in the joint density of electronic states in non-armchair metallic SWNTs [56, 57].

Among semiconducting nanotubes, the one with $n - m = 1$ has allowed states that are on lines with the smallest deviation angle from the tilted M–K line in Fig. 6a, and consequently E_{22}/E_{11} for $n - m = 1$ are closest to two. The set of parallel lines representing allowed nanotube states is not unique. Because of the sixfold symmetry of the Brillouin zone, the angle θ between the solid horizontal lines in Fig. 6a and parallel lines representing allowed states for *any* SWNT can be narrowly confined to be within $\pi/6$. This implies that the energies of allowed states for all SWNTs behave in a similar way as those of the zigzag nanotubes. Differing energy slopes of allowed states on the two sides of the K point cause E_{22}/E_{11} to deviate from two, the direction of which depends on whether $(n - m)$ mod 3 equals 1 or 2. As the angle θ approaches $\pi/6$ (for $n - m = 1$, for example), $|E_{22}/E_{11} - 2|$ minimizes. This also explains why deviation of E_{22}/E_{11} from the value two increases with $n - m$ (and with $|\theta - \pi/6|$) as was observed in Ref. [35].

A rigorous proof has been given here to these interpretations of the experimental results [29, 31, 33, 58] on the low-energy peaks in the absorption spectra of SWNTs. In contrast to those low-frequency features, common absorption peaks attributed to the M points and their vicinities remain to be observed experimentally for SWNTs of various sizes and chiralities. Orbital hybridization and electronic correlations are also more likely to affect higher energy excitations, which makes their experimental confirmations less certain.

3. LOCALIZED-DENSITY-MATRIX METHOD

The prediction of White and Mintmire [46] about the low-lying absorption peaks of SWNTs, and that from the tight-binding model as discussed in length in the previous section, consider only explicitly the π electrons. Rehybridization of σ and π orbitals and electronic correlations are known to affect the band structure, DOS, and transition dipoles of SWNTs and may thus lead to substantial changes of optical absorption spectra. Therefore, more realistic calculations beyond the tight-binding model are needed to examine the implications of White and Mintmire's discovery for optical absorption. In this section we calculate SWNT optical absorption spectra by including explicitly the electron–electron correlations and the σ–π orbital rehybridization in the framework of the LDM method based on the TDHF approximation [48].

In the LDM approach, electronic correlations are taken into account within the framework of TDHF approximation or random phase approximation (RPA) [59]. We have the following equation for the linear response of the density matrix deviation $\delta\rho$ from its ground-state value $\rho^{(0)}$

$$\left(i\hbar\frac{d}{dt}+\gamma\right)\delta\rho(t)=\left[h^{(0)},\delta\rho(t)\right]+\left[\delta h(t),\rho^{(0)}\right]-\mathbf{E}(t)\cdot\left[\mathbf{P},\rho^{(0)}\right] \tag{27}$$

The following approximations are employed to achieve the linear-scaling calculation for the excited state properties [60, 61, 49]:

$$\rho^{(0)}{}_{ab}^{mn}=0 \quad \text{if} \quad r_{ab}>l_0$$
$$\delta\rho_{ab}^{mn}=0 \quad \text{if} \quad r_{ab}>l_1$$

where r_{ab} is the distance between two atoms a and b, and l_0 and l_1 are two cut-off lengths. The DOS operator can be defined as

$$\hat{\sigma}=\sum_m |m\rangle\langle m|\delta(E-E_m) \tag{28}$$

where $|m\rangle$ is the state m, and E_m is its energy. The DOS of a system is then given by [62]

$$\sum_m \delta(E-E_m)=\mathrm{Tr}\hat{\sigma}(E)=\frac{1}{\pi}\mathrm{Im}\sum_m \lim_{\eta\to 0^-}\frac{1}{E-E_m-i\eta} \tag{29}$$

If the $|m\rangle$ is a Hartree–Fock molecular orbital, Eq. (29) gives the one-electron DOS.

The LDM method has been developed to evaluate the ground- and excited-state properties of very large systems [48, 49, 60, 61, 63–67], which is facilitated by the truncation of the reduced single-electron density matrices. As a result, the computation time of the LDM method can be scaled linearly with the system size. The LDM method has been used to determine the absorption spectra of a few open-ended zigzag SWNTs [49]. The PPP Hamiltonian, which considers only the π electrons, is adopted first in the computation. The fast multipole method (FMM) method is employed to test linear-scaling properties of the calculations [49]. SWNTs are often regarded as one-dimensional nanostructures because their lengths are far greater than their diameters. To illustrate that the LDM method is applicable to three-dimensional systems, we consider the nanotubes with diameters comparable to their lengths. The diameters range from 20.37 to 81.48 Å, and the lengths from 15.63 to 66.78 Å. The number of carbon atoms corresponds to 416, 1664, 3328, 4576, and 6656. The CPU time for propagating the TDHF equation of motion for the single-electron reduced density matrix between a time interval of [−0.5 fs, −0.3 fs] is recorded. The time step is 0.01 fs. The critical lengths l_0 and l_1 are set to be 15 Å. The results are shown in Fig. 7a. The CPU time scales linearly with the system size N. The maximum number of atoms in the smallest box is kept at 26. The corresponding absorption spectrum of a SWNT with 1200 carbon atoms is shown in Fig. 7b. The critical cutoff lengths l_0=28 Å and l_1=43 Å are used. The calculated absorption spectrum, which differs significantly from those of one-dimensional SWNTs, resembles those of graphite [68] if the nanotube radius is large enough.

The curvature of the tube leads to some sp^3 hybridization of π and σ orbitals. Orbital hybridization, which increases with decreasing tube diameters, may alter significantly the zero-order band structure of the SWNTs. Thus, a more realistic model that includes all valence orbitals is needed to describe accurately the electronic structures of the SWNTs, especially those of the capped ones. Semiempirical methods such as CNDO/S [69], INDO [70], MNDO [71], and AM1 [72] consider explicitly all valence electrons including σ electrons in SWNTs. The LDM method using the CNDO/S Hamiltonian was employed for spectral calculations of poly(p-phenylenevynelene) aggregates [67]. Stewart reparametrized MNDO to an MNDO-PM3 (MNDO parametric method 3) or a PM3 [73] Hamiltonian, which substantially reduces errors in calculations of the heats of formation as compared with the MNDO and AM1 Hamiltonians. The PM3 Hamiltonian has been employed to

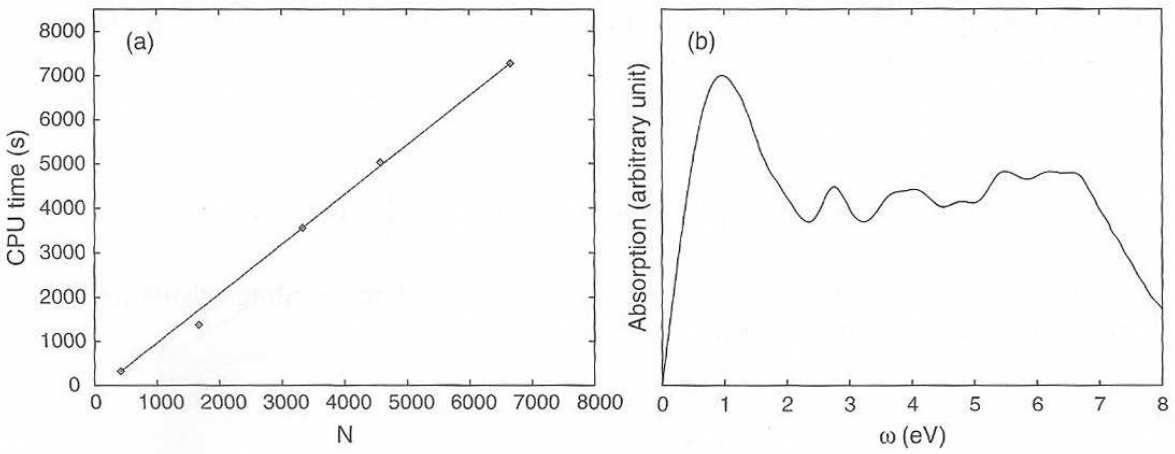

Figure 7. (a) CPU time for the excited-state calculation of three-dimensional CNTs with a large radius. The time interval is [−0.5 fs, −0.3 fs] with the time step 0.01 fs. The critical length l_0 and l_1 are 15 Å. Twenty-six atoms are included in the smallest box. (b) Absorption spectrum of the zigzag (60, 0) nanotube $C_{1200}H_{120}$. $\gamma = 0.4$ eV. Reprinted with permission from [49], W. Z. Liang et al., *J. Am. Chem. Soc.* 104, 2445 (2000). © 2000, American Chemical Society.

calculate the absorption spectra of organic compounds [74–76]. For the remainder of the section, the LDM-PM3 method will be used for calculations of SWNT optical absorption spectra.

A series of SWNTs have been investigated systematically for their optical properties by the LDM method [49, 65, 66]. Two types of dipole-induced excitations have been identified; namely, the end modes (low energy, $\omega < 1.0$ eV) and tube modes (high energy, $\omega > 1.0$ eV). The low-energy excitations are electron–hole pairs confined within the two ends of SWNTs, and the higher energy excitations are located mainly along the tube [65]. Those SWNTs whose optical properties have been calculated are mainly armchair and zigzag SWNTs, and their diameters are much greater than 4 Å. It was found that the absorption spectra of large-diameter carbon nanotubes are determined mainly by their diameters, with a weak dependence on their chiralities.

As early as in 1992, Sawada and Hamada [77] predicted the existence of extremely thin tubules; for instance, 4-Å SWNTs. They calculated the cohesive energies of the SWNTs using the Tersoff's empirical potential for carbon [78] and showed that SWNTs of all diameters, large and small, are energetically more favorable than the graphite sheets of the same width. They thus suggested that the 4-Å SWNTs may exist. Recently, both 4-Å SWNTs and multi-walled CNTs containing 4-Å SWNTs have been synthesized by the mass-selected carbon ion beam deposition (MSIBD) method [79, 80] and the pyrolysis of tripropylamine molecules in channels of porous zeolite $AlPO_4$–5 (AFI) single crystals [32], respectively. The 4-Å SWNTs have three possible structures: the chiral (4, 2) SWNT, the zigzag (5, 0) SWNT, and the armchair (3, 3) SWNT. Their diameters are 4.2, 3.9, and 4.1 Å, respectively. It has been argued that the 4-Å CNTs may be either (3, 3) or (5, 0) because they fit well with the half fullerene C_{20} cap [79]. The corresponding electronic structures and optical properties have been measured experimentally [81]. Three major absorption peaks at 1.35, 2.15, and 3.10 eV are identified in the absorption spectra when the electric field is parallel to the tubes. When the external field is perpendicular to the tube axis, the CNTs are almost transparent, with a very weak absorption peak at an energy slightly lower than 1.35 eV [81].

We first outline the implementation of the LDM method at the PM3 level denoted as the LDM-PM3 method. Next, in Section 3.2 we investigate electronic structures and optical properties of SWNTs of various chiralities, caps, and lengths. The nature of dipole-induced excitations is examined by projecting the corresponding reduced single-electron density matrices onto the Hartree–Fock molecular orbital (HFMO) representation. In Section 3.3, we report calculations of optical absorption spectra of the (4, 2), (3, 3), and (5, 0) SWNTs with diameters around 4 Å [65]. The anisotropy of absorption spectra is investigated by calculating the dynamic polarizabilities for various light polarizations. In Section 3.4, we study the effect of functionalization on metallic SWNTS with the help of the LDM-PM3 method.

3.1. The PM3 Hamiltonian

The PM3 Hamiltonian in the presence of an external field $\mathbf{E}$ is described as follows,

$$\begin{aligned} H &= H_e + H_{\text{ee}} + H_{\text{ext}} \\ H_e &= \sum_{ab}\sum_{mn} H_{ab}^{mn} c_{am}^{\dagger} c_{bn} \\ H_{\text{ee}} &= \frac{1}{2}\sum_{ab}\sum_{mnij} V_{ab}^{mn,ij} c_{an}^{\dagger} c_{bi}^{\dagger} c_{bj} c_{am} \\ H_{\text{ext}} &= -\mathbf{E}(t)\cdot\widehat{\mathbf{P}} \end{aligned} \tag{30}$$

where $c_{am}^{\dagger}$ (c_{bn}) is the creation (annihilation) operator for an electron at a localized atomic orbital m (n) on atom a (b). One-electron integral H_{ab}^{mn} may be expressed as

$$H_{ab}^{mn} = \left\langle \chi_a^m \left| -\frac{1}{2}\nabla_{\mathbf{r}}^2 + U(\mathbf{r}) \right| \chi_b^n \right\rangle \tag{31}$$

where χ_a^m (χ_b^n) is the m (n)-th atomic orbital on atom a (b) and $U(\mathbf{r})$ is the one-electron potential. The Hamiltonian H_{ee} is the two-electron part of the Hamiltonian that represents the effective electron–electron Coulomb interaction. The PM3 model uses the neglect of differential overlap for atomic orbitals on different atoms; that is, all the two-electron integrals are set to zero except that when the orbitals m and n belong to the same atom a and i and j belong to atom b. The term $V_{ab}^{mn,ij}$ is expressed as

$$V_{ab}^{mn,ij} = \langle \chi_a^n(1)\chi_b^i(2)|V(r_{12})|\chi_a^m(1)\chi_b^j(2)\rangle \tag{32}$$

The Hamiltonian H_{ext} is the interaction between the valence electrons and an external electric field $\mathbf{E}(t)$, and $\widehat{\mathbf{P}}$ is the molecular dipole moment operator. As a consequence, the Fock matrix h may be written as

$$h_{ab}^{mn} = H_{ab}^{mn} + 2\delta_{ab}\sum_{c}\sum_{ij\in c} V_{ac}^{mn,ij}\rho_{cc}^{ij} - \sum_{i\in a}\sum_{j\in b} V_{ab}^{mi,jn}\rho_{ab}^{ij} \tag{33}$$

Similarly, the induced Fock matrix may be expressed as

$$\delta h_{ab}^{mn} = 2\delta_{ab}\sum_{c}\sum_{ij\in c} V_{ac}^{mn,ij}\delta\rho_{cc}^{ij} - \sum_{i\in a}\sum_{j\in b} V_{ab}^{mi,jn}\delta\rho_{ab}^{ij} \tag{34}$$

3.2. Absorption Spectra of Carbon Nanotubes

To test the validity of the PM3 model for determining optical spectroscopy, we calculate the absorption spectrum of a C_{60} molecule. The result is demonstrated in Fig. 8. The geometry optimization for C_{60} is carried out at the Hartree–Fock level, using the PM3 Hamiltonian. The calculated energies of the first three main absorption peaks in C_{60} are 3.8, 4.6, and 5.7 eV, which compare well to the corresponding experimental values of 3.7, 4.6, and 5.7 eV for C_{60} in the n-hexane solution [82]. The calculations are performed using our LDM program with inclusion of all reduced single-electron density matrix elements (i.e., a full TDHF calculation).

A series of CNTs with different chiralities and ends are investigated, and their absorption spectra are determined. The external field is polarized along the tube axis in all calculations. Most CNTs' geometries are optimized at the Hartree–Fock level except those specified otherwise in the text. In our calculations, open-ended CNTs are terminated with hydrogen atoms or other functional groups. Capped CNTs are closed with fullerene-like cages that contain only hexagonal and pentagonal faces. For instance, a C_{60} molecule is bisected at its equator, and the two resulting half spheres may be attached to a open-ended (5, 5) armchair tube or (9, 0) zigzag tube depending on the way that the C_{60} molecule is cut. Six pentagons are needed to form a cap for (5, 0) tube, and six pentagons together with one hexagon for

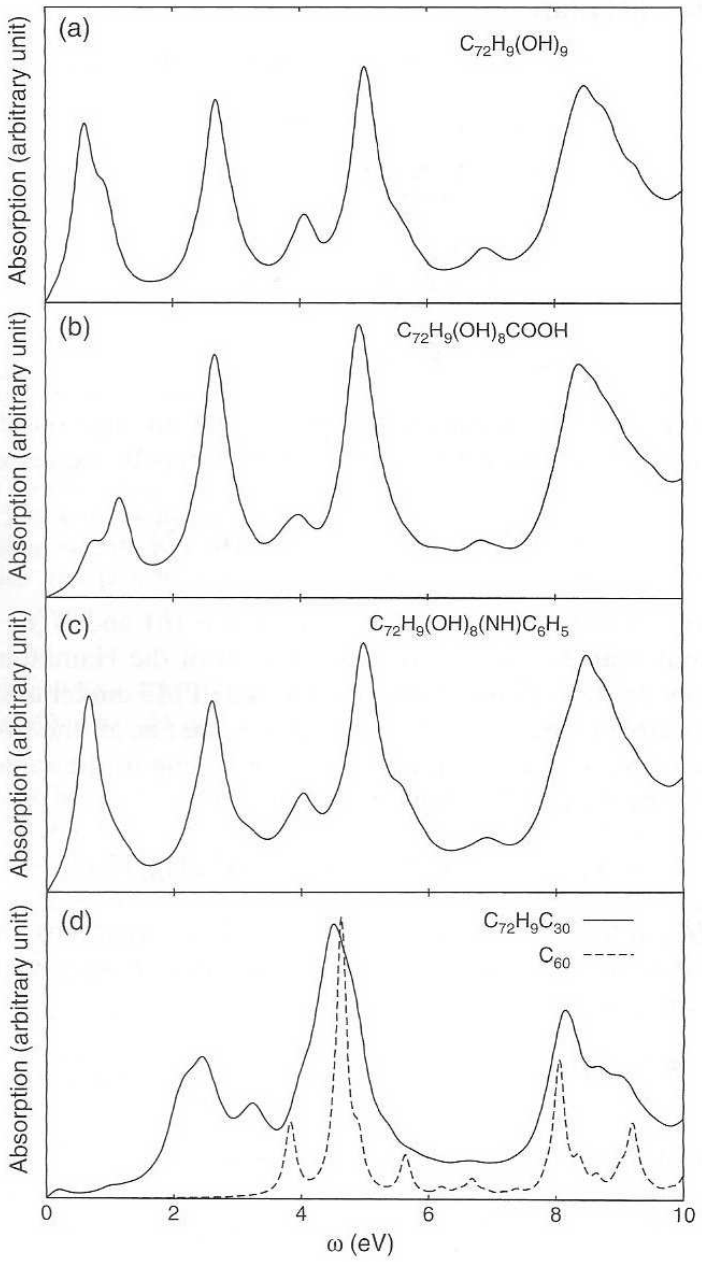

Figure 8. Calculated absorption spectra of C_{60} with dephasing parameter $\gamma = 0.1$ eV and the (9, 0) CNTs with $\gamma = 0.2$ eV. (a), (b), (c), and (d) are the absorption spectra for $C_{72}(H)_9(OH)_9$, $C_{72}(H)_9(OH)_8(COOH)$, $C_{72}(H)_9(OH)_8(NH)(C_6H_5)$, and $C_{72+39}H_9$ by full TDHF, respectively. All the geometries are optimized on the HF level with the PM3 Hamiltonian. Reprinted with permission from [65], W. Z. Liang et al., *J. Am. Chem. Soc.* 122, 11129 (2000). © 2000, American Chemical Society.

(6, 0) tube, as a total of 12 pentagons are needed to form a closed polygon, which is required by the Euler's theorem and sp^2 hybridization.

The influence of two ends on the optical properties of CNTs is examined. The calculated absorption spectra are shown in Fig. 8 for (9, 0) CNTs of same length but different ends. Figure 8a, 8b, 8c, and 8d shows the spectra of $C_{72}H_9(OH)_9$ (one end with —OH and another end with hydrogens), $C_{72}(OH)_8H_9$ (COOH) (one —OH is replaced by —COOH), $C_{72}(OH)_8H_9(NH)C_6H_5$, (one —OH is replaced by $—(NH)C_6H_5$), and $C_{72+30}H_9$ (one end with caps, another end with hydrogens), respectively. Similar line shapes are observed for $\omega >$ 2.0 eV in all spectra. The peaks centered at about 2.7, 4.0, 5.0, 6.9, and 8.0 eV are observed in all systems and are attributed to the excitations along the tubes. They are not much influenced by the different terminating functional groups. Differences appear for $\omega < 2.0$ eV, which should correspond to the excitations at two tube ends. The highest occupied molecular orbits (HOMOs) and lowest occupied molecular orbits (LUMOs) of CNTs have large components at the ends. This is further verified by the density matrices of low-energy excitations.

The physical properties of infinite CNTs are determined by their chiralities and radii [22, 83–86]. For finite size tubes, we find that the tube length also plays a vital role in the electronic structure. Figures 9 and 10 are the calculated absorption spectra of different-size (9, 0) and (5, 5) CNTs. Figure 9 shows absorption spectra of capped (9, 0) CNTs. As the number of carbon atoms increases from 78 to 222 (Fig. 9a–d), the peaks at $\omega < 6.0$ eV red-shift, although these near 8.0 eV change little. As a consequence of the red-shift, the line shapes differ for $\omega < 6.0$ eV until a saturation is reached. The absorption spectra of open-ended (9, 0) tubes differ drastically from those of capped (9, 0) CNTs, especially when the tube lengths are short. Low-energy peaks ($\omega < 2.0$ eV) for $C_{72}H_9(OH)_9$ (Fig. 8a) disappear in the absorption spectrum of C_{72+60} (Fig. 9c). The absorption spectrum of the open-ended (9, 0) tube changes drastically with increasing size. The first two peaks of $C_{72}H_9(OH)_9$ disappear when the number of carbon atoms increases to 162, whereas the third peak shifts below 2.0 eV. Investigation of corresponding density matrices reveals that the first peak for $C_{72}H_9(OH)_9$ corresponds to the electron–hole pairs located at two ends. The two ends play an important role in the optical response of short, open-ended zigzag tubes, and their

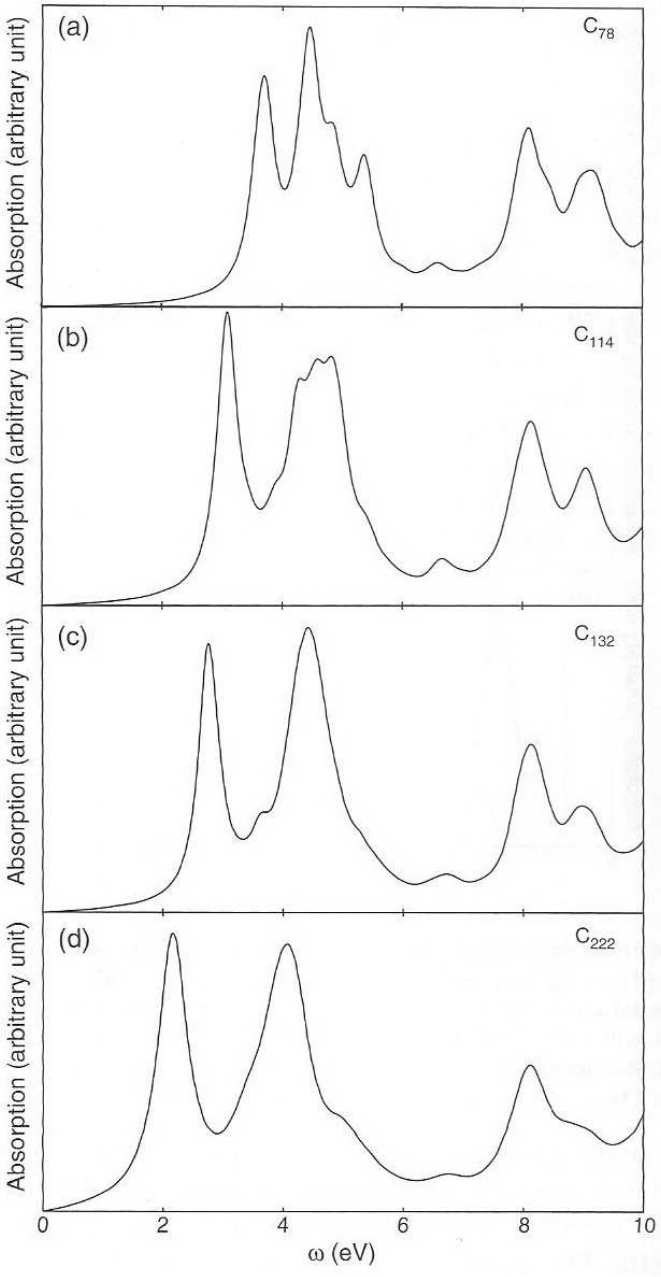

Figure 9. Absorption spectra of capped (9, 0) tubes calculated by full TDHF and LDM method. (a), (b), and (c) are the results calculated by full TDHF with $\gamma = 0.2$ eV, and (d) is the result of LDM with $\gamma = 0.3$ eV. All the geometries are optimized. Reprinted with permission from [65], W. Z. Liang et al., *J. Am. Chem. Soc.* 122, 11129 (2000). © 2000, American Chemical Society.

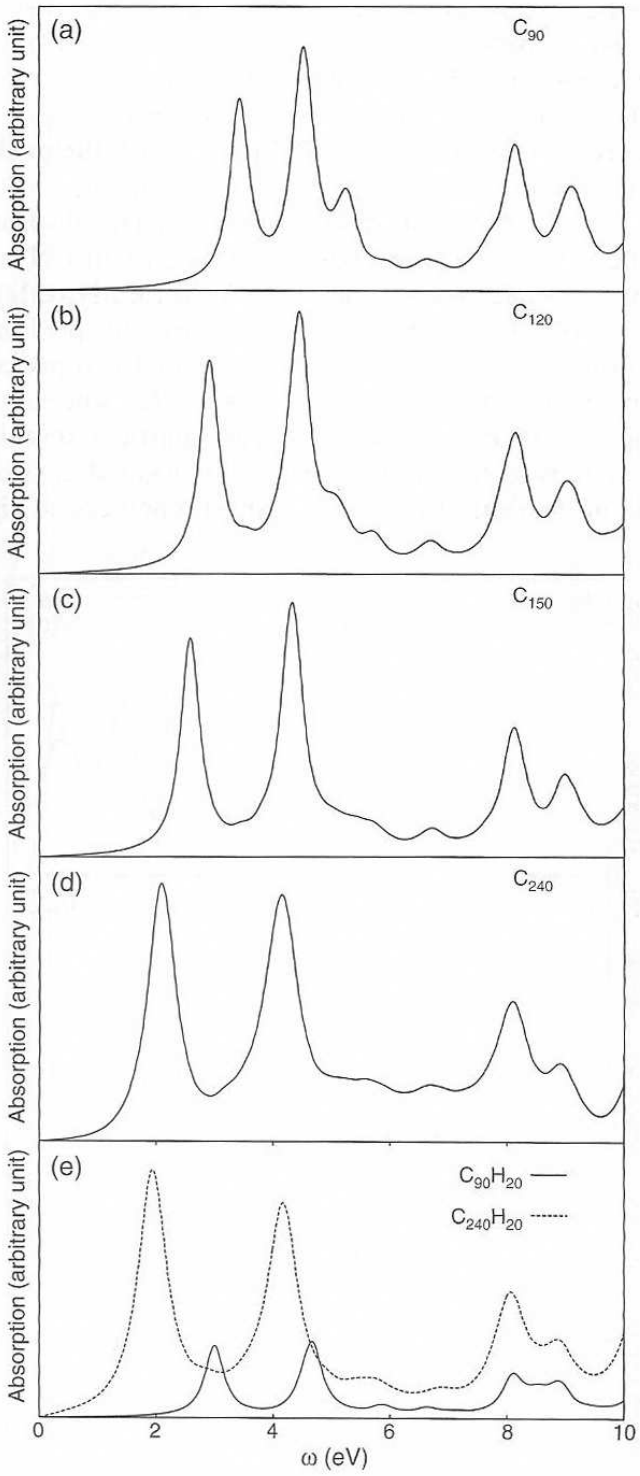

Figure 10. Absorption spectra of open-ended and capped (5, 5) armchair tubes calculated by full TDHF and LDM method. (a), (b), (c), and (d) are the absorption spectra of the capped (5, 5) tube. (e) Absorption spectra of open-ended (5, 5) tubes. The solid line is for $C_{10j}H_{20}$, $j = 9$, and the dashed line is for $j = 24$. (a), (b), (c), and (e) (solid line) are calculated with $\gamma = 0.2$ eV, whereas $\gamma = 0.3$ eV is employed in (d) and (e) (dashed line). All the geometries are optimized. Reprinted with permission from [65], W. Z. Liang et al., *J. Am. Chem. Soc.* 122, 11129 (2000). © 2000, American Chemical Society.

influence diminishes as the size increases. Absorption spectra of several SWNTs with different end groups have been measured, and little variance of the spectra has been observed [87]. This is consistent with our finding that the end groups of long SWNTs have little effect on their absorption spectra. The absorption spectra of (5, 5) CNTs (see Fig. 10) are similar to those of capped (9, 0) CNTs. This is because that both tubes have similar radii [3.5 Å for (9, 0) and 3.4 Å for (5, 5)]. The tight-binding calculations have predicted the same electronic and optical behavior for (5, 5) and (9, 0) tubes [21]. The optical absorption spectra of capped and open-ended (5, 5) look similar. For instance, a mere small red-shift is observed

for the open-ended (5, 5) tube $C_{90}H_{20}$ (solid line in Fig. 10e), as compared to capped C_{90+60} tube (Fig. 10c) of the same cylindrical length.

Computed optical absorption spectra of two SWNTs, (9, 0) (C_{294}) and (5, 5) (C_{290}), are shown in Fig. 11. Both SWNTs are capped by a bisected C_{60} molecule at their equators. Geometries are optimized by PM3, and the LDM-PM3 method is employed for the absorption spectra calculation. Solid lines are for (9, 0) and dashed lines are for (5, 5). In Fig. 11a, the external field **E** is along the tube axis, whereas **E** $\perp$ **T** in Fig. 11b. The diameters of (9, 0) and (5, 5) are 6.9 and 7.1 Å, respectively. In other words, (9, 0) and (5, 5) are of the similar diameters. Clearly, their absorption spectra are quite similar as well. This supports our conclusion that the chirality of a larger-diameter SWNT has little effect on its optical absorption spectrum [65].

The energy of the first major peak (or optical gap) of capped (9, 0) and (5, 5) CNTs versus $1/N$ is plotted in Fig. 12, where N is the number of carbon atoms. The two dashed lines are the linear fits and are almost identical. The optical gaps approach to $E_g = 1.23$ eV as the sizes of both tubes approach infinity. Because the radii of two CNTs are similar, the resulting optical gaps for two infinite long tubes have the same values up the second decimal digits. It may be generalized that the optical gaps for infinite long tubes are finite and their values depend mainly on the tube radii. The optical absorption spectra of finite-size capped (9, 0) and (5, 5) CNTs have been calculated by the tight-binding model with only π orbitals of carbon atoms considered. The tight-binding optical gaps for a (9, 0) tube with $N = 420$ and a (5, 5) tube with $N = 250$ are 1.2 and 1.25 eV, respectively [88, 89]. These are comparable to our extrapolated optical gaps for infinitly long CNTs. The optical signal at ~1.2 eV has been observed in the optical conductivity and absorption measurement of SWNTs [29, 90]. In addition, a gap of 1.2 eV has been found in the calculated DOS spectrum for (9, 0) by the tight-binding method [21].

Absorption spectra of capped (5, 0) tubes with $N = 150$ and 250 and of capped (6, 0) tubes with $N = 156$ and 252 are shown in Fig. 13. The absorption spectra of (5, 0) with $N = 150$ and (6, 0) with $N = 156$ are calculated by the full TDHF method with a dephasing coefficient $\gamma = 0.2$ eV. The absorption spectra of two other tubes are calculated by the LDM method with $\gamma = 0.3$ eV and a cutoff distance $l_0 = l_1 = 29$ Å. As expected, the red-shifts occur when the system sizes increase. The optical gap of infinite (5, 0) tube approaches ~1.0 eV, as shown in the inset of Fig. 13(a). A much weak peak appears at $\omega \sim 1.4$ eV for

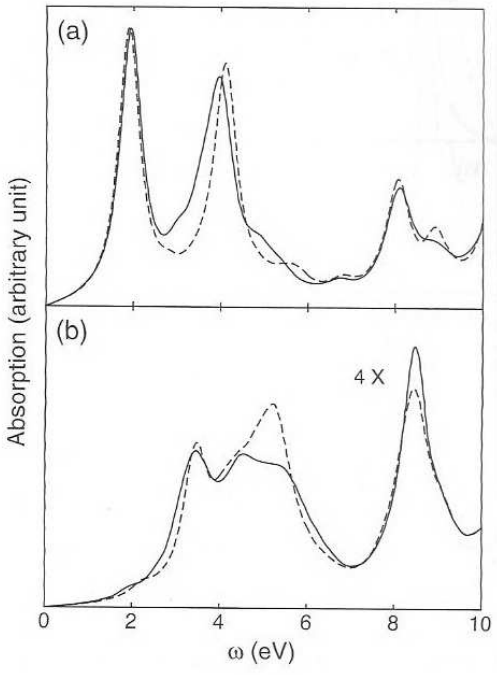

Figure 11. Calculated absorption spectra of capped (9, 0) C_{294} (solid line) and (5, 5) C_{290} (dashed line) SWNTs. The external field **E** is (a) along tube axis and (b) **E** $\perp$ **T**. The absorption spectra in (b) are magnified four times. The dephasing parameter $\gamma = 0.3$ eV. Reprinted with permission from [66], W. Z. Liang et al., *J. Am. Chem. Soc.* 123, 9830 (2001). © 2001, American Chemical Society.

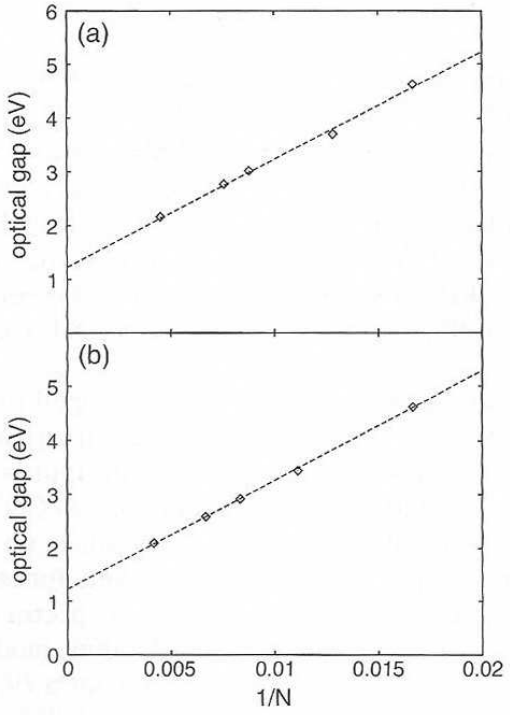

Figure 12. Optical gap via $1/N$ for capped $(9, 0)$ and $(5, 5)$ tubes. (a) $(9, 0)$ tube, (b) $(5, 5)$ tube. Reprinted with permission from [65], W. Z. Liang et al., *J. Am. Chem. Soc.* 122, 11129 (2000). © 2000, American Chemical Society.

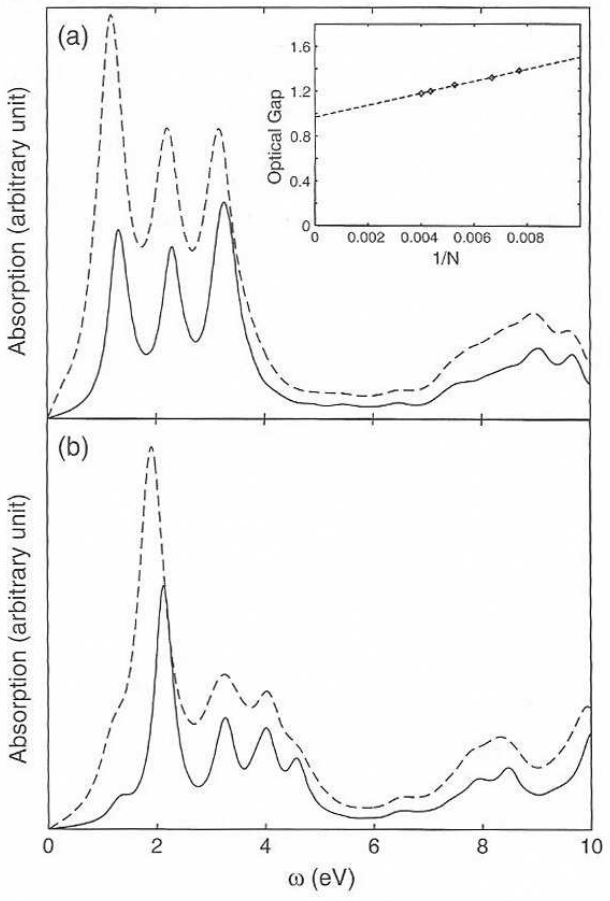

Figure 13. Absorption spectra of capped $(5, 0)$ and $(6, 0)$ tubes. (a) The absorption spectra of $(5, 0)$ C_{150} (the solid line) and C_{250} (dashed line) calculated by full TDHF and LDM with dephasing $\gamma = 0.2$ and $\gamma = 0.3$ eV, respectively. The inset shows the optical gap versus $1/N$ for the $(5, 0)$ tube. (b) The absorption spectra of the capped $(6, 0)$ tube. The solid line for C_{156} is calculated by full TDHF with $\gamma = 0.2$ eV. The dashed line for C_{252} is calculated by LDM with dephasing $\gamma = 0.3$ eV. All the geometries are optimized. Reprinted with permission from [65], W. Z. Liang et al., *J. Am. Chem. Soc.* 122, 11129 (2000). © 2000, American Chemical Society.

the $(6, 0)$ tube. This is because the optimized geometry for the $(6, 0)$ tube has C_{2v} point group symmetry which is different from the C_{3h} point group of the $(9, 0)$ tube. Tubes like $(9, 0)$ and $(5, 5)$ have the first major absorption peak located at a larger transition energy, and $(5, 0)$ tubes of the same length possess relatively small optical gaps. This indicates that geometry plays a fundamental role in determining the optical behavior of CNTs.

A broad group of peaks located at $6.0 \sim 7.0$ eV is observed in the absorption spectra of capped $(5, 0)$, $(6, 0)$, $(9, 0)$, and $(5, 5)$ tubes. These peaks shift little as the tube lengths increase and are identified mainly as $\pi - \pi^*$ transitions by the low-energy EELS experiments [29] and calculations [91]. The relative oscillator strength decreases with the reducing tube radius. This is caused by larger $\pi - \sigma$ hybridization in smaller-radius tubes. The larger the curvature, the more the π and σ hybridization.

Figure 14 shows the optical absorption spectra of an open-ended armchair tube ($C_{4mj}H_{2m}$), with $j = 4$ and $m = 6$, 8, and 10. The ideal structures, which are rolled up from a single graphite sheet with all bond lengths set to 1.421 Å are adopted here. The absorption spectra red-shift as the tube radius increases, except that the first peak blue-shifts slightly. The blue-shift may come from the competition between the size effect and the π orbital overlapping. When the external electric field is applied perpendicular to the tube axis, red-shifts of lowest peaks are observed when the radii of tubes increase. This is consistent with the expectation that the lowest peak red-shifts as the radius increases (see Fig. 15, in which the optical gaps versus $1/r$ is plotted with r being the radius of the tube). A linear relationship between the gap and $1/r$ is observed, and a gap of 0.7 eV is determined as $r \to \infty$. It was also found that the absorption threshold is significantly higher for the external field polarized along

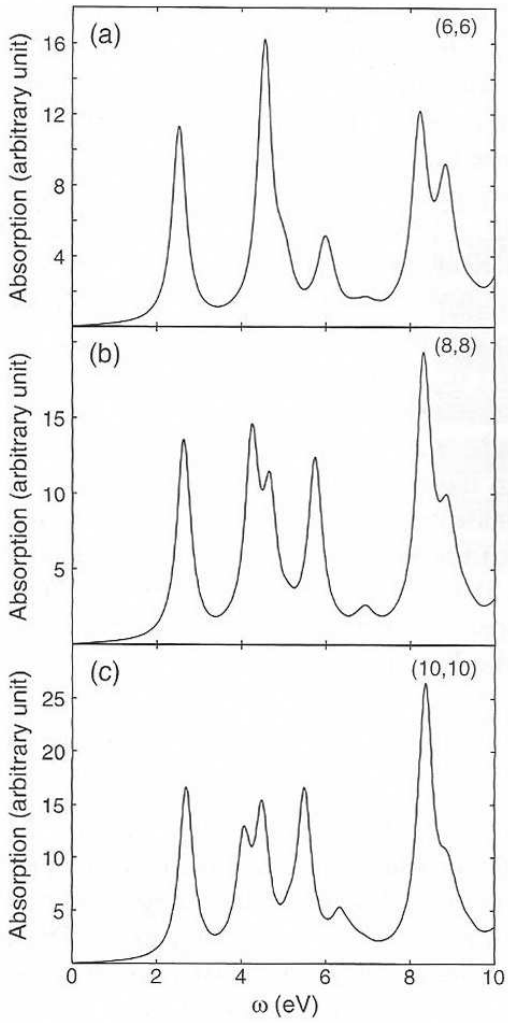

Figure 14. Absorption spectra of (m, m) armchair tube with $m = 6, 8, 10$ and dephasing $\gamma = 0.2$ eV. The ideal structure is employed. (a) $(6, 6)$ $C_{12j}H_{24}$. (b) $(8, 8)$ $C_{16j}H_{32}$. (c) The absorption spectra of $(10, 10)$ $C_{20j}H_{40}$, with $j = 8$. Reprinted with permission from [65], W. Z. Liang et al., *J. Am. Chem. Soc.* 122, 11129 (2000). © 2000. American Chemical Society.

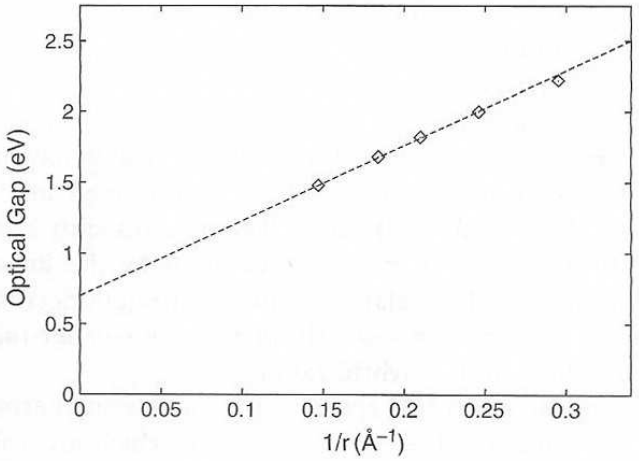

Figure 15. The optical gap via $1/r$ when the external field is applied perpendicular to the tube axis. Reprinted with permission from [65], W. Z. Liang et al., *J. Am. Chem. Soc.* 122, 11129 (2000). © 2000, American Chemical Society.

the tube axis than perpendicular to the tube axis. The absorption spectra of (6, 6), (8, 8), and (10, 10) are very different from that of (5, 5) (solid line in Fig. 10e). This is because different bond lengths are used here. Thus, it is determined that the nature of excitations is sensitive to the bond lengths. The density matrices in molecular orbital (MO) representation reveal that the first peak in armchair tubes come mainly from the HOMO $\rightarrow$ LUMO + 1 and HOMO $-$ 1 $\rightarrow$ LUMO transitions. The HOMO $\rightarrow$ LUMO transition is forbidden. The other peaks red-shift with the increasing tube radius. The relative oscillator strength of these peaks that center at relatively high energies (from 4.3 to 8.2 eV) increase with the increasing radius. These peaks correspond to $\pi - \pi^*$ and small-fraction $\pi - \sigma^*$ transitions.

We proceed to discuss the single-electron density matrices of the dipole-induced excitations. To understand the nature of the electronic excitations, the induced density matrices $\delta\rho^{(1)}(\omega)$ of $C_{72}H_9(OH)_9$ are examined at 0.61, 2.67, and 5.01 eV; C_{72+60} at 2.77, 6.72, and 8.14 eV; and $C_{80}H_{20}$ at 2.89, 4.79, and 8.04 eV. $C_{72}H_9(OH)_9$ and C_{72+60} are open-ended and capped (9, 0) tubes, respectively, and $C_{80}H_{20}$ is an open-ended (5, 5) tube. The results are shown in the Figs. 16, 17, and 18. The atomic orbital (AO) representation is employed. The atomic indices are assigned increasingly from one end of the tube to the other, and the orbital indices are arranged in the order of $2s, 2p_x, 2p_y$, and $2p_z$. The absolute values of density matrix elements are shown in the contour plots. Logarithmic scale is employed. The scales employed for ground- and excited-state density matrices are shown in Fig. 16e and Fig. 16f, respectively. From the contour plots in Figs. 16a, 17a, and 18a, it is observed that the ground-state density matrices of the three systems are almost diagonal. However, the electron coherence between the two ends is stronger in the opened-end (9, 0) tube than in the capped (9, 0) and (5, 5) CNTs. The strong electron coherence between the two open ends of (9, 0) has a significant influence on the optical properties. The excited-state density matrices are obtained by the Fourier transformation

$$\delta\rho(\omega) = \int dt\, e^{i\omega t}\delta\rho(t) \tag{35}$$

In the actual TDHF calculation, dephasing γ is added to calculate the time evolution of $\delta\rho(t)$. The term $\delta\rho(\omega)$ contains not only the effect of the mode at ω but also the effect of other modes. When γ is much less than the energy differences of different excitations, the mixing of excitations in $\delta\rho(\omega)$ ($\omega \sim \Omega_\nu$) is negligible. Therefore, $\mathrm{Im}[\delta\rho(\Omega_\nu)]$ is a very good approximation of the reduced-density matrix for the excitation at Ω_ν. The density matrices shown take the form $\{\mathrm{Im}[\delta\rho(\omega)] + \mathrm{Im}[\delta\rho^T(\omega)]\}/(i\sqrt{2})$, where $\delta\rho^T(\omega)$ is the transpose of $\delta\rho(\omega)$. Three excited-state density matrices of an open-ended (9, 0) tube are shown in Fig. 16b–d. The first excitation at $\omega = 0.61$ eV in $C_{72}H_9(OH)_9$ includes mostly the π electron–hole pairs from the two ends. This peak disappears in the absorption spectra of capped (9, 0) tubes. The contribution from the electron–hole pairs among the π orbitals

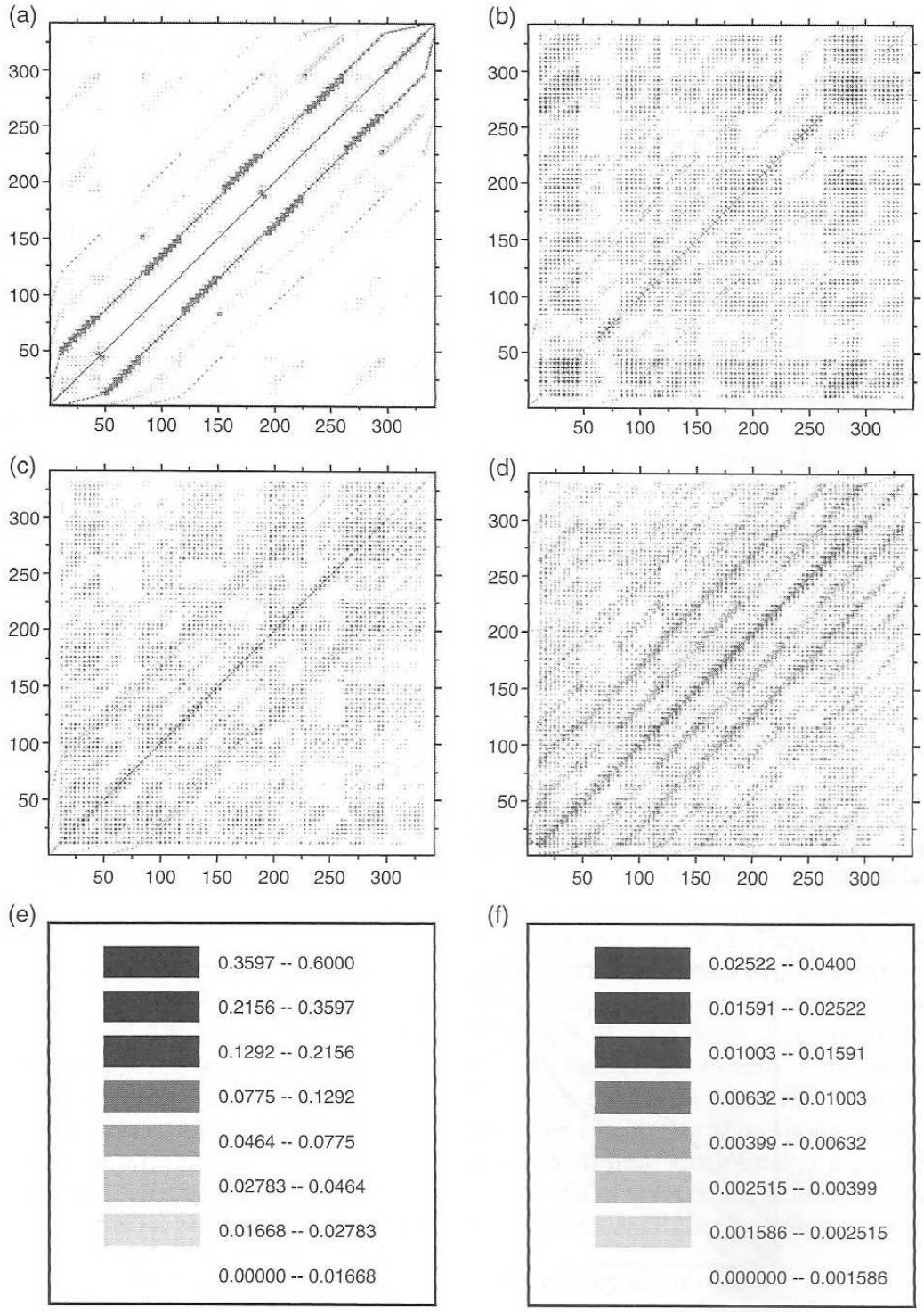

Figure 16. Density matrices of ground states and various excited states for an open-ended (9, 0) $C_{72}H_9(OH)_9$ tube in AO representation by full TDHF with $\gamma = 0.1$ eV. Matrix elements are shown on a gray logarithmic scale. (a) The ground state; (b) $\omega = 0.61$ eV; (c) $\omega = 2.67$ eV; (d) $\omega = 5.01$ eV; (e) scale of all the ground-state density matrices; (f) scale of all the excited state density matrices. Reprinted with permission from [65], W. Z. Liang et al., *J. Am. Chem. Soc.* 122, 11129 (2000). © 2000, American Chemical Society.

located in the middle of tube increases for the excitation at $\omega = 2.67$ eV. The excitation at 5.01 eV in $C_{72}H_9(OH)_9$ contains π as well as σ orbital contributions. In general, a contribution that comes from the electron–hole pairs in the middle increases rapidly as energy increases. As expected, the oscillator strengths of these excitations increase and their energies red-shift with increasing sizes [49].

Figure 17b–d depict the excited-state density matrices of capped (9, 0) tube C_{72+60} at energies 2.77, 6.72, and 8.14 eV, whereas Fig. 18b–d show the excited-state density matrices of an open-ended (5, 5) tube at energies 2.89, 4.79, and 8.04 eV, respectively. The contributions from two ends are much weaker than those in $C_{72}H_9(OH)_9$; that is, the electron coherence

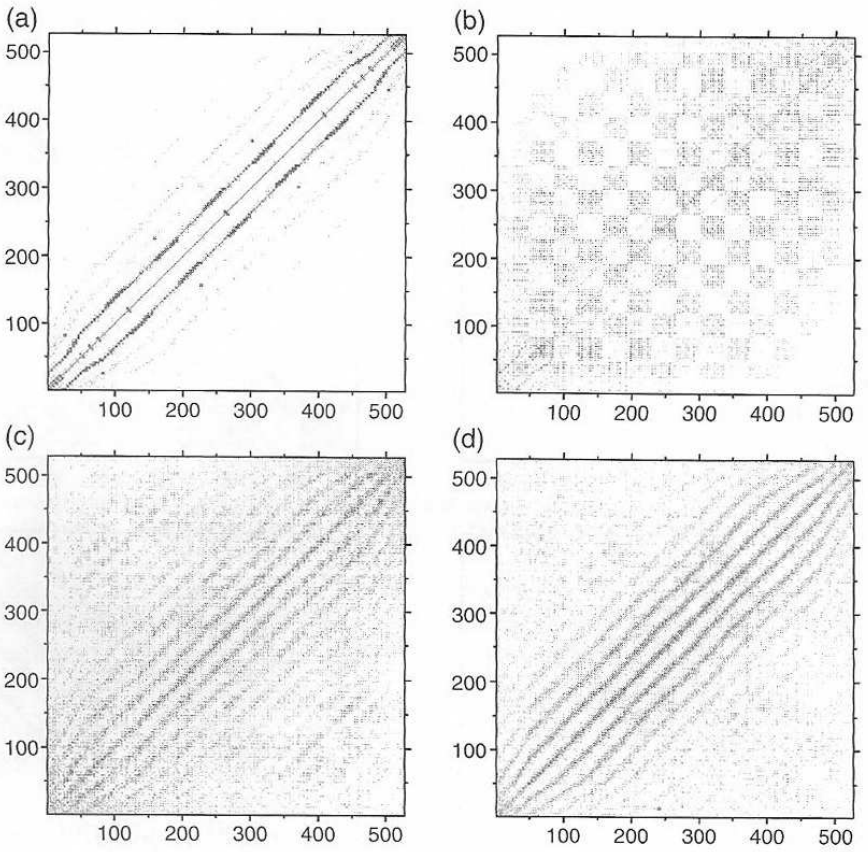

Figure 17. Density matrices of ground states and various excited states for capped $(9, 0)$ tube C_{132} in AO representation by full TDHF with $\gamma = 0.1$ eV. (a) The ground state; (b) $\omega = 2.77$ eV; (c) $\omega = 6.72$ eV; (d) $\omega = 8.14$ eV. Reprinted with permission from [65], W. Z. Liang et al., *J. Am. Chem. Soc.* 122, 11129 (2000), © 2000. American Chemical Society.

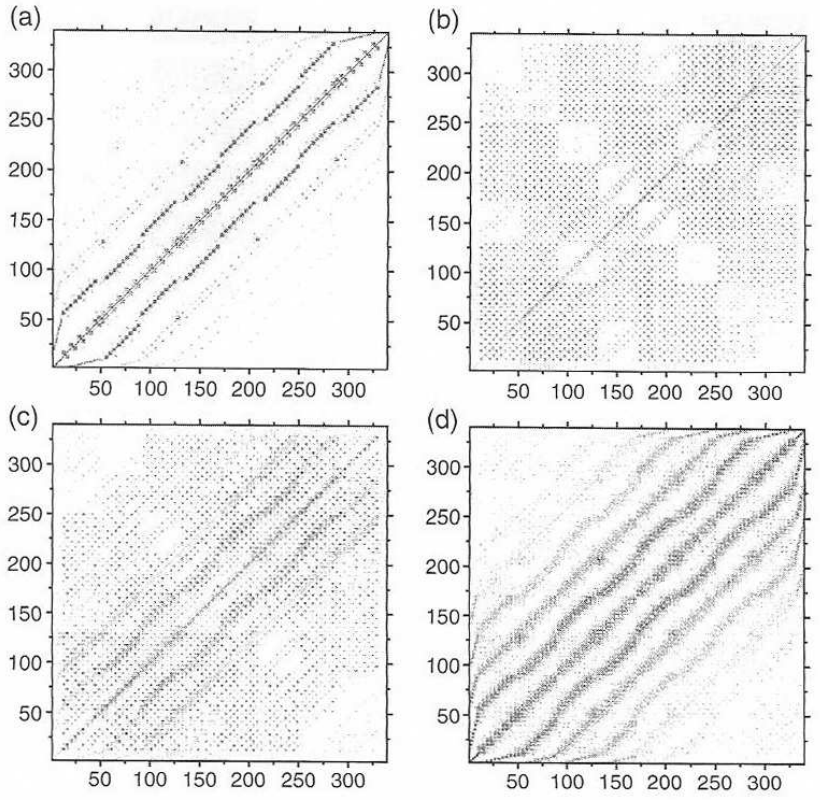

Figure 18. Density matrices of ground states and various excited states for open-ended $(5, 5)$ tube $C_{80}H_{20}$ in AO representation by full TDHF with $\gamma = 0.1$ eV. (a) The ground state; (b) $\omega = 2.89$ eV; (c) $\omega = 4.79$ eV; (d) $\omega = 8.04$ eV. Reprinted with permission from [65], W. Z. Liang et al., *J. Am. Chem. Soc.* 122, 11129 (2000). © 2000, American Chemical Society.

between two ends is weak. The main contributions are from the middle of the tubes. This is the reason why the absorption spectra are rather similar for (5, 5) and capped (9, 0) tubes. The peaks centered at the low-energy of 2.77 eV in Fig. 17b and at 2.89 and 4.79 eV in Fig. 18b and 18c result mostly from π electron–hole pairs. The first peak in both systems comes mostly from HOMO $\rightarrow$ LUMO + 1 and HOMO − 1 $\rightarrow$ LUMO transitions. Transitions HOMO $\rightarrow$ LUMO + 2 and HOMO − 2 $\rightarrow$ LUMO also contribute significantly to the first peak ($\omega = 2.77$ eV) of the capped (9, 0) tube. Other transitions between the HOMO − m and LUMO + n also effect the first peak of the (9, 0) and (5, 5) tubes. The white squares of the "chess board" pattern in Fig. 17b correspond to the electron coherence between two orbitals that belong to two atoms located, respectively, at the nth ring and $n \pm j$th rings, where j is a positive odd number. The antidiagonal part is nearly zero in Figs. 17b and 18b. The white square in the antidiagonal part corresponds to the elements between the two orbitals that belong to the two atoms located, respectively, at two mirror rings, which are symmetric with respect to a center plane equally dividing the nanotube. Their values are almost zero except for the pairs of π orbitals, which belong to two mirror symmetric atoms. The σ electrons have larger contribution in the high- energy range; for instance, the peaks at 6.72 and 8.14 eV (Fig. 17c and 17d) in capped (9, 0) tube and the peak at 8.04 eV (Fig. 18d) in the (5, 5) tube. These peaks originate from the main $\pi - \pi^*$ transition as well as the partial $\pi - \sigma^*$ transition, which is revealed by the corresponding density matrices in MO representation. These excitations have been observed by low-energy EELS experiment [92]. The electron coherence among $\pi - \pi^*$ has larger spatial extents than that among $\pi - \sigma^*$, $\sigma - \pi^*$, and $\sigma - \sigma^*$ (see Fig. 17c, 17d). Examining the excited-state density matrices of these three systems reveals that π orbitals are mainly responsible for electron excitations, with $\omega < 8.0$ eV, while σ electrons are responsible for higher-energy electron excitations. The patterns of the reduced-density matrix contour plots reflect the structure features of CNTs. For instance, the stripes in Figs. 16a, 16d, 17a, 17c, 17d, 18a, 18c, and 18d are the manifestation of the underlying ring structure of CNTs. The "chessboard" pattern in Fig. 17b reflects large electron coherence within the same ring or between adjacent rings (the dark squares), and diminishing electron coherence between adjacent or next-nearest rings.

The STM may probe directly one electron orbital density or DOS. Figure 19 shows the DOS of several CNTs; $C_{300}H_{20}$, $C_{316}H_{20}$, and $C_{320}H_{20}$. The chiralities of above three CNTs are (6, 4), (7, 3), and (5, 5), respectively. The ideal structures are employed. Their radii are 3.415, 3.482, and 3.393 Å, and the lengths are 35.3, 34.91, and 38.14 Å, respectively. The Fermi energy level is between the HOMO and LUMO and is set to zero. According to the tight-binding model, a CNT with a chirality (m, n) is a conductor when $m - n \bmod 3 = 0$. A CNT with other chiralities is a semiconductor. Our calculation shows that the HOMO-LUMO gap for a (5, 5) is 2.8 eV, whereas (7, 3) and (6, 4) have much smaller gaps, although three radii and lengths are of the similar values. The DOS spectra are determined by their chiralities of CNTs. Further, we find that the HOMO-LUMO energy difference decreases

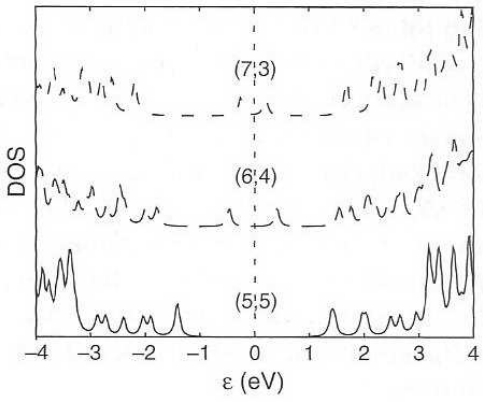

Figure 19. DOS of HF molecular orbitals of (5, 5) $C_{320}H_{20}$, (7, 3) $C_{312}H_{20}$, and (6, 4) $C_{300}H_{20}$ by the PM3 Hamiltonian. The Fermi level is set to $\epsilon = 0.0$ eV. The energy resolution $\eta = 0.05$ eV is employed. Reprinted with permission from [65], W. Z. Liang et al., *J. Am. Chem. Soc.* 122, 11129 (2000) © 2000, American Chemical Society.

overall as the nanotube length increases and the energy gap in the DOS spectrum may be different from the HOMO-LUMO energy difference. This energy gap and DOS spectrum saturate when the length is long enough. Our calculated HOMO-LUMO energy gap of (5, 5) tubes is larger than that of the tight-binding calculation for CNTs of the same length because the HOMO-LUMO energy gaps predicted by tight-binding calculation saturate more rapidly than those by *ab initio* HF or semiempirical methods [93]. It is worthy pointing out that the DOS of (5, 5) calculated by the tight-binding model has a similar appearance to our result, and a gap of 2.0 eV exists. Our calculated DOS is not symmetric with respect to the Fermi level, which is consistent with the experiment [94] but differs from the tight-binding results [95–97]. The difference stems from $\pi - \sigma$ hybridization [98].

The absorption spectra of a series of CNTs with different sizes, chiralities, ends, and bond lengths are calculated by the LDM method with the PM3 Hamiltonian. The dipole-induced excitations may be categorized into end modes (low energy) and tube modes (high energy). These modes have been characterized by examining their reduced single-electron density matrices. It has been found that their optical properties are very much affected by the tube length, radius, end group, and chirality, as well as the bond length. The density matrices of various excitations exhibit interesting features that relate to the structural features of CNTs. The main results are summarized as follows.

The low-energy dipole-induced excitations appearing in the absorption spectra in Fig. 8 are the end modes; that is, the electron–hole pairs that reside mostly at the two ends of tube. These excitations come mainly from $\pi - \pi^*$ transitions. The corresponding absorption peaks have been observed only for short, open-ended, zigzag CNTs in our calculation. The excitation energy and oscillator strength depend sensitively on the tube length, end groups and chiralities. As the length increases, the low-energy ($\omega \leq 1.0$ eV) absorption peaks red-shift, and their oscillator strengths decrease. When the end groups are altered, the profile of low-energy-absorption spectra changes drastically for short CNTs. Their sensitivities to the end groups may be used to design new SWNT-based materials. It is interesting to note that the capped zigzag CNTs and armchair tubes do not have such low-energy absorption peaks. We emphasize that the absorption spectra of long SWNTs are affected little by the caps or end groups. This has been confirmed experimentally [87].

For $\omega \geq 2.0$ eV in Fig. 8, the dipole-induced excitations are regarded as the tube modes; that is, the electron–hole pairs residing in the middle of the tube. The energies and oscillator strengths of these tube modes may depend on the tube lengths, radii, and bond-length alternations. However, they are not sensitive to the chirality and end groups. It is emphasized that the absorption spectra for capped (9, 0), capped (5, 5), and open-ended (5, 5) tubes of the same length are strikingly similar.

The tube modes may be divided further into two groups of excitations: $2.0 \leq \omega \leq 6.0$ and $\omega \geq 6.0$ eV. For the excitations whose energies ω are between 2.0 and 6.0 eV, the electron–hole pairs arise from $\pi - \pi^*$ transitions. These excitations are sensitive to the tube length. As the tube length increases, the corresponding absorption peaks red-shift (see Figs. 8–13). The absorption spectrum saturates when the tube length reaches a few nanometers. The calculated optical gaps are consistent to the energy gaps measured by STM experiment [29]. When the radii increase, most absorption peaks in the range ($2.0 \leq \omega \leq 6.0$ eV) red-shift except the first absorption peaks of armchair CNTs (see Fig. 14), which blue-shift slightly when the external field is polarized along the tube. This may be explained by the competing effects of the hopping matrix elements of π electrons and the tube radii.

For the dipole-induced excitations with $\omega \geq 6.0$ eV, their energies and oscillator strengths are not sensitive to the length, chiralities, and ends, but their oscillator strengths are sensitive to the tube radii and bond-length alternation. The broad peaks at $6.0 \sim 7.0$ and $8.0 \sim 9.0$ eV are mostly from the $\pi - \pi^*$ transitions, but a small fraction of $\pi - \sigma^*$, $\sigma - \pi^*$, and $\sigma - \sigma^*$ transitions also contribute to these peaks.

For the open-ended tubes containing a few hundreds of atoms, it is observed that the HOMO–LUMO gap for armchair CNTs is quite large [$\sim$2.0 eV for (5, 5)]. This confirms results from earlier *ab initio* Hartree–Fock and semiempirical calculations [93]. It was postulated that this larger HOMO–LUMO gap is a result of the finite size effect. As the tube

length increases to infinity, the gap may vanish. Our calculation shows evidence for such a postulation.

Finally, the optical gaps of CNTs are finite and approach nonzero values as the tube lengths become infinity. It is illustrated that the optical gaps depend linearly on $1/N$. The inverse dependence of the optical gap on diameter has been investigated in armchair tube (m, m). It is found that the optical gaps depend inversely on the diameter of the tubes.

In summary, the dipole-induced excitations may be categorized into the end modes and tube modes. The end modes are sensitive to the tube length, chirality, and radius in addition to the bond length. When the tube length becomes long enough or the ends are closed with carbon cages, the corresponding low-energy absorption peaks disappear. The tube modes are of higher energies and are less sensitive to the tube length and chirality. The dipole-induced transitions below 8.0 eV are composed mainly of $\pi - \pi^*$ transitions. Furthermore, it has been found that the optical gap scales linearly with $1/N$ and is finite when the number of carbon atoms N approaches infinity. Although the precise values of excitation energies and oscillator strengths may depend on detailed structures of CNTs, the above qualitative conclusion on the composition and categorization of CNTs' optical excitations remains valid.

3.3. Polarization-Dependent Optical Absorption Spectra of 4-Å Single-Walled Carbon Nanotubes

The narrowest possible nanotube has a diameter of 4 Å, the size at which a SWNT remains energetically stable. Some of the smallest CNTs are first found capped inside an 18-shell nanotube [79]. Lately, 4-Å SWNTs have been fabricated inside inert AFI zeolite channels [32, 33]. Chen et al. have examined the optical properties of 4-Å SWNTs using the LDM method [65].

The two ends of the SWNTs are terminated with hydrogen atoms in the calculations. The ideal structures are employed; that is, the SWNTs are constructed by rolling graphite segments along the tube axis with the C–C bond length set to 1.42 Å, except that the structures of (4, 2) SWNTs are optimized by the PM3 calculations. In a neutral (5, 0) CNT electrons cannot fill the closed-shell structure. The unpaired electrons result in a net dipole moment that prevents the converge of the self-consistent field (SCF) calculation [99]. Four extra electrons are added to the (5, 0) CNT, on which the self-consistent computation converges and a set of MOs are obtained. It is expected that the extra four electrons have little effect on the optical response when the number of carbon atom reaches 200 or more. Figures 20, 21, and 22 show calculated absorption spectra of (4, 2), (3, 3), and (5, 0) SWNTs. Each unit cell of the (4, 2), (3, 3), and (5, 0) CNTs has 56, 12, and 20 carbon atoms, respectively. All solid lines are the absorption spectra corresponding to $\mathbf{E} \parallel \mathbf{T}$, and the dashed lines correspond to $\mathbf{E} \perp \mathbf{T}$. The calculated absorption spectra of (4, 2), (5, 0), and (3, 3) CNTs are quite different despite the fact that their diameters are almost the same. This differs from our previous results from larger-diameter CNTs, which showed that the absorption spectra are insensitive to the chiralities of CNTs when the tube lengths are long enough. In the case in which $\mathbf{E} \parallel \mathbf{T}$, the optical spectra of the three SWNTs depend very much on the tube lengths. As the number of carbon atoms increases, the absorption spectra of the open-ended chiral (4, 2) tubes change drastically, especially when the tube lengths are relatively short. The overall spectra red-shift and the relative amplitude in the low-energy range ($\omega < 1.0$ eV) reduce as the number of carbon atom N increases. When the (4, 2) SWNTs have 200 or more carbon atoms, these peaks disappear when compared to the others (see Fig. 20). The open-ended (3, 3) and (5, 0) SWNTs have a different response to the external field as compared to the (4, 2) SWNTs. In the low-energy range ($\omega < 1$ eV), no peaks are found even for very short tubes (see Figs. 21 and 22). The two ends play an important role in the optical response for some short tubes; for instance, the (4, 2) CNTs. Their influence recedes as the length increases. The optical behaviors of the long tubes are affected little by the two ends, which is consistent with experimental observations [87, 90].

Two absorption peaks are found at 1.60 and 2.9 eV for (4, 2) $C_{332}H_{12}$, and three peaks are found at 1.16, 1.66, and 2.60 eV for (5, 0) $C_{300}H_{10}$. The (3, 3) SWNT has one distinctive

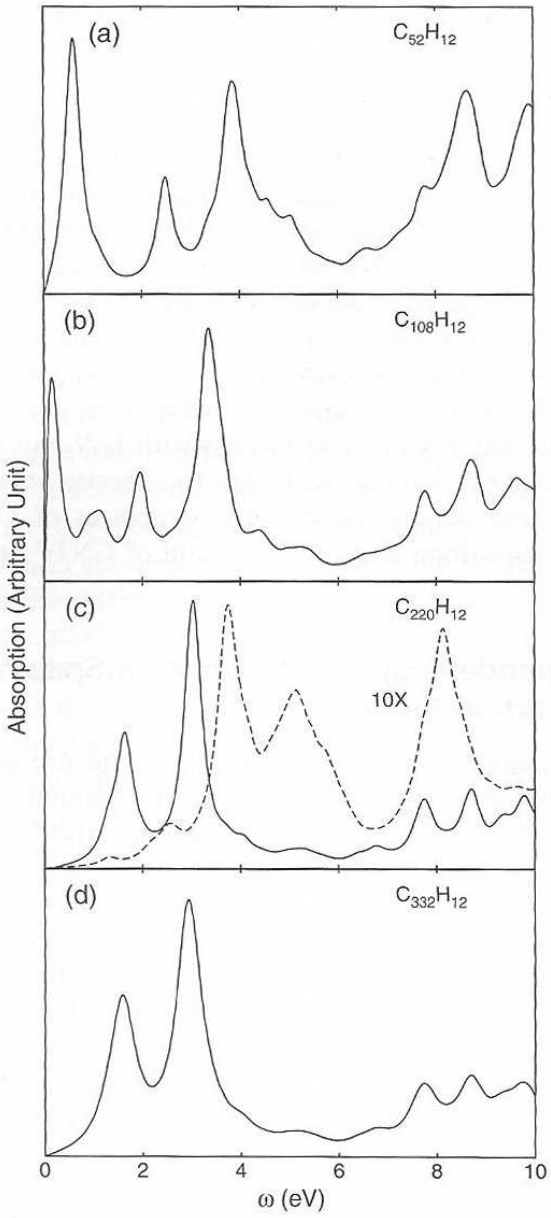

Figure 20. Calculated absorption spectra of (4, 2) SWNTs with dephasing parameter $\gamma = 0.2$ eV (a–c) and $\gamma = 0.3$ eV (d). The external field **E** is along tube axis except the dashed line in part (c) which is the result for $\mathbf{E} \perp \mathbf{T}$. The dashed lines are magnified 10 times. Reprinted with permission from [66], W. Z. Liang et al., *J. Am. Chem. Soc.* 123, 9830 (2001). © 2001, American Chemical Society.

strong absorption peak in the low-energy range for $N > 200$. It red-shifts when the tube length increases and saturates at 0.61 eV as $N \to \infty$ (see Fig. 23b). Similar red-shifts of absorption spectra are found for (4, 2) and (5, 0) SWNTs. These red-shifts are caused by the collective character of the excitation in terms of the single electron–hole excitation picture [59]. Because π electrons delocalize more than σ electrons, the red-shifts are prominent for $\omega < 4$ eV because the corresponding excitations are mainly $\pi - \pi^*$ transition. Note that the spectral profiles do not vary much after N reaches 200 or more. Therefore, $C_{332}H_{12}$, $C_{420}H_{12}$, and $C_{300}H_{10}$ are used to simulate, respectively, the infinite long (4, 2), (3, 3), and (5, 0) SWNTs. Given the fact that the absorption spectra are very different for (4, 2), (3, 3), and (5, 0), it is concluded that for small-diameter SWNTs, the optical response depends on the chirality of the tube, in addition to the diameter and the tube length. Therefore, the observed absorption spectra may be used to determine the structures of 4-Å SWNTs.

To investigate the anisotropy characters of (3, 3), (5, 0), and (4, 2) SWNTs, their absorption spectra are calculated by aligning the external field **E** perpendicular to the tube axis ($\mathbf{E} \perp \mathbf{T}$). The resulting absorption spectra are shown as dashed lines in Figs. 20c, 21a, 21b, 22a, and 22c. Strong anisotropy is observed for all three SWNTs. The absorption intensities

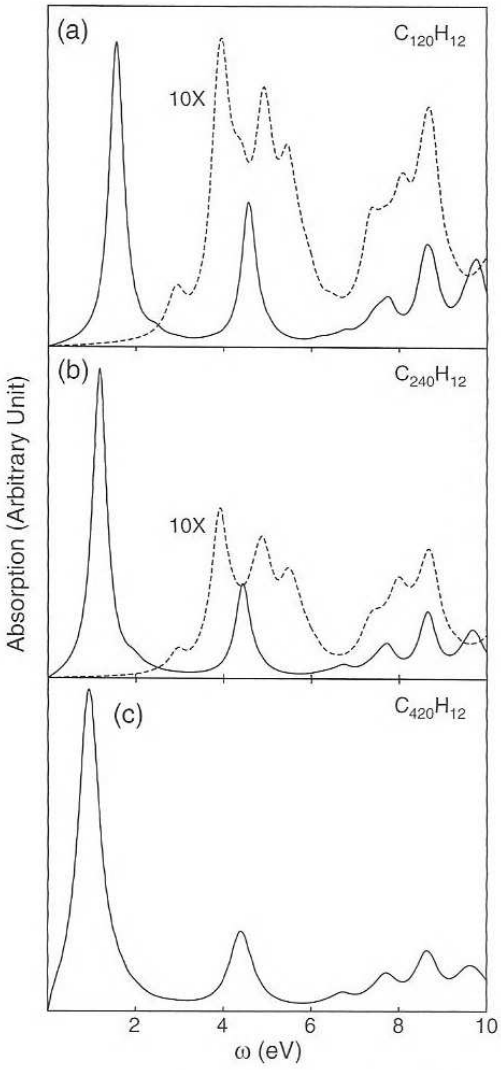

Figure 21. Calculated absorption spectra of (3, 3) SWNTs with dephasing parameter $\gamma = 0.2$ eV (a, b) and $\gamma = 0.3$ eV (c). The solids are the results for $\mathbf{E} \parallel \mathbf{T}$ and the dashed lines for $\mathbf{E} \perp \mathbf{T}$. The dashed lines are magnified 10 times. Reprinted with permission from [66], W. Z. Liang et al., *J. Am. Chem. Soc.* 123, 9830 (2001). © 2001, American Chemical Society.

are much weaker for $\mathbf{E} \perp \mathbf{T}$ as compared to for $\mathbf{E} \parallel \mathbf{T}$. The anisotropy increases as the tube length increases. This is consistent with the experimental observation [81] that the 4-Å SWNTs are opaque for $\mathbf{E} \parallel \mathbf{T}$ but almost transparent for $\mathbf{E} \perp \mathbf{T}$. The lowest-absorption peak red-shifts when the light polarization varies from the parallel direction of the tube to the perpendicular direction [81]. Our calculations show the same phenomenon for (4, 2) and (5, 0) but not for (3, 3). For (4, 2) $C_{220}H_{12}$ and (5, 0) $C_{300}H_{10}$, their respective optical gaps are 1.33 and 0.70 eV for $\mathbf{E} \perp \mathbf{T}$, and 1.64 and 1.16 eV for $\mathbf{E} \parallel \mathbf{T}$. For (3, 3) CNTs, the optical gap is larger for $\mathbf{E} \perp \mathbf{T}$ than for $\mathbf{E} \parallel \mathbf{T}$.

The optical gaps of the open-ended tubes (4, 2), (3, 3), and (5, 0) versus $1/N$ for $\mathbf{E} \parallel \mathbf{T}$ are plotted in Fig. 23a, 23b, and 23c, respectively. The dashed lines are the linear fits. Clearly the gaps depend linearly on $1/N$. The optical gaps of (4, 2), (3, 3), and (5, 0) are respectively 1.5, 0.61, and 0.90 eV as the tubes become infinitely long. In Ref. [65], similar findings have been reported; that is, it was found that the long (6, 0), (9, 0), (5, 5), (8, 8), and (10, 10) SWNTs have finite optical gaps.

The concept of the pyramidalization angle is developed to extend the definition of the π orbital to a nonplanar molecule [100]. To examine the effect of rehybridization of the σ and π electrons on the optical gap, the pyramidalization angle [100] of those carbon nanotubes has been calculated using the π orbital axis vector 1 (POAV1) analysis [100, 101]. The π orbital axis makes equal angles with all three σ bonds at the conjugated carbon atom in question. The angle between π orbital axis vector and the σ bond is 90 degrees for

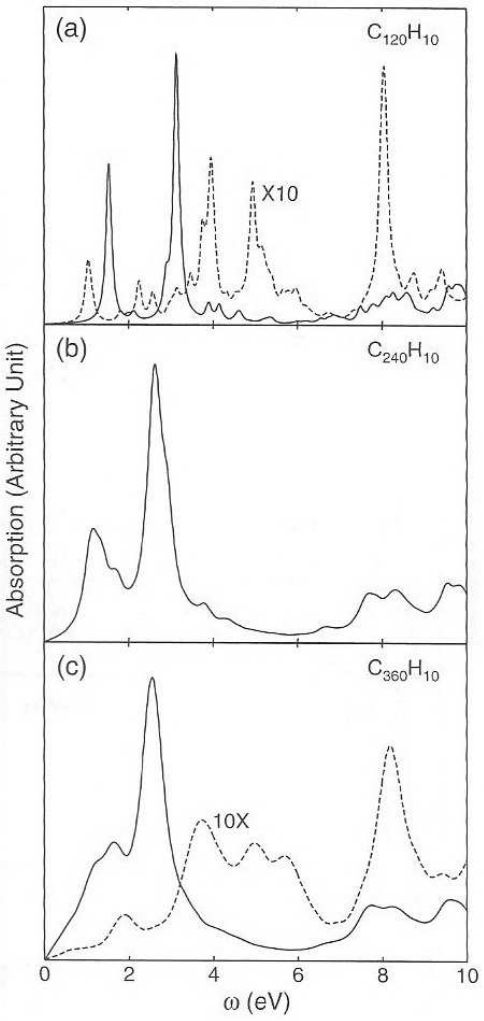

Figure 22. Calculated absorption spectra of zigzag (5, 0) SWNTs with dephasing parameter $\gamma = 0.08$ eV (a) and $\gamma = 0.2$ eV (b and c). The solids are the results for $\mathbf{E} \parallel \mathbf{T}$ and the dashed lines for $\mathbf{E} \perp \mathbf{T}$. The dashed lines are magnified 10 times. Reprinted with permission from [66], W. Z. Liang et al., *J. Am. Chem. Soc.* 123, 9830 (2001). © 2001, American Chemical Society.

planar molecules. The pyramidalization angle θ_P is then defined as the deviation of this angle from 90 degrees. The larger θ_P is, the larger the rehybridization of the σ and π electrons [100]. For (3, 3) and (5, 0), $\theta_P = 9.9$ and 10.0 degrees are obtained, respectively. For (4, 2) $C_{220}H_{12}$, θ_Ps are $9.6 \sim 9.7$ degrees, depending on the atoms. Because the θ_P values have no clear correlation with the optical gaps, it is conjectured that the differences in the optical spectra of (4, 2), (3, 3), and (5, 0) are caused mainly by the relative positions of the carbon atoms.

Armchair and zigzag SWNTs are highly symmetric. Depending on the way we terminate the open CNTs, (3, 3) and (5, 0) CNTs may have D_{3h} or D_{3d} and D_{5h} or D_{5d} symmetry, respectively [99]. When the lengths of the (3, 3) and (5, 0) SWNTs are large enough (>25 Å), the difference in optical response caused by different symmetries can be neglected [93, 99]. Chosen here to be examined are (3, 3) SWNTs with D_{3d} symmetry and (5, 0) with D_{5h}. For the dipole-allowed optical transition, the matrix element $\langle \Phi_i | \mathbf{r} \cdot \mathbf{E} | \Phi_f \rangle$ is nonzero, and $|\Phi_i\rangle$ ($|\Phi_f\rangle$) is the initial (final) electronic state. The variable D_{3d} has six irreducible representations: A_{1g}, A_{2g}, E_g, A_{1u}, A_{2u}, and E_u, and D_{5h} has eight irreducible representations: A_1', A_2', E_1', E_2', A_1'', A_2'', E_1'', and E_2'' [102]. For the electric field $\mathbf{E} \parallel \mathbf{T}$, the following transitions are allowed between the pairs of the molecular orbitals: for (3, 3) SWNTs, $A_{1g} \leftrightarrow A_{2u}$, $A_{2g} \leftrightarrow A_{1u}$, and $E_u \leftrightarrow E_g$; and for (5, 0) SWNTs, $E_1' \leftrightarrow E_1''$, $E_2' \leftrightarrow E_2''$, and $A_1' \leftrightarrow A_2''$. For the electric field $\mathbf{E} \perp \mathbf{T}$, the allowed transitions are, for (3, 3), $A_{1g} \leftrightarrow E_u$, $A_{2g} \leftrightarrow E_u$, $A_{1u} \leftrightarrow E_g$, $A_{2u} \leftrightarrow E_g$, and $E_u \leftrightarrow E_g$; and for (5, 0), $A_1' \leftrightarrow E_1'$, $A_1' \leftrightarrow E_2'$, $A_2' \leftrightarrow E_1'$, $A_2' \leftrightarrow E_2'$, $A_2'' \leftrightarrow E_1''$, $A_2'' \leftrightarrow E_2''$, $A_1'' \leftrightarrow E_1''$, and $A_1'' \leftrightarrow E_2''$. For the open-ended (3, 3) SWNTs, the molecular orbitals with A_{1g}, A_{2g}, A_{1u}, and A_{2u} symmetry are found to be energetically

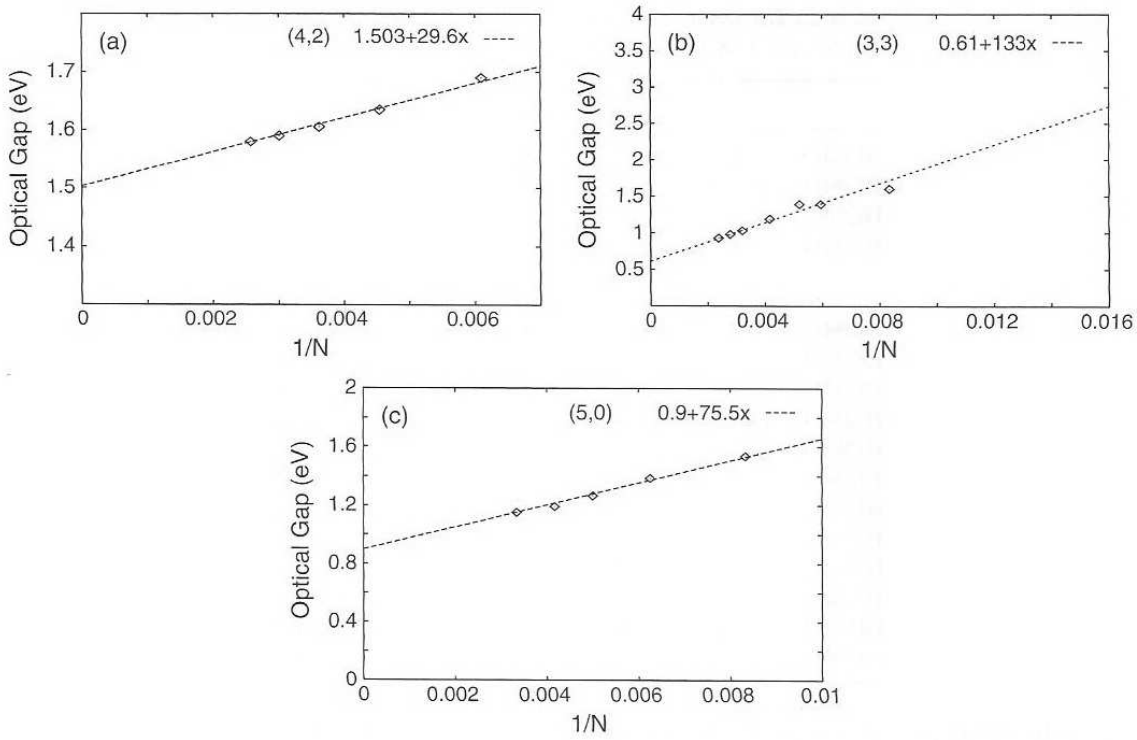

Figure 23. The optical gap versus $1/N$ for open-ended (4, 2), (3, 3), and (5, 0) SWNTs for $\mathbf{E} \parallel \mathbf{T}$, where N is the number of carbon atoms. The dashed lines are linear fits to the calculated results. The optical gaps are 1.50, 0.61, and 0.90 eV for infinite (4, 2), (3, 3), and (5, 0) SWNTs, respectively. Reprinted with permission from [66], W. Z. Liang et al., *J. Am. Chem. Soc.* 123, 9830 (2001). © 2001, American Chemical Society.

close to the HOMO and LUMO. The molecular orbitals with E_u and E_g symmetry are quite different in energy from HOMO and LUMO. The excitation at 1.57 eV of (3, 3) $C_{120}H_{12}$ for $\mathbf{E} \parallel \mathbf{T}$ consists mainly of the transitions $A_{1g} \leftrightarrow A_{2u}$ and $A_{2g} \leftrightarrow A_{1u}$, whereas, the first excitation for $\mathbf{E} \perp \mathbf{T}$ consists mainly of $A_{1g} \leftrightarrow E_u$, $A_{1u} \leftrightarrow E_g$, $A_{2g} \leftrightarrow E_u$, and $A_{2u} \leftrightarrow E_g$ transitions. This explains the fact that the optical gap for $\mathbf{E} \perp \mathbf{T}$ is larger than for $\mathbf{E} \parallel \mathbf{T}$ for (3, 3) SWNTs.

After obtaining the induced density matrices $\delta\rho$ of the transitions corresponding to the absorption peaks at 1.57 and 4.58 eV of (3, 3) $C_{120}H_{12}$, 1.53 and 3.14 eV of (5, 0) $C_{120}H_{10}$, and 0.61 and 2.49 eV of (4, 2) $C_{52}H_{12}$, the matrices are projected onto the HFMO representation [103]. In other words, the dipole-induced excitations are decomposed into the transitions between the pairs of molecular orbitals. The results are shown in Tables 1–3. The molecular orbital transitions whose absolute amplitudes are larger than 0.1 are listed. Because $|\delta\rho_{ij}| = |\delta\rho_{ji}|$, only $\delta\rho_{ij}$ $(i < j)$ are shown, where i and j stand for a pair of molecular orbitals. For (3, 3) $C_{120}H_{12}$, the excitation at 1.57 eV is a $\pi^* - \pi$ transition and consists mainly of the HOMO to LUMO + 1 and HOMO − 1 to LUMO transitions, with their respective amplitudes of 0.44 and 0.36 (see Table 1). Other contributions, such as the HOMO − 2 to LUMO + 3 and HOMO − 3 to LUMO + 2, are much smaller. The excitation at 4.58 eV is also a $\pi - \pi^*$ transition. Its main contributions are from the pairs of the molecular orbitals with E_u and E_g symmetry (see Table 1). The transition from HOMO to LUMO is forbidden for (3, 3) CNTs, as they have A_{1g} and A_{2g} symmetry, respectively. For (5, 0) $C_{120}H_{10}$, the excitations at 1.53 and 3.14 eV are from $\pi - \pi^*$ transitions. The molecular orbitals involved in the transitions have E_1', E_1'', E_2', and E_2'' symmetry (see Table 2). The $A_2'' \leftrightarrow A_1'$ transition has made a small contribution to the excitation at 3.14 eV. The HOMO to LUMO transition is forbidden for (5, 0) as well. For (4, 2) $C_{52}H_{12}$, the excitation at 0.61 eV is a $\pi - \pi^*$ transition, and its main contributions are from the HOMO to LUMO, HOMO − 1 to LUMO + 1, and HOMO − 2 to LUMO + 4 transitions. The excitation at 2.49 eV is also a π to π^* transitions, with the HOMO − 1 to LUMO + 1 transition as the main contributor (see Table 3).

The absorption spectra of the 4-Å SWNTs reported in Ref. [32] were measured recently [81]. The polarization of the light was tuned to examine the anisotropy of the optical

Table 1. The compositions of the photo-induced transitions at 1.57 and 4.58 eV of (3, 3) $C_{120}H_{12}$.

1.57 eV	
HOMO $-$ 1(A_{1u}) $\rightarrow$ LUMO + 0(A_{2g})	0.36
HOMO $-$ 0(A_{1g}) $\rightarrow$ LUMO + 1(A_{2u})	0.44
HOMO $-$ 3(A_{2g}) $\rightarrow$ LUMO + 2(A_{1u})	$-$0.15
HOMO $-$ 2(A_{2u}) $\rightarrow$ LUMO + 3(A_{1g})	$-$0.19
4.58 eV	
HOMO $-$ 18(E_u) $\rightarrow$ LUMO + 9(E_g)	$-$0.11
HOMO $-$ 10(E_u) $\rightarrow$ LUMO + 9(E_g)	0.16
HOMO $-$ 9(E_u) $\rightarrow$ LUMO + 9(E_g)	$-$0.12
HOMO $-$ 17(E_u) $\rightarrow$ LUMO + 10(E_g)	$-$0.11
HOMO $-$ 10(E_u) $\rightarrow$ LUMO + 10(E_g)	0.14
HOMO $-$ 9(E_u) $\rightarrow$ LUMO + 10(E_g)	0.16
HOMO $-$ 11(E_g) $\rightarrow$ LUMO + 11(E_u)	$-$0.23
HOMO $-$ 12(E_g) $\rightarrow$ LUMO + 12(E_u)	0.23
HOMO $-$ 13(E_g) $\rightarrow$ LUMO + 13(E_u)	$-$0.13
HOMO $-$ 14(E_g) $\rightarrow$ LUMO + 14(E_u)	0.13
HOMO $-$ 15(E_u) $\rightarrow$ LUMO + 15(E_g)	$-$0.13
HOMO $-$ 16(E_u) $\rightarrow$ LUMO + 16(E_g)	0.13

The first column lists the transitions between pairs of molecular orbitals, and the second column lists the corresponding composition coefficients of the specific transitions between the molecular orbital pairs. Reprinted with permission from [66], W. Z. Liang, et al., *J. Am. Chem. Soc.* 123, 9830 (2001). © 2001, American Chemical Society.

Table 2. The compositions of the photo-induced transitions at 1.53 and 3.14 eV of (5, 0) $C_{120}H_{10}$.

1.53 eV	
HOMO $-$ 10(E_1'') $\rightarrow$ LUMO + 0(E_1')	0.12
HOMO $-$ 11(E_1'') $\rightarrow$ LUMO + 1(E_1')	0.12
HOMO $-$ 4(E_2') $\rightarrow$ LUMO + 3(E_2'')	0.19
HOMO $-$ 0(E_2') $\rightarrow$ LUMO + 3(E_2'')	$-$0.28
HOMO $-$ 5(E_2') $\rightarrow$ LUMO + 4(E_2'')	0.19
HOMO $-$ 1(E_2') $\rightarrow$ LUMO + 4(E_2'')	0.28
HOMO $-$ 6(E_2'') $\rightarrow$ LUMO + 8(E_2')	0.10
HOMO $-$ 3(E_2'') $\rightarrow$ LUMO + 8(E_2')	0.13
HOMO $-$ 2(E_2'') $\rightarrow$ LUMO + 8(E_2')	$-$0.20
HOMO $-$ 7(E_2'') $\rightarrow$ LUMO + 9(E_2')	0.10
HOMO $-$ 3(E_2'') $\rightarrow$ LUMO + 9(E_2')	$-$0.20
HOMO $-$ 2(E_2'') $\rightarrow$ LUMO + 9(E_2')	$-$0.13
HOMO $-$ 1(E_2') $\rightarrow$ LUMO + 13(E_2'')	0.11
HOMO $-$ 0(E_2') $\rightarrow$ LUMO + 13(E_2'')	0.11
HOMO $-$ 1(E_2') $\rightarrow$ LUMO + 14(E_2'')	$-$0.11
HOMO $-$ 0(E_2') $\rightarrow$ LUMO + 14(E_2'')	0.11
3.14 eV	
HOMO $-$ 10(E_1'') $\rightarrow$ LUMO + 0(E_1')	$-$0.25
HOMO $-$ 11(E_1'') $\rightarrow$ LUMO + 1(E_1')	$-$0.25
HOMO $-$ 24(A_2'') $\rightarrow$ LUMO + 2(A_1')	$-$0.11
HOMO $-$ 4(E_2') $\rightarrow$ LUMO + 3(E_2'')	0.19
HOMO $-$ 0(E_2') $\rightarrow$ LUMO + 3(E_2'')	0.12
HOMO $-$ 5(E_2') $\rightarrow$ LUMO + 4(E_2'')	0.19
HOMO $-$ 1(E_2') $\rightarrow$ LUMO + 4(E_2'')	$-$0.12
HOMO $-$ 14(E_1') $\rightarrow$ LUMO + 6(E_1'')	0.10
HOMO $-$ 15(E_1') $\rightarrow$ LUMO + 7(E_1'')	0.10
HOMO $-$ 6(E_2'') $\rightarrow$ LUMO + 8(E_2')	0.11
HOMO $-$ 7(E_2'') $\rightarrow$ LUMO + 8(E_2')	0.11

The first column lists the transitions between pairs of molecular orbitals, and the second column lists the corresponding composition coefficients of the specific transitions between the molecular orbital pairs. Reprinted with permission from [66], W. Z. Liang, et al., *J. Am. Chem. Soc.* 123, 9830 (2001). © 2001, American Chemical Society.

Table 3. The compositions of the photo-induced transitions at 0.61 and 2.49 eV of (4, 2) $C_{52}H_{12}$.

1.61 eV	
HOMO − 0 → LOMO + 0	−0.72
HOMO − 1 → LOMO + 1	−0.34
HOMO − 2 → LOMO + 4	−0.25
HOMO − 4 → LOMO + 6	0.12
2.49 eV	
HOMO − 0 → LOMO + 0	−0.15
HOMO − 1 → LOMO + 1	0.53
HOMO − 3 → LOMO + 2	0.19
HOMO − 5 → LOMO + 3	−0.18
HOMO − 2 → LOMO + 4	0.19
HOMO − 4 → LOMO + 6	−0.15
HOMO − 2 → LOMO + 6	0.14

The first column lists the transitions between pairs of molecular orbitals, and the second column lists the corresponding composition coefficients of the specific transitions between the molecular orbital pairs. Reprinted with permission from [66], W. Z. Liang, et al., *J. Am. Chem. Soc.* 123, 9830 (2001). © 2001, American Chemical Society.

response. Several important observations were obtained. First, for $\mathbf{E} \parallel \mathbf{T}$, three absorption peaks were identified at 1.35, 2.15, and 3.10 eV. Second, As **E** deviates from the tube's parallel direction to its normal direction, the absorption intensity weakens significantly, and moreover, the spectra red-shift. Third, the 4-Å SWNTs are transparent for $\mathbf{E} \perp \mathbf{T}$. The absorption spectrum of the (3, 3) SWNT has only one major peak below 4.0 eV. When the electric field is parallel to the tube, there are three distinctive absorption peaks below 4 eV for (5, 0) SWNTs and two peaks below 4.0 eV for (4, 2). Both of these numbers are consistent with the experimental measurement. Because the parameters in the PM3 Hamiltonian were not optimized for the TDHF method, which is employed in the LDM calculation, the calculated absorption spectra red-shift with respect to the experimental spectra. Nevertheless, the calculated and measured absorption spectra agree qualitatively. It is clear that the (3, 3) SWNT alone can not account for the measured absorption spectrum, and it may explain only the first peak at 1.37 eV in the measured spectrum. The calculated absorption spectra of (4, 2) and (5, 0) are consistent with the measured spectra. Because it is energetically unfavorable to fit half C_{20} caps on (4, 2) SWNTs [32], only the *H*-terminated (4, 2) SWNTs may exist. The sharp peak at 1.37 eV in the measured absorption spectrum agrees very well with the first peak in the absorption spectrum of (4, 2). This seems to indicate that (4, 2) SWNT is the most likely candidate. However, the porous AFI crystals were thermally treated at 500°–800°C during the synthesis [32], and it is not clear that *H* atoms inside the pores survive the thermal treatment. This may be resolved by examining the energetics of *H*-terminated (4, 2) or the binding energies of the terminal *H* atoms, and additional calculations are required. If the 4-Å SWNTs synthesized in the porous AFI crystals are of a single chirality, they should be either the *H*-terminated (4, 2) or (5, 0) SWNTs. Of course, a mixture of three SWNTs (4, 2), (3, 3), and (5, 0) cannot be ruled out.

The chirality has a strong influence on the absorption spectra of 4-Å SWNTs. This differs from previous findings [65] of larger-diameter SWNTs, where the chirality has a much abated effect on the absorption spectra. Because of their sensitive dependence on the chirality, the absorption spectra are used to determine the structure of 4-Å SWNT. The optical responses of the 4-Å SWNTs are highly anisotropic. This is because the transition dipole moments parallel to the tube are much larger than the moments perpendicular to the tube. The anisotropy is clearly demonstrated in Figs. 20, 21, and 22. The optical responses of the 4-Å SWNTs are highly anisotropic. This is because the transition dipole moments parallel to the tube are much larger than the moments perpendicular to the tube. The anisotropy is clearly demonstrated in Figs. 20, 21, and 22. Similar to the findings from the larger-diameter SWNTs, the optical gaps of the infinite (3, 3), (4, 2), and (5, 0) SWNTs are all finite, being 0.6, 1.5, and 0.9 eV, respectively. This is despite the fact that the LDA calculation

predicts that all three 4-Å SWNTs are metallic [98]. The existence of the finite optical gap is consistent with the measured absorption spectra [81].

3.4. Effect of Functionalization on Optical Spectra of Metallic Single-Walled Carbon Nanotubes

Modern synthetic chemistry and biological processes primarily take place in the solution phase. However, SWNTs typically exist in forms of raw ropes or bundles about 10–25 nm in diameter and a few micrometers in length. Because SWNT bundles are entangled together in the solid state to form a highly dense, complex network structure, it is difficult to develop a dissolution process for the SWNTs. It is possible to wet the SWNT raw soot in refluxing nitric acid, whereby the end caps of the tubes are oxidized to carboxylic acid and other weakly acidic functionalities [104–107]. In certain instances, covalent chemistry on the side walls of the SWNTs is a viable route to soluble materials [108]. In fact, the ability to carry out controlled covalent chemistry on the side walls of the SWNTs is a very important step, and the achievement of systematic and predictable side-wall chemistry is likely to be a precursor to many of the applications that are currently envisioned for CNTs.

It was previously known that ionic doping with electron acceptors introduces holes into the valence band that can lead to the removal of the interband transitions in semiconducting SWNTs [90]. Recently, it was shown that covalent chemistry can covert the metallic SWNTs to semiconductors, which may lead to efficient nanotube separation [38, 39]. Kamaras et al. showed that reactions with dichlorocarbene rapidly opens a gap near the Fermi level of the metallic CNTs. Strano et al. demonstrated that diazonium agents allow functionalization of SWNTs suspended in aqueous solution with high selectivity and display an autocatalytic effect that functionalizes the entire tube. In particular, metallic species are selected to react to the near exclusion of semiconducting SWNTs under controlled conditions [39]. The optical absorption spectrum is used to monitor the valence-to-conduction electronic transitions.

Here the LDM-PM3 method is employed to study the effect of functionalization on optical absorption spectra of metallic SWNTs. The hydrogenated armchair SWNT (5, 5) ($C_{140}H_{20}$ and $C_{140}H_{20}-C_6H_4Cl$) are selected for absorption spectra calculations. When one functional group is attached to the tube side wall, a double bond is broken, and the functionalized SWNT can receive electrons from neighboring nanotubes or can react with fluoride and diazonium salts. In our model, one ($—C_6H_4Cl$) is attached to the (5, 5) SWNT, and one hydrogen atom is put in to neutralize the free radical. The amount of functionality addition is 7.1 mol per 1000 mol carbon when one ($—C_6H_4Cl$) functionality is attached to the (5, 5) SWNT. An arene-functionalized (5, 5) SWNT is shown in Fig. 24a with $—C_6H_4Cl$ attached to one side of the tube and a hydrogen atom to the other side. Optical absorption spectra are calculated for (5, 5) SWNTs with and without functionalities. In Fig. 24, the effect of functionalization is illustrated by comparing the spectrum of the stand-alone

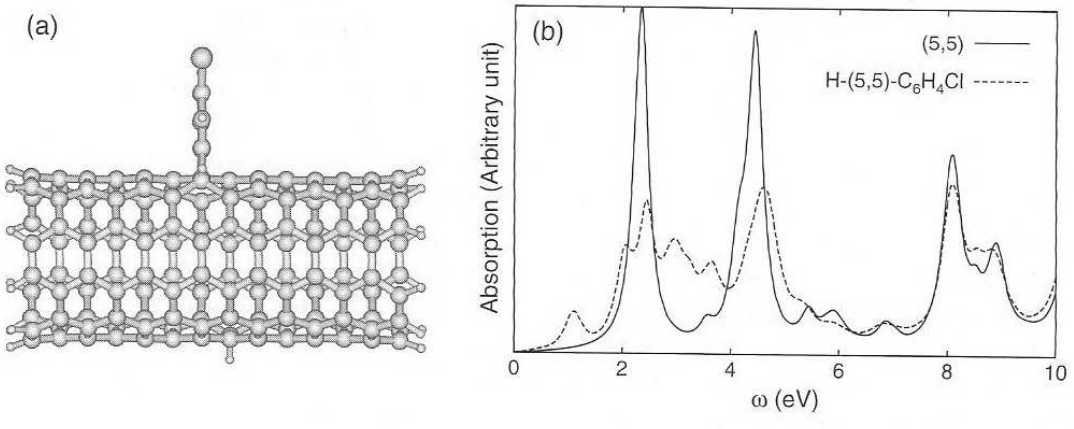

Figure 24. (a) The structure of the functionalized (5, 5) SWNT: $C_{120}H_{20}-C_6H_4Cl-H$. (b) Absorption spectra of the (5, 5) metallic SWNT and the functionalized (5, 5) SWNT.

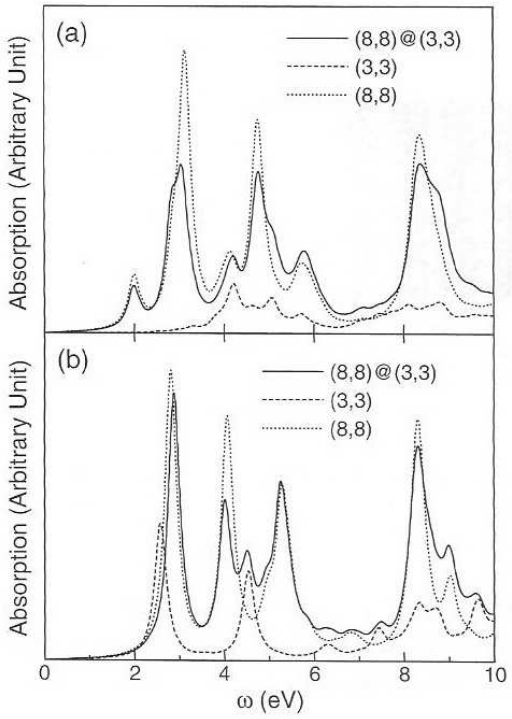

Figure 25. Absorption spectrum of a (3, 3)@(8, 8) DWNT (solid) is shown together with those of a (3, 3) SWNT (dashed) and a (8, 8) SWNT (dotted). The external field is (a) perpendicular or (b) parallel to the nanotube axis. Both tubes in the DWNT are 15.4 Å.

(5, 5) SWNT with that of the arene-functionalized (5, 5) SWNT. The low-energy metallic absorption peaks of the (5, 5) SWNT (below 5 eV) are greatly reduced in intensities on functionalization, in full agreement with measurements [39]. The effect of functionalization on the high-energy features near 8 eV, however, is much less pronounced.

The effect of functionalization on optical absorption spectra of semiconducting SWNTs has also been examined in this study. Similar changes of calculated absorption spectra on

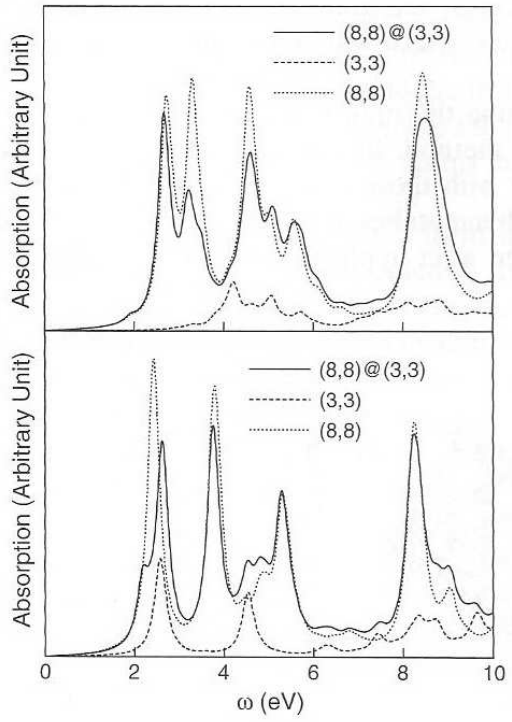

Figure 26. Absorption spectrum of a (3, 3)/(8, 8) DWNT (solid) is shown with those of a (3, 3) SWNT (dashed) and a (8, 8) SWNT (dotted). The DWNT is composed of nanotubes of unequal lengths. The inner tube of the DWNT is 15.4 Å, and the outer tube is 20.4 Å. The external field is (a) perpendicular or (b) parallel to the nanotube axis.

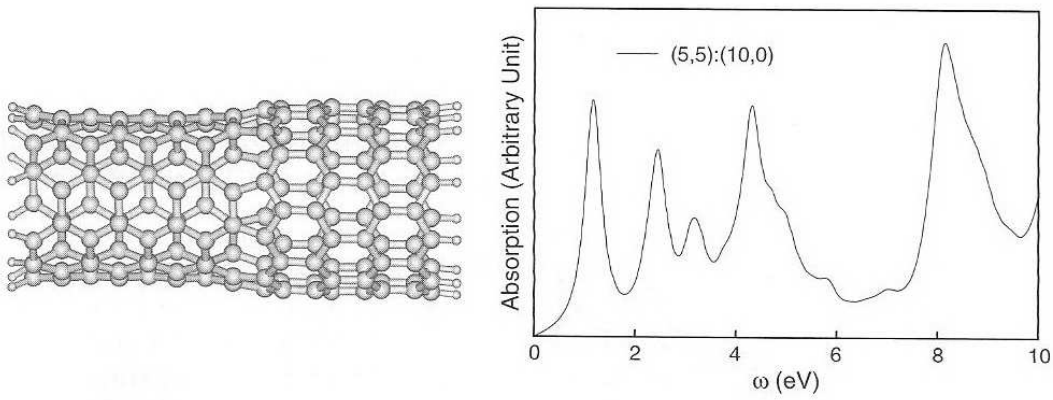

Figure 27. Absorption spectrum for a coaxial CNT junction between a (5, 5) SWNT and a (10, 0) SWNT. The external light field is along the nanotube axis. The lowest absorption peak is attributed to the (10, 0) part of the junction via a density-matrix analysis, whereas the second (~2.4 eV) and fourth (~4.3 eV) peaks have contributions from both the (5, 5) and (10, 0) components of the junction.

functionalization are found. The fact that experimentally semiconducting peaks are not altered on functionalization in the work of Strano et al. [39] confirms the high selectivity of functionalization in the presence of diazonium agents.

3.5. Absorption Spectra of Multiwalled Nanotubes and Carbon Nanotube Junctions

Multiwalled nanotubes (MWNTs) are representative of a unique class of self-organized solids with structural hierarchy. Compared with SWNTs, modifications in the electronic properties are introduced by the internanotube interactions in MWNTs [109–111]. For instance, those interactions are known to cause a small band repulsion and a pseudogap near E_F for metallic CNTs [112, 113]. Thin DWNTs have been synthesized by fusion of fullerenes encapsulated in SWNTs [41, 114] via electron beam irradiation on the carbon peapods, which induces coalescence of fullerenes. Optical absorption spectra of DWNTs will be studied here and compared with those of individual SWNTs that compose the corresponding DWNTs. Also of great interest are optical properties of the nanotube junctions [115] and CNTs with structural defects, which will be examined here with the help of the LDM-PM3 algorithm.

We start out by examining the optical absorption spectra of DWNTs, calculated by the semiempirical LDM-PM3 method. In Fig. 25, the absorption spectrum of a (3, 3)@(8, 8) DWNT is shown together with those of a (3, 3) SWNT and an (8, 8) SWNT of the same lengths as the DWNT. Both nanotubes in the DWNT are 15.4 Å. In the upper panel, Fig. 25a, the lineshapes are obtained after applying an external field perpendicular to the nanotube

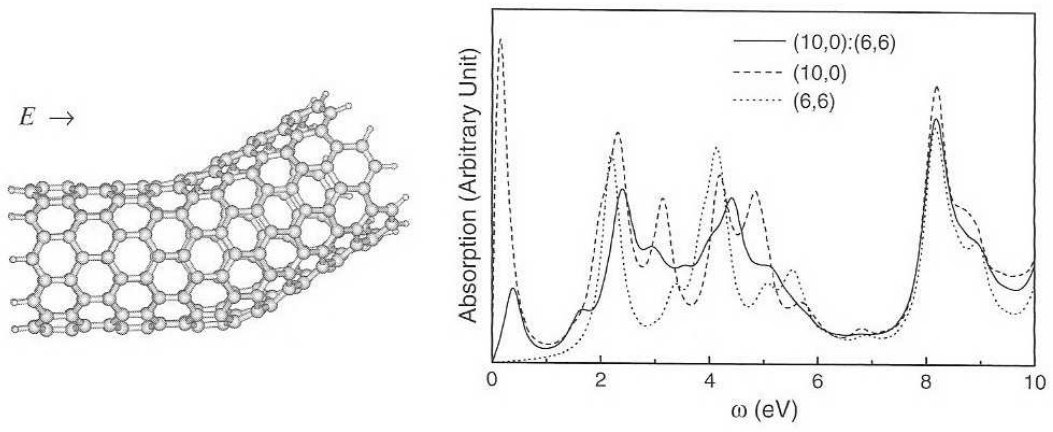

Figure 28. Absorption spectrum for a CNT junction between a (6, 6) SWNT and a (10, 0) SWNT. The (6, 6) and (10, 0) segments are oriented to form an angle of about $\pi/6$. The external light field is along the direction of the (6, 6) SWNT. Absorption spectra of a (6, 6) SWNT and a (10, 0) SWNT are also shown for comparison.

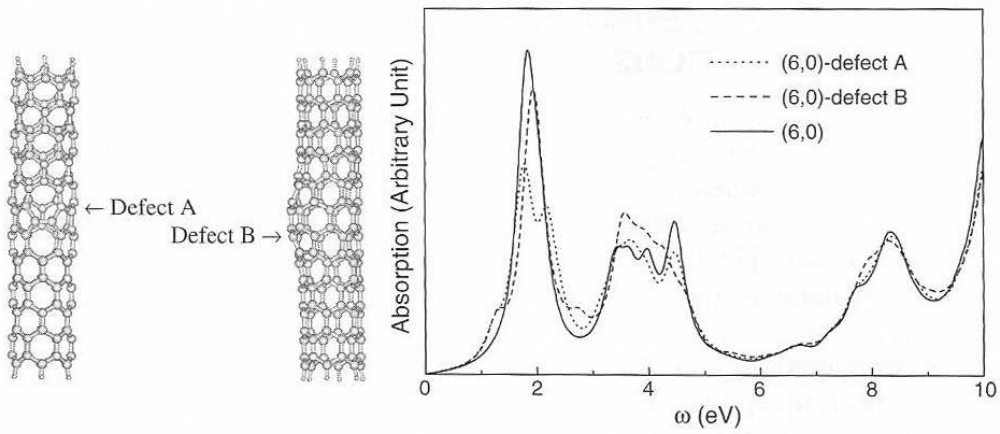

Figure 29. Absorption spectrum for a (6, 0) SWNT is compared with those of two (6, 0) SWNTs with defects.

axis. The contribution from the inner (3, 3) tube seems to be small, and the spectra of the DWNT resemble that of the outer (8, 8) for $\mathbf{E} \perp \mathbf{T}$. In the lower panel, Fig. 25b, the external field is parallel to the nanotube axis ($\mathbf{E} \parallel \mathbf{T}$), and the contribution from the inner (3, 3) tube is much more significant. The first absorption peak of the DWNT has a slightly higher energy than both isolated (8, 8) and (3, 3) SWNTs. High-energy peaks of the SWNT located between 4 and 5.5 eV are a combination of peaks from the isolated SWNTs.

In comparison, absorption spectra of (3, 3) and (8, 8) DWNT tubes of unequal lengths are shown in Fig. 26. The inner tube of the DWNT is 15.4 Å, and the outer tube is 20.4 Å. For $\mathbf{E} \perp \mathbf{T}$, the absorption spectrum of the DWNT in Fig. 26a, although differing from that in Fig. 25a, remains sufficiently close to that of an isolated (8,8) SWNT with a length of 20.4 Å. The contribution from the inner tube for $\mathbf{E} \perp \mathbf{T}$ is minimal. For $\mathbf{E} \parallel \mathbf{T}$, the absorption lineshape of the DWNT is practically a linear combination of those of isolated (3, 3) and (8, 8) SWNTs with similar lengths, as shown in Fig. 26b. Compared with the spectrum in Fig. 25b, the major peak positions in Fig. 26b are located at similar energies, and the change in nanotube lengths merely alters the relative strengths of the peaks.

Shown in Fig. 27 is the optical absorption spectrum of a coaxial CNT junction between a (5, 5) SWNT and a (10, 0) SWNT. The external light field is along their common axis. The lowest absorption peak is attributed to the (10, 0) part of the junction with the help of a density-matrix analysis, whereas the second (~2.4 eV) and the forth (~4.3 eV) peaks receive contributions from both the (5, 5) and (10, 0) components of the junction. The weakest low-energy excitation; that is, the third peak at about 3.2 eV, seems mostly caused by the (10, 0) segment.

A CNT junction can also be constructed in a noncoaxial form, as demonstrated in Fig. 28. The (6, 6) and (10, 0) segments of the junction are oriented to form an angle of about $\pi/6$ between them. The external field is along the direction of the (6, 6) SWNT. Two prominent absorption features at about 2.4 eV and 4.3 eV are found in addition to a structure near 8 eV. Overall, the absorption spectrum of the noncoaxial junction is approximately an average over those of the (6, 6) and (10, 0) segments, as shown in Fig. 28.

Last, we examine the effect of wall defects on the optical properties of SWNTs. A combination of two pairs of the so-called "5+7 member rings" (one pentagon and one heptagon) is the simplest point defect that keeps the carbon nanotube in a straight line with C_{2v} symmetry. In Fig. 29, we modeled two different types of point defects by introducing two pairs of "5 + 7 member-rings" on a (6, 0) SWNT. (In fact, the noncoaxial CNT junction in Fig. 28 is also constructed using two pairs of "5 + 7 member rings.") For example, if one C–C bond at the central part of the SWNT is rotated by $\pi/2$ to arrive at two pairs of "5 + 7 member-rings," the type of point defects formed this way is called Defect A, and the original 66 carbon hexagons are now replaced by 62 hexagons and two pairs of "5 + 7 member-rings." The absorption spectrum for a perfect (6, 0) SWNT is compared with those of two (6, 0) SWNTs with wall defects in Fig. 29. It is found that such localized wall defects have no significant effect on the absorption spectra of the SWNTs.

4. FIRST-PRINCIPLES DENSITY-FUNCTION THEORY CALCULATIONS

First-principles calculations have been carried out on SWNTs [116, 117], including those with the smallest diameter (4 Å) [118]. Moreover, the detailed plane-wave *ab initio* pseudopotential local density approximation (LDA) calculations [98] predicted that all small-diameter tubes are conductors regardless their chiralities. Recently, *ab initio* calculations have been performed on the anisotropic dielectric response of small-diameter SWNTs in the framework of time-dependent density-functional theory (DFT) [119] with results in good agreement with experiment.

DFT-based configurations and electronic structures were optimized for finite open (4, 4) and (5, 5) SWNTs [120], and results show that charge distributions and bond lengths/angles at tube ends and those on tube side walls differ significantly. As DFT studies have revealed, rehybridization of σ and π orbitals and interactions among π orbitals caused by the curvature of the tube lead to significant modifications of the electronic band structures [98]. It is thus plausible that orbital rehybridization and electronic interactions that are taken into account in the DFT approach may cause quantitative or even qualitative alternations to the simplified tight-binding absorption spectra. To supplement our semiempirical LDM method, we have therefore employed a first-principles DFT approach [121, 122] to calculate the optical response of isolated SWNTs with periodic boundary conditions. Calculations are performed with the WIEN97 software package [123] based on the full potential linearized augmented plane waves (LAPW) method. In the LAPW method, the unit cell is divided into two types of regions: the atomic spheres centered at nuclear sites and the interstitial region between the nonoverlapping spheres. Within the atomic spheres, the wave function is expanded in terms of atomic wave functions, and in the interstitial region the wave function is expanded in terms of plane waves. Optical properties of SWNTs are obtained by combining the joint density of states (JDOS) and transition dipole matrix elements. Results are compared with those from the tight-binding model and the LDM method in the next section.

It has been shown [114, 124, 125] that carbon nanotubes can encapsulate fullerenes. In Ref. [124], this so-called carbon peapod is found to be a metal with multicarries distributed both along the nanotube and on the C_{60} chain. These examples show that through chemical doping, the electronic properties of nanotubes can be modified. As mentioned earlier, potassium iodide has been successfully inserted into a (10, 10) SWNT [41, 42]. Lattice distortions are observed that are attributed to the difference in K:I coordination from the bulk crystal and to interactions between the KI crystal and the tubule wall. Here we employ the first-principles DFT approach to calculate the electronic structure of the KI intercalated (10, 10) carbon nanotube. The resulting KI/SWNT composite is a highly anisotropic one-dimensional structure whose electronic and optical properties are expected to be considerably modified with respect to those of the bulk halide and the encapsulating nanotube.

In the calculation we adopt the experimental structure of KI@(10, 10) reported in Ref. [41]. The structure is depicted in Fig. 30. The muffin-tin radii are set to 1.30, 2.61, and

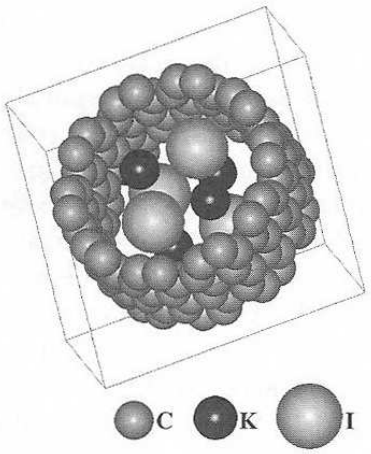

Figure 30. Unit cell of a (10, 10) carbon nanotube having potassium iodide inside.

Table 4. Charges distribution of KI@(10, 10), (10, 10) SWNT, and KI.

	Charges		
Region	KI@(10, 10)	(10, 10)	KI
C_{120}	401.73	436.48	—
K_4I_4	281.53	—	282.53
Interstitial	324.74	283.52	5.47

3.50 atomic units for carbon, potassium, and iodine, respectively. The lattice parameters of KI@(10, 10) in our calculation are a = 18 Å, b = 18 Å, and c = 7.384 Å. Linear chains of K and I are put into each nanotube, and each unit cell contains $K_4I_4C_{120}$. Across the SWNT capillaries, K and I are spaced at intervals of 4.0 Å, whereas along the SWNT capillaries, the spacing is 3.69 Å to maintain the periodicity. The center-to-center distance between the nanotubes in the neighboring cells is set to 18 Å, which was found to be large enough to prevent intertubule interactions. To achieve self-consistency for the electronic structure calculations, we use one k point in the irreducible part of the Brillouin zone, and the calculation is considered to be achieved when the energy variation for the k point between two consecutive iterations does not exceed 10^{-5} Ry.

Table 4 shows the charges in the atomic spheres and interstitial regions of KI@(10, 10) nanotube, (10, 10) nanotube, and linear chain KI. In the calculation of a linear chain KI, we use the same unit cell as the KI@(10, 10), with the carbon atoms removed. Each unit cell contains four potassium and iodine atoms. The results show that there is a substantial amount of charge transfer from the carbon atomic spheres into the interstitial region on the KI intercalation. On the average there are 0.3 electrons per carbon atom transferred from the atomic sphere region to the interstitial region, although there are only about 0.12 electrons per *K* and I transferred to the interstitial region. Hence, we expect some significant change in the electronic structure of the (10, 10) SWNT on intercalation.

Electronic energy bands for (10, 10) and KI@(10, 10) CNTs are given in Fig. 31a and 31b, respectively. The cell used in the calculation for (10, 10) contains 120 carbon atoms, which is three times as many as those of the (10, 10) unit cell. This is chosen to match with the unit cell of KI@(10, 10), so that a direct comparison of the electronic structures between (10, 10) and KI@(10, 10) is more clear (see Fig. 31). Both the (10, 10) SWNT and KI@(10, 10) SWNT show the metallic character. It is found that I's 5p orbitals contribute to the flat energy bands near −1 eV in Fig. 31b, and the conduction bands between 1 and 5 eV in Fig. 31b contain large contributions from K's 4s orbitals. We plot the DOS in Fig. 32.

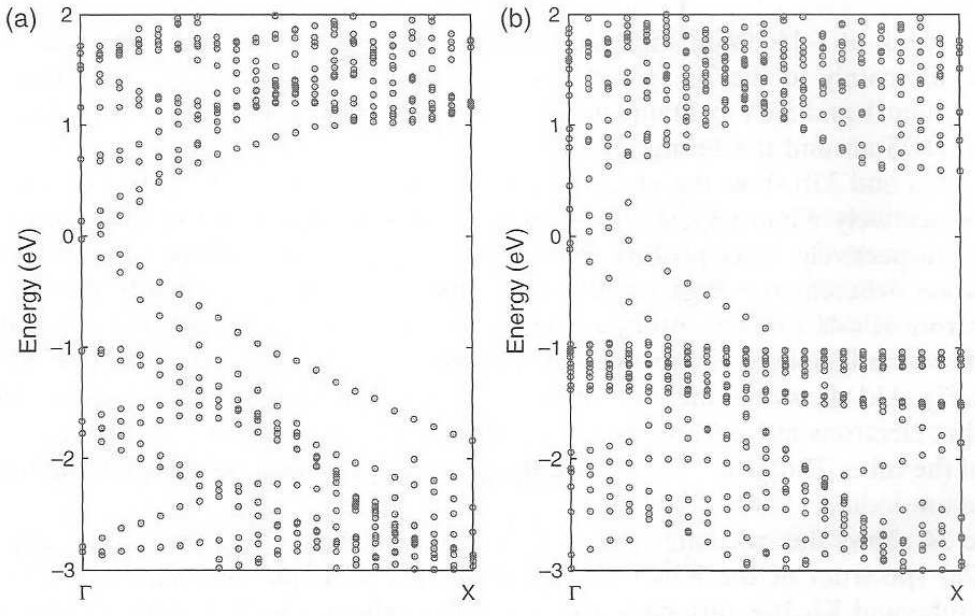

Figure 31. Calculated band structures of (a) (10, 10) carbon nanotube and (b) KI@(10, 10). Energies are measured from the Fermi level energy.

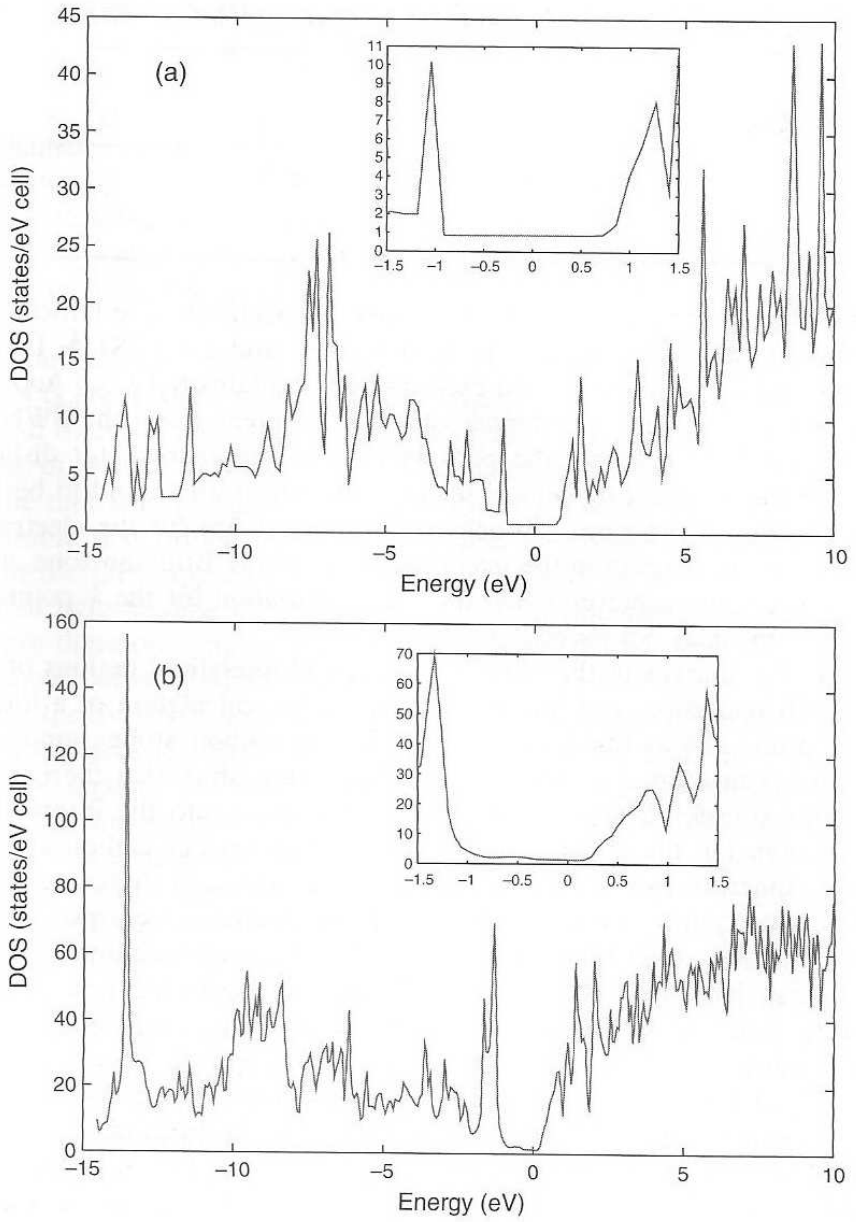

Figure 32. Density of states for (a) (10, 10) carbon nanotube and (b) KI@(10, 10). The Fermi level is at 0 eV.

The huge peak at −15 eV in Fig. 32b belongs to K's 3p orbitals, and the peak at −1 eV corresponds mainly to the I's 5p orbitals. Among other contributions, the broad band of peaks between 1 and 5 eV contains those from K's 4s orbital. The insets in Fig. 32a and 32b show the DOS around the Fermi level.

Figure 33a and 33b show the electron density contour plots for (10, 10) and KI@(10, 10) CNTs, respectively. Figure 33c and 33d show the positive and negative differences between the two, respectively, and positive means the decrease of electron density on the KI intercalation, whereas the negative means the increase of density. Clearly there is electron transfer from K's 4s to I's 5p orbitals. Figure 33c shows the decrease of electron density in the carbon atomic sphere regions of KI@(10, 10) CNTs with respect to those of (10, 10), whereas Fig. 33d shows the increase of electron density in the interstitial region. This shows clearly that electrons move from the atomic sphere region of carbon atoms to the interstitial region of the tube. Thus, the electrons on the tube become more delocalized on intercalation of potassium iodide.

Figure 34 shows the calculated absorption spectra of KI@(10, 10), (10, 10), and KI. The absorption spectrum of the KI@(10, 10) tube is not a simple summation of those of the (10, 10) tube and KI. It is observed that the peak at about 1.8 eV broadens considerably on intercalation. This is consistent with our calculation result that the DOS changes near the Fermi level on the KI intercalation, as indicated by the insets of Fig. 32.

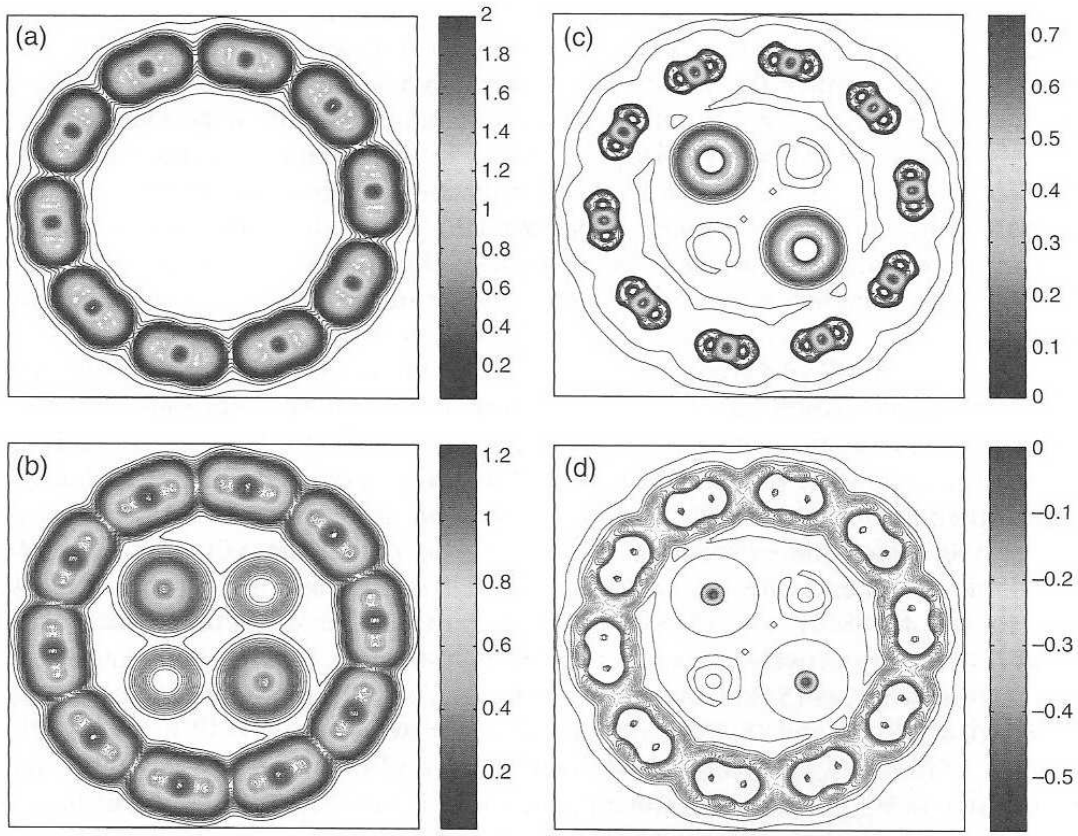

Figure 33. Contour plots of the electron density of (a) (10, 10) carbon nanotube and (b) KI@(10, 10). The contour plots of a more positively charged area and one more negatively charged than a simple sum of two charge densities of the nanotube and KI are shown in (c) and (d) respectively.

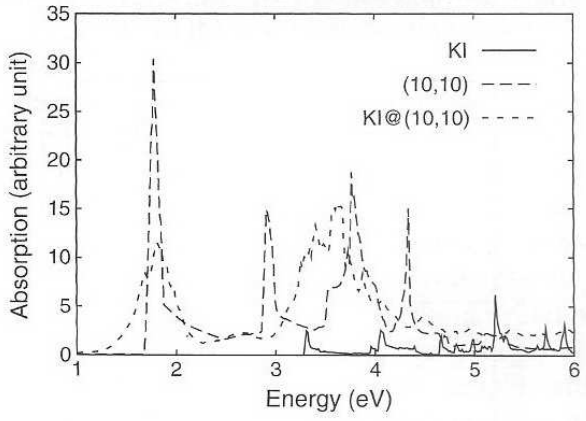

Figure 34. Absorption spectrum of KI@(10, 10), (10, 10) nanotube, and KI.

The electronic structure of potassium iodide intercalated carbon nanotubes has been investigated. On intercalation, the electrons in the SWNT become much more delocalized, indicating strong interactions between KI and the nanotube wall. The interactions alter the electronic structures and the DOS near the Fermi level. The calculated band structures and DOSs reflect these changes. The intercalations thus have the potential to drastically change the physical properties of CNTs.

5. COMPARISON OF THE TIGHT-BINDING, LOCALIZED-DENSITY-MATRIX AND DENSITY-FUNCTION THEORY APPROACHES

Rehybridization of σ and π orbitals and electronic correlations are known to affect the band structure, DOS, and transition dipole, and thus lead to substantial changes of the absorption spectrum. The tight-binding model presented in Section 2 grossly simplifies the electronic

dynamics in the nanotubes. For example, curvature effects are known to introduce small energy gaps in "metallic" zigzag SWNTs that depend inversely on the square of the tube radius [126–128]. Whether the low-energy absorption features as predicted by the tight-binding model survive rehybridization and correlation effects remains to be seen. To compare with the tight-binding low-energy absorption peaks, in this section we explicitly include the electron correlations and the σ–π orbital rehybridization by using the LDM-PM3 method. It is followed by employing the first-principles DFT [123]. It is shown that those low-energy spectral features, as illustrated by the tight-binding theory, persist in the presence of electron–electron Coulomb interactions [129] and σ–π orbital rehybridization, and are thus universal.

The optical responses of carbon nanotubes are highly anisotropic, as has been demonstrated by the tight-binding and LDM calculations in the previous sections [48]. Because of their unique geometric structure, the transition dipoles along the tubule axis **T** greatly exceeds their components perpendicular to **T**. For the purpose here of comparing various theoretical predictions of the SWNT optical absorption lineshapes, we again consider only the scenario in which the external field is parallel to the tubule axis (**E** ∥ **T**), and thus the transition occurs exclusively between the orbitals of the same momenta **k** [51]. Three SWNTs, the (6, 4), (8, 0), and (5, 5) nanotubes, have similar diameters, which are 6.83, 6.26, and 6.78 Å, respectively. According to the tight-binding theory, (8, 0) and (6, 4) are semiconductors, whereas (5, 5) is a metal. In Fig. 35a, we plot the tight-binding absorption spectra of (6, 4), (8, 0), and (5, 5) nanotubes. The first two peaks at $0.42|V_{pp\pi}|$ ($0.48|V_{pp\pi}|$) and $0.80|V_{pp\pi}|$ ($0.83|V_{pp\pi}|$) belong to the semiconducting (6, 4) [(8, 0)] nanotube, and the third peak at $1.18|V_{pp\pi}|$ belongs to the metallic (5, 5) nanotube. All three tubes have large absorption peaks near $2|V_{pp\pi}|$ that are not shown in Fig. 35a.

The first two peaks of the (6, 4) nanotube are 0.36 and 0.68 of the lowest peak of the (5, 5) nanotube in energy, which are close to 1/3 and 2/3, respectively. The slight deviation stems from a minor departure of the $E_c - E_v$ contour from the circular feature near the K points, the so-called trigonal warping effect [44]; and deviation of $E_c - E_v$ from its linear

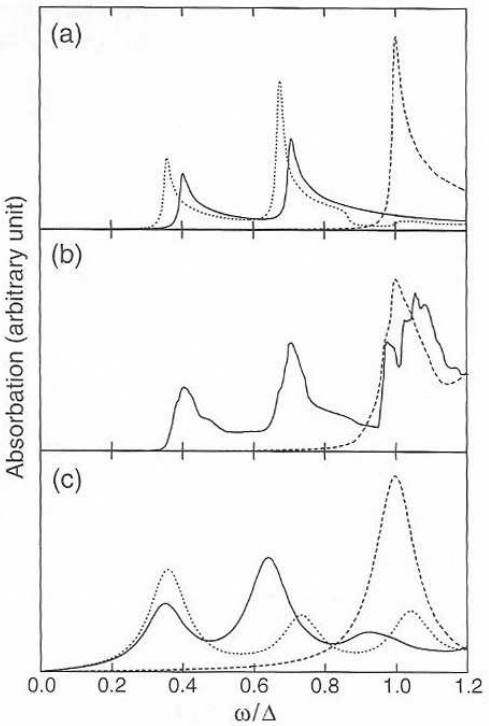

Figure 35. Calculated absorption spectra from (a) the tight-binding model, (b) DFT calculations implemented by the WIEN97 code, and (c) the LDM algorithm are shown for carbon nanotubes of three chiralities: (8, 0) (solid lines), (5, 5) (dashed lines), and (6, 4) (dotted lines); (6, 4) and (8, 0) are semiconducting, and (5, 5) is metallic. The symbol Δ labels the energy of the (5, 5) SWNT's first absorption peak: (a) $\Delta = 1.18|V_{pp\pi}|$, (b) $\Delta = 2.76$ eV, and (c) $\Delta = 2.34$ eV. A dephasing constant of 0.16 eV is used to generate the LDM spectra. Reprinted with permission from [43], Y. Zhao et al., *Chem. Phys. Lett.* 387, 149 (2004). © 2004, Elsevier B. V.

behavior as **k** moves away from the K point. The $(8, 0)$ nanotube has a smaller diameter so that its absorption spectrum is blue-shifted compared to that of $(6, 4)$, and its first and second peaks are 0.41 and 0.70 of the lowest peak of $(5, 5)$, respectively.

Using the full-potential LAPW method implemented in the WIEN97 code [123], we have carried out the spectral calculations for two SWNTs: $(5, 5)$ and $(8, 0)$. Exchange and correlation are included via the local spin-density approximation (LSDA) within the DPT, using the Perdew–Wang parameterization [130]. Optical absorption spectra are calculated via the sum-of-states approach, taking into account pairwise interband transitions [123]. The resulting absorption spectra are shown in Fig. 35b. The lowest peak of the $(5, 5)$ nanotube centers at ~2.76 eV, and the lowest two peaks of $(8, 0)$ are 1.12 eV and 1.95 eV, which are 0.41 and 0.71 of the first peak of $(5, 5)$ (2.76 eV), respectively. The DFT results of the $(5, 5)$ and $(8, 0)$ tubes therefore closely resemble those from the tight-binding model. We conclude that the tight-binding spectral features survive the inclusion of σ–π orbital rehybridization, as shown here by the first-principles DFT calculations.

The LDM method [48], which is size consistent and based on the random phase approximation, considers full single-electron excitation configurations and partial multiple-electron excitation configurations. Because all valence electrons are treated explicitly, the LDM calculation accounts for the σ–π orbital rehybridization as well. Absorption spectra of $(5, 5)$ and $(9, 0)$ SWNTs calculated by the LDM method were found to be similar, which led to our earlier hypothesis that the SWNT absorption lineshapes are mainly determined by their diameters [49]. The calculated LDM absorption spectra of the $(8, 0)$, $(5, 5)$, and $(6, 4)$ SWNTs (C_{128} H_{16}, C_{140} H_{20} and C_{148} H_{20}, respectively) are shown in Fig. 35c. The lengths of the $(8, 0)$, $(5, 5)$, and $(6, 4)$ SWNTs are approximately the same, at 14.92, 14.74, and 15.64 Å, respectively. The PM3 Hamiltonian is employed in the LDM calculations. The first absorption peak of the $(5, 5)$ tube is at 2.34 eV. The lowest two absorption peaks for the $(6, 4)$ tube are at 0.84 and 1.72 eV, which are 0.36 and 0.74 of 2.34 eV, respectively, and for the $(8, 0)$ tube, they are 0.82 and 1.49 eV, which are 0.35 and 0.64 of 2.34 eV, respectively. The LDM results are in approximate agreement with those from the tight-binding model. Discrepancies between the LDM and tight-binding results for the $(8, 0)$ SWNT may be attributed to its small size.

As mentioned earlier, most recent spectrofluorimetric measurements on SWNTs isolated in aqueous surfactant suspensions [35, 131–133] show that for semiconducting nanotubes the tight-binding model can also account for qualitatively small deviations of absorption peaks' dependence on diameter from linear relations, which bear signatures of nanotube chiral angles. Although a consensus on the strength on the electron–hole interaction has yet to emerge [134], that the central value of the energy ratios E_{22}/E_{11} is found to be slightly smaller than 2 [35, 34, 135] is attributed to many-electron correlation effects [35, 136, 137]. First and second van Hove transition wavelengths have been observed directly for 33 semiconducting SWNTs in a surfactant-suspended bulk sample, with each of these species assigned a (n, m) index [35, 131–133], and spectral transitions of six additional SWNT species have been reported in a study of SWNTs of slightly larger diameters [138]. From identified nanotubes ranging from 0.62 to 1.41 nm in diameter and from 3 to 28 degrees in chiral angle, measured transition frequencies have been used to anchor empirical fitting functions that allow extrapolation beyond the measured set [35, 135]. Such extrapolated spectral frequencies have been recently used to constrain theories on SWNT excitonic effects [137].

6. SUMMARY

A large literature of theoretical calculations exists on the electronic structures and optical properties of SWNTs [20–23, 88, 89, 116, 117, 139, 140]. Tight-binding [20–23] and DFT calculations [116, 117] conclude that an (m, n) SWNT is conductor if $m - n \bmod 3 = 0$ and is a semiconductor if $m - n \bmod 3 \neq 0$ [20–23]. Lin et al. studied the absorption spectra of bundles of SWNTs via a tight-binding model, which stressed the spectral differences caused by different chiral angles [51]. Margulis and Gaiduk also proposed a single-electron theory for the absorption spectra of a bundle of diameter-distributed SWNTs that gave good agreement with measurements with regard to both the position and spectral shape of the fundamental

absorption edge [141]. Hagen and Hertel discussed how tight-binding band-structure calculations with a chirality- and diameter-dependent nearest-neighbor-hopping integral may be used to relate well-resolved features in the absorption spectra of individual SWNTs to electronic excitations in specific tube types [142]. Our earlier LDM study [49] on the 4-Å SWNTs shows that the absorption spectra of the (4, 2), (3, 3), and (5, 0) SWNTs are distinct, although their diameters are virtually the same (4.2, 4.1, and 3.9 Å, respectively). When the CNT diameter d_t is comparable to C–C bond length a, adjacent π orbitals overlap. The extent of the orbital overlaps depends on the orientation along which the tube is rolled up, and this leads to the spectral lineshapes that are sensitive to the chiral angles. With support from both the DFT and LDM calculations, it can be concluded that to the lowest order in a/d_t, the simple tight-binding model provides an accurate description of low-energy optical processes in SWNTs [43]. The diameters of the (5, 5), (6, 4), and (8, 0) SWNTs are modestly large compared to the C–C bond length. Greater SWNT diameters are expected to bring the DFT and LDM calculations into closer agreement with the tight-binding results. In addition to its success in describing the nanotubes' band structures, the tight-binding model provides a remarkably accurate overall account of the low-energy absorption lineshapes. Optical properties of a series of finite-size SWNTs, including those with the smallest diameter (4 Å), DWNTs, CNT junctions, and SWNTs with localized defects have been studied systematically. Their absorption spectra are calculated with the LDM method. The Pariser–Parr–Pople (PPP) and MNDO parametric method 3 (PM3) semiempirical Hamiltonians are employed. The finite optical gaps are predicted for the infinite long SWNTs. Strong anisotropy of the dynamic polarizabilities is found for 4-Å SWNTs [143]. Calculated results on 4-Å SWNTs are in good agreement with the recent experimental findings. Furthermore, the compositions of the dipole-induced excitations are examined by projecting the corresponding density matrices onto the Hartree–Fock molecular orbital representation. Via the DFT approach electronic and optical properties of a potassium iodide intercalated (10, 10) nanotube are also calculated.

To summarize, a multiapproached picture is presented for optical absorption spectra of single-walled carbon nanotubes (SWNTs), and theories on SWNT optical properties of incremental sophistication have been reviewed. On the basis of the simplified treatment of the tight-binding model, a visual, intuitive connection is given between optical absorption lineshapes and the underlying carbon nanotube structures. Within the tight-binding model, the absorption spectra of SWNTs can be linked directly to plots of energy contours and transition dipoles of a graphene sheet. Calculations based on two distinctively different methods, the LDM and DFT approaches, result in common low-energy absorption spectral features for SWNTs with diameters much larger than the C–C bond length. These spectral features survive σ–π orbital rehybridization and electronic correlations and are further supported by measured absorption spectra and EELS of SWNT bundles. Among many useful results presented here is the vertical transition dipole $\mathbf{d}$ between the valence-band wave function $|\phi_v(\mathbf{k})\rangle$ and the corresponding conduction-band wave function $|\phi_c(\mathbf{k})\rangle$ defined as $\mathbf{d} \equiv \langle\phi_c(\mathbf{k})|e\mathbf{r}|\phi_c(\mathbf{k})\rangle$ (cf. Fig. 2c).

Emerging fields of nanotechnology hold the promise of overcoming limitations of existing technologies on nanoscale manipulation. In particular, these new developments provide approaches for the creation of chemical–biological hybrid nanocomposites that can have a variety of applications such as being introduced into cells, and they can subsequently be used to initiate intracellular processes or biochemical reactions. Such nanocomposites may advance medical biotechnology as much as introduce new possibilities in chemistry and material sciences. SWNTs and their derivatives are among the simplest nanocomposites that are currently undergoing intense experimental and theoretical investigations. Various manufacturing methods produce SWNTs in form of bundles or ropes intertwined with the van der Waals interactions, and identification of spectroscopic signatures and correlation with nanotube structures helps purify and segregate SWNTs. Optical properties of SWNTS therefore become indispensable to structure-based nanotube characterization and separation.

Recently discovered near-infrared band-gap photoluminescence of dispersed, micelle-isolated semiconducting SWNTs allow optical-spectra-based characterization of SWNT structures. Optical measurements of individual SWNTs in aqueous surfactant suspensions provide

information that is sensitive to both SWNT chiralities and diameters [35, 131–133]. Time-resolved carrier dynamics in SWNTs have been investigated by means of two-color pump-probe techniques [144]. Using various pump-probe wavelengths and intensities, femtosecond dynamics of photoexcitations in films containing semiconducting and metallic SWNTs have also been studied to probe confined excitons and charge carriers [145]. More stringent tests on theoretical models of SWNT optical properties will soon be available from Raman, luminescence, and ultrafast spectroscopic measurements that are being carried out for isolated SWNTs as well as for SWNT bundles.

ACKNOWLEDGMENTS

This work is supported by the Hong Kong Research Grant Council (RGC) and the Committee for Research and Conference Grants (CRCG) of the University of Hong Kong. The authors would like to thank W. Z. Liang, C. Y. Yam, and S. Yokojima for their help in preparing the manuscript.

REFERENCES

1. S. Iijima, *Nature* 354, 56 (1991).
2. T. W. Ebbesen and P. M. Ajayan, *Nature* 358, 220 (1992); T. W. Ebbesen, H. Hiura, J. Fujita, Y. Ochiai, S. Matsui, and K. Tanigaki, *Chem. Phys. Lett.* 209, 83 (1993).
3. S. Iijima and T. Ichihashi, *Nature* 363, 603 (1993).
4. D. S. Bethune, C. H. Kiang, M. S. Devries, G. Gorman, R. Savoy, J. Vazquez, and R. Beyers, *Nature* 363, 605 (1993).
5. S. Iijima, *Mater. Sci. Eng. B* 19, 172 (1993).
6. K. Sattler, *Carbon*, 33, 915 (1995).
7. M. Bockrath, D. H. Cobden, P. L. McEuen, N. G. Chopra, A. Zettl, A. Thess, and R. E. Smalley, *Science* 275, 1922 (1997).
8. K. Tsukagoshi, B. W. Alphenaar, and H. Ago, *Nature* 401, 572 (1999).
9. R. D. Antonov and A. T. Johnsons, *Phys. Rev. Lett.* 83, 3274 (1999).
10. Z. Yao, H. W. Ch. Postma, L. Balents, and C. Dekker, *Nature* 402, 273 (1999).
11. R. E. Tuzun, D. W. Noid, and B. G. Sumpter, *Nanotechnology* 6, 64 (1995).
12. D. Srivastava, *Nanotechnology* 8, 186 (1997).
13. J. Cumings and A. Zettl, *Science* 289, 602 (2000).
14. S. Berber, Y. K. Kwon, and D. Tománek, *Phys. Rev. Lett.* 91, 165503 (2003).
15. Q. S. Zheng and Q. Jiang, *Phys. Rev. Lett.* 88, 045503 (2002); Q. S. Zheng, J. Z. Liu, and Q. Jiang, *Phys. Rev. B* 65, 245209 (2002).
16. Y. Zhao, C. C. Ma, G. H. Chen, and Q. Jiang, *Phys. Rev. Lett.* 91, 175504 (2003).
17. S. B. Legoas, V. R. Coluci, S. F. Braga, P. Z. Coura, S. O. Dantas, and D. S. Galvão, *Phys. Rev. Lett.* 90, 055504 (2003).
18. J. L. Rivera, C. McCabe, and P. T. Cummings, *Nano. Lett.* 3, 1001 (2003).
19. W. L. Guo, Y. f. Guo, H. J. Gao, Q. S. Zheng, and W. Y. Zhong, *Phys. Rev. Lett.* 91, 125501 (2003).
20. N. Hamada, S. Sawada, and A. Oshiyama, *Phys. Rev. Lett.* 68, 1579 (1992).
21. M. S. Dresselhaus, G. Dresselhaus, and P. C. Eklund, "Science of Fullerenes and Carbon Nanotubes." Academic Press, San Diego, CA, 1996.
22. R. Saito, M. Fujita, G. Dresselhaus, and M. S. Dresselhaus, *Appl. Phys. Lett.* 60, 2204 (1992); R. Saito, M. Fujita, G. Dresselhaus, and M. S. Dresselhaus, *Phys. Rev. B* 46, 1804 (1992).
23. R. Saito, G. Dresselhaus, and M. S. Dresselhaus, "Physical Properties of Carbon Nanotubes." Imperial College Press, London, 1998.
24. C. T. White, D. H. Robertson, and J. W. Mintmire, *Phys. Rev. B* 47, 5485 (1993).
25. K. Keren, R. S. Berman, E. Buchstab, U. Sivan, and E. Braun, *Science* 302, 1380 (2003).
26. M. Freitag, Y. Martin, J. A. Misewich, R. Martel, and P. Avouris, *Nano. Lett.* 3, 1067 (2003).
27. J. A. Misewich, R. Martel, Ph. Avouris, J. C. Tsang, S. Heinze, and J. Tersoff, *Science* 300, 783 (2003).
28. M. Zheng, A. Jagota, M. S. Strano, A. P. Santos, P. Barone, S. G. Chou, B. A. Diner, M. S. Dresselhaus, R. S. Mclean, G. B. Onoa, G. G. Samsonidze, E. D. Semke, M. Usrey, and D. J. Walls, *Science* 302, 1545 (2003).
29. T. Pichler, M. Knupfer, M. S. Golden, J. Fink, A. Rinzler, and R. E. Smalley, *Phys. Rev. Lett.* 80, 4729 (1998).
30. O. Jost, A. A. Gorbunov, W. Pompe, T. Pichler, R. Friedlein, M. Knupfer, M. Reibold, H.-D. Bauer, L. Dunsch, M. S. Golden, and J. Fink, *Appl. Phys. Lett.* 75, 2217 (1999).
31. H. Kataura, Y. Kumazawa, Y. Maniwa, I. Umezu, S. Suzuki, Y. Ohtsuka, Y. Achiba, *Synth. Met.* 103, 2555 (1999).
32. N. Wang, Z. K. Tang, G. D. Li, and J. S. Chen. *Nature* 408, 50 (2000).

33. Z. M. Li, Z. K. Tang, H. J. Liu, N. Wang, C. T. Chan, R. Saito, S. Okada, G. D. Li, J. S. Chen, N. Nagasawa, and S. Tsuda, *Phys. Rev. Lett.* 87, 127401 (2001).
34. M. J. O'Connell, S. M. Bachilo, C. B. Huffman, V. C. Moore, M. S. Strano, E. H. Haroz, K. L. Rialon, P. J. Boul, W. H. Noon, C. Kittrell, J. P. Ma, R. H. Hauge, R. Bruce Weisman, and R. E. Smalley, *Science* 297, 593 (2002).
35. S. M. Bachilo, M. S. Strano, C. Kittrell, R. H. Hauge, R. E. Smalley, and R. Bruce Weisman, *Science* 298, 2361 (2002).
36. M. S. Strano, S. K. Doorn, E. H. Haroz, C. Kittrell, R. H. Hauge, and R. E. Smalley, *Nano. Lett.* 3, 1091 (2003).
37. M. Zheng, A. Jagota, E. D. Semke, B. A. Diner, R. S. Mclean, S. R. Lustig, R. E. Richardson, N. G. Tassi, *Nat. Mater.* 2, 338 (2003).
38. K. Kamaras, M. E. Itkis, H. Hu, B. Zhao, and R. C. Haddon, *Science* 301, 1501 (2003).
39. M. S. Strano, C. A. Dyke, M. L. Usrey, P. W. Barone, M. J. Allen, H. W. Shan, C. Kittrell, R. H. Hauge, J. M. Tour, and R. E. Smalley, *Science* 301, 1519 (2003).
40. R. S. Lee, H. J. Kim, J. E. Fischer, A. Thess, and R. E. Smalley, *Nature* 388, 255 (1997).
41. J. Sloan, M. C. Novotny, S. R. Bailey, G. Brown, C. Xu, V. C. Williams, S. Friedrichs, E. Flahaut, R. L. Callender, A. P. E. York, K. S. Coleman, M. L. H. Green, R. E. Dunin-Borkowski, and J. L. Hutchison, *Chem. Phys. Lett.* 329, 61 (2000).
42. R. R. Meyer, J. Sloan, R. E. Dunin-Borkowski, A. I. Kirkland, M. C. Novotny, S. R. Bailey, J. L. Hutchison, and M. L. H. Green, *Science* 289, 1324 (2000).
43. Y. Zhao, X. J. Wang, C. C. Ma, and G. H. Chen, *Chem. Phys. Lett.* 387, 149 (2004).
44. R. Saito, G. Dresselhaus, and M. S. Dresselhaus, *Phys. Rev. B* 61, 2981 (2000).
45. S. Reich and C. Thomsen, *Phys. Rev. B* 62, 4273 (2000).
46. C. T. White and J. W. Mintmire, *Nature* 394, 29 (1998).
47. J. W. G. Wildöer, L. C. Venema, A. G. Rinzler, R. E. Smalley, and C. Dekker, *Nature* 391, 59 (1998).
48. S. Yokojima and G. H. Chen, *Chem. Phys. Lett.* 300, 540 (1999).
49. W. Z. Liang, S. Yokojima, D. H. Zhou, and G. H. Chen, *J. Phys. Chem. A* 104, 2445 (2000).
50. W. A. de Heer, W. S. Bacsa, A. Châtelain, T. Gerfin, R. Humphrey-Baker, L. Forro, and D. Ugarte, *Science* 268, 845 (1995).
51. M. F. Lin and W. K. Shung, *J. Phys. Soc. Jpn.* 66, 3294 (1997).
52. M. F. Lin, *Phys. Rev. B* 62, 13153 (2000).
53. A. Grüneis, R. Saito, Ge. G. Samsonidze, T. Kimura, M. A. Pimenta, A. Jorio, A. G. Souza Filho, G. Dresselhaus, and M. S. Dresselhaus, *Phys. Rev. B* 67, 165402 (2003).
54. F. L. Shyu, C. P. Chang, R. B. Chen, C. W. Chiu, and M. F. Lin, *Phys. Rev. B* 67, 045405 (2003).
55. H. Ajiki and T. Ando, *Physica B* 201, 349 (1994).
56. A. G. Souza Filho, A. Jorio, Ge. G. Samsonidze, G. Dresselhaus, M. S. Dresselhaus, A. K. Swan, M. S. Ünlüe, B. B. Goldberg, R. Saito, J. H. Hafner, C. M. Lieber, and M. A. Pimenta, *Chem. Phys. Lett.* 354, 62 (2002).
57. Ge. G. Samsonidze, R. Saito, A. Jorio, A. G. Souza Filho, A. Grüneis, M. A. Pimenta, G. Dresselhaus, and M. S. Dresselhaus, *Phys. Rev. Lett.* 90, 027403 (2003).
58. X. Liu, T. Pichler, M. Knupfer, M. S. Golden, J. Fink, H. Kataura, and Y. Achiba, *Phys. Rev. B* 66, 045411 (2002).
59. P. Ring and P. Schuck, "The Nuclear Many-Body Problem." Springer, New York, 1980.
60. S. Yokojima and G. H. Chen, *Chem. Phys. Lett.* 292, 379 (1998).
61. S. Yokojima and G. H. Chen, *Phys. Rev. B* 59, 7259 (1999).
62. M. F. Li, "Modern Semiconductor Quantum Physics." World Scientific, Singapore, 1995.
63. S. Yokojima, D. H. Zhou, and G. H. Chen, *Chem. Phys. Lett.* 302, 495 (1999).
64. W. Z. Liang, S. Yokojima, and G. H. Chen, *J. Chem. Phys.* 110, 1844 (1999).
65. W. Z. Liang, X. J. Wang, S. Yokojima, and G. H. Chen, *J. Am. Chem. Soc.* 122, 11129 (2000).
66. W. Z. Liang, S. Yokojima, M. F. Ng, G. H. Chen, and G. Z. He, *J. Am. Chem. Soc.* 123, 9830 (2001).
67. S. Yokojima, X. J. Wang, D. H. Zhou, and G. H. Chen, *J. Chem. Phys.* 111, 10444 (1999).
68. R. F. Willis, B. Feuerbacher, and B. Fitton, *Phys. Rev. B* 4, 2441 (1971).
69. J. Del Bene and H. H. Jaffe, *J. Chem. Phys.* 48, 1807 (1968); *J. Chem. Phys.* 48, 4050 (1968).
70. J. A. Pople, D. L. Beveridge, and P. A. Dobosh, *J. Chem. Phys.* 47, 2026 (1967).
71. M. J. S. Dewar and W. Thiel, *J. Am. Chem. Soc.* 99, 4899 (1977).
72. M. J. S. Dewar, E. G. Zoebisch, E. F. Healy, and J. J. P. Stewart, *J. Am. Chem. Soc.* 107, 3902 (1985).
73. J. J. P. Stewart, *J. Comput. Chem.* 10, 209 (1989).
74. X.-M. Duan, H. Konami, S. Okaka, H. Oikawa, H. Matsuda, and H. Nakanishi, *J. Phys. Chem.* 100, 17780 (1996).
75. U. S. Choi, T. W. Kim, S. W. Jung, and C. J. Kim, B. Kor, *Chem. Soc.* 19, 299 (1998).
76. N. Matsuzawa and D. A. Dixon, *J. Phys. Chem.* 96, 6232 (1992).
77. S. Sawada and N. Hamada, *Solid State Commun.* 83, 917 (1992).
78. J. Tersoff, *Phys. Rev. Lett.* 61, 2879 (1988).
79. L.-C. Qin, X. Zhao, K. Hirahara, Y. Miyamoto, Y. Ando, and S. Iijima, *Nature* 408, 50 (2000).
80. H. Y. Peng, N. Wang, Y. F. Zheng, Y. Lifshitz, J. Kulik, R. Q. Zhang, C. S. Lee, and S. T. Lee, *Appl. Phys. Lett.* 77, 2831 (2000).
81. Z. K. Tang, private communication.

82. S. Leach, M. Vervloet, A. Despres, E. Breheret, J. P. Hare, T. J. Dennis, H. W. Kroto, R. Taylor, and D. R. M. Walton, *Chem. Phys.* 160, 451 (1992).
83. R. Saito, T. Takeya, T. Kimura, G. Dresselhaus, and M. S. Dresselhaus, *Phys. Rev. B* 59, 2388 (1999).
84. Z. Zhang and C. M. Lieber, *Appl. Phys. Lett.* 62, 2792 (1993).
85. T. W. Odom, J.-L. Huang, P. Kim, and C. M. Lieber, *Nature* 391, 62 (1998).
86. E. W. Wong, P. E. Sheehan, and C. M. Lieber, *Science* 277, 1971 (1997).
87. M. A. Hamon, J. Chen, H. Hu, Y. Chen, M. E. Itkis, A. M. Rao, P. C. Eklund, and R. C. Haddon, *Adv. Mater.* 11, 834 (1999).
88. J. Ma and R.-K. Yuan, *Phys. Rev. B* 57, 9343 (1998).
89. J. Jiang, J. Dong, and D. Y. Xing, *Phys. Rev. B* 59, 9838 (1999); J. Jiang, J. M. Dong, X. G. Wan, and D. Y. Xing, *J. Phys. B* 31, 3079 (1998).
90. J. Chen, M. A. Hamon, H. Hu, Y. Chen, A. M. Rao, P. C. Eklund, and R. C. Haddon, *Science* 282, 95 (1998).
91. M.-F. Lin and K. W.-K. Shung, *Phys. Rev. B* 50, 17744 (1994); M.-F. Lin, K. W.-K. Shung, D. S. Chuu, C. S. Huang, and Y. K. Lin, *Phys. Rev. B* 53, 15493 (1996).
92. P. M. Ajayan, S. Iijima, and T. Ichihashi, *Phys. Rev. B* 47, 6859 (1993).
93. A. Rochefort, D. R. Salahub, and P. Avouris, *J. Phys. Chem. B* 103, 641 (1999).
94. P. Kim, T. W. Odom, J. L. Huang, and C. M. Lieber, *Phys. Rev. Lett.* 82, 1225 (1999).
95. J. C. Charlier, *Phys. Rev. B* 57, R15037 (1998).
96. A. Rochefort, D. S. Salahub, and P. Avouris, *Chem. Phys. Lett.* 297, 45 (1998).
97. A. M. Rao, E. Richter, S. Bandow, B. Chase, P. C. Elund, K. A. Williams, S. Fang, K. R. Subbaswamy, M. Menon, A. Thess, R. E. Smalley, G. Dresselhaus, and M. S. Dresselhaus, *Science* 275, 187 (1997).
98. X. Blase, L. X. Benedict, E. L. Shirley, and S. G. Louie, *Phys. Rev. Lett.* 72, 1878 (1994).
99. L. G. Bulusheva, A. V. Okotrub, D. A. Romanov, and D. Tomanek, *J. Phys. Chem. A* 102, 975 (1998).
100. R. C. Haddon, *Acc. Chem. Res.* 21, 243 (1988).
101. R. C. Haddon, *J. Phys. Chem. A* 105, 4164 (2001).
102. W. Ludwig and C. Falter, "Symmetries in Physics: Group Theory Applied to Physical Problems." Springer, New York, 1996.
103. G. H. Chen and S. Mukamel, *J. Am. Chem. Soc.* 117, 4945 (1995).
104. B. Zhou, Y. Lin, H. Li, W. Huang, J. W. Connell, L. F. Allard, and Y. P. Sun, *J. Phys. Chem. B* 107, 13588 (2003).
105. S. Banerjee and S. S. Wong, *J. Am. Chem. Soc.* 124, 8940 (2002).
106. F. Pompeo and D. E. Resasco, *Nano. Lett.* 2, 369 (2002).
107. Z. Jin, X. Sun, G. Xu, S. H. Goh, and W. Ji, *Chem. Phys. Lett.* 318, 505 (2000).
108. J. L. Bahr and J. M. Tour, *J. Mat. Chem.* 12, 1952 (2002).
109. S. Okada and A. Oshiyama, *Phys. Rev. Lett.* 91, 216801 (2003).
110. Y. Miyamoto, S. Saito, and D. Tománek, *Phys. Rev. B* 65, 041402 (2001).
111. H. Stahl, J. Appenzeller, R. Martel, Ph. Avouris, and B. Lengeler, *Phys. Rev. Lett.* 85, 5186 (2000).
112. P. Delaney, H. J. Choi, J. Ihm, S. G. Louie, and M. L. Cohen, *Nature* 391, 466 (1998).
113. Y.-K. Kwon, S. Saito, and D. Tománek, *Phys. Rev. B* 58, R13314 (1998).
114. B. W. Smith, M. Monthioux, and D. E. Luzzi, *Nature* 396, 323 (1998).
115. L. Chico, V. H. Crespi, L. X. Benedict, S. G. Louie, and M. L. Cohen, *Phys. Rev. Lett.* 76, 971 (1996).
116. A. Rubio, *Appl. Phys. A* 68, 275 (1999).
117. A. Rubio, D. Sánchez-Portal, E. Artacho, P. Ordejón, and J. M. Soler, *Phys. Rev. Lett.* 82, 3520 (1999).
118. H. J. Liu and C. T. Chan, *Phys. Rev. B* 66, 115416 (2002).
119. A. G. Marinopoulos, L. Reining, A. Rubio, and N. Vast, *Phys. Rev. Lett.* 91, 046402 (2003).
120. D.-S. Wu, W.-D. Cheng, H. Zhang, X.-D. Li, Y.-Z. Lan, D.-G. Chen, Y.-J. Gong, and Y.-C. Zhang, *Phys. Rev. B* 68, 125402 (2003).
121. P. Hohenberg and W. Kohn, *Phys. Rev.* 136, B864 (1964).
122. W. Kohn and L. J. Sham, *Phys. Rev.* 140, A1133 (1965).
123. P. Blaha, K. Schwarz, and J. Luitz, "WIEN97, A Full Potential Linearized Augmented Plane Wave Package for Calculating Crystal Properties." Karlheinz Schwarz, Techn. Universitat, Wien, 1999.
124. S. Okada, S. Saito, and A. Oshiyama, *Phys. Rev. Lett.* 86, 3835 (2001).
125. T. Pichler, X. Liu, M. Knupfer, and J. Fink, *New J. Phys.* 5, 156 (2003).
126. M. Ouyang, J. L. Huang, C. L. Cheung, and C. M. Lieber, *Science* 292, 702 (2001).
127. J. W. Ding, X. H. Yan, and J. X. Cao, *Phys. Rev. B* 66, 073401 (2002).
128. M. E. Itkis, S. Niyogi, M. E. Meng, M. A. Hamon, H. Hu, and R. C. Haddon, *Nano. Lett.* 2, 155 (2002).
129. M. Ichida, S. Mizuno, Y. Saito, H. Kataura, Y. Achiba, and A. Nakamura, *Phys. Rev. B* 65, 241407 (2002).
130. J. P. Perdew and Y. Wang, *Phys. Rev. B* 45, 13244 (1992).
131. S. M. Bachilo, L. Balzano, J. E. Herrera, F. Pompeo, D. E. Resasco, and R. B. Weisman, *J. Am. Chem. Soc.* 125, 11186 (2003).
132. S. Maruyama, Y. Miyauchi, Y. Murakami, and S. Chiashi, *New J. Phys.* 5, 149 (2003).
133. S. Lebedkin, K. Arnold, F. Hennrich, R. Krupke, B. Renker, and M. M. Kappes, *New J. Phys.* 5, 140 (2003).
134. A. Hartschuh, H. N. Pedrosa, L. Novotny, and T. D. Krauss, *Science* 301, 1354 (2003).
135. R. B. Weisman and S. M. Bachilo, *Nano. Lett.* 3, 1235 (2003).
136. C. L. Kane and E. J. Mele, *Phys. Rev. Lett.* 90, 207401 (2003).

137. C. D. Spataru, S. Ismail-Beigi, L. X. Benedict, and S. G. Louie, *Phys. Rev. Lett.* 92, 077402 (2004).
138. S. Lebedkin, F. Hennrich, T. Skipa, and M. M. Kappes, *J. Phys. Chem. B* 107, 1949 (2003).
139. X. Wan, J. Dong, and D. Y. Xing, *Phys. Rev. B* 58, 6756 (1998).
140. T. Ando, *J. Phys. Soc. Jpn.* 66, 1066 (1997).
141. V. A. Margulis and E. A. Gaiduk, *Phys. Lett. A* 281, 52 (2001).
142. A. Hagen and T. Hertel, *Nano. Lett.* 3, 383 (2003).
143. W. Z. Liang, G. H. Chen, Z. M. Li, and Z. K. Tang, *Appl. Phys. Lett.* 80, 3415 (2002).
144. J.-S. Lauret, C. Voisin, G. Cassabois, C. Delalande, P. Roussignol, O. Jost, and L. Capes, *Phys. Rev. Lett.* 90, 057404 (2003).
145. O. J. Korovyanko, C. X. Sheng, Z. V. Vardeny, A. B. Dalton, and R. H. Baughman, *Phys. Rev. Lett.* 92, 017403 (2004).